ABSTRACT

Title of Document:	AN EXPERIMENTAL ANALYSIS OF FIREFIGHTER PROTECTIVE CLOTHING: THE INFLUENCES OF MOISTURE AND A THERMALLY ACTIVATED EXPANDING AIR-GAP.
	James Patrick White, Master of Science, 2012
Directed By:	Professor, Marino di Marzo, Department of Fire Protection Engineering

Thermally protective clothing garments are necessary pieces of equipment that ensure the life safety of firefighters. In this analysis, material samples of such garments are tested experimentally with and without the presence of both moisture and a thermally activated, expanding air-gap. Moisture is delivered to samples via a porous baseplate with an integral fluid supply system, simulating perspiration. Operation of the expanding air-gap is controlled by a custom-designed assembly of shape-memory rings, which undergo a shape transformation over a predetermined temperature range. Samples with varying characteristic layers and arrangements are subjected to a controlled thermal exposure. The performances of tested samples are evaluated based on normalized temperature parameters. Assembly characteristics offering the greatest protective performance are then established. Results suggest that limiting moisture absorption in the thermal liner of a garment and implementing air-gaps of increasing thickness improve the protective performance of firefighter protective clothing.

AN EXPERIMENTAL ANALYSIS OF FIREFIGHTER PROTECTIVE
CLOTHING: THE INFLUENCES OF MOISTURE AND A THERMALLY
ACTIVATED EXPANDING AIR-GAP

By

James Patrick White

Thesis submitted to the Faculty of the Graduate School of the
University of Maryland, College Park, in partial fulfillment
of the requirements for the degree of
Master of Science
2012

Advisory Committee:
Professor Marino di Marzo, Chair
Professor Amr Baz
Associate Professor Arnaud Trouve

Acknowledgements

Table of Contents

List of Tables

List of Figures

Nomenclature

NTR	Normalized Temperature-Rise Parameter
NTG	Normalized Temperature-Gradient Parameter
T	Temperature
$\bar{T}$	Average Temperature
E	Total Energy
$\dot{q}$	Rate of Heat Transfer
$\dot{q}''$	Heat Flux
$\dot{q}'''$	Volumetric Heat Flux
$\dot{m}''$	Mass Flux
λ	Thermal Conductivity
ρ	Mass Density
c	Heat Capacity
D_{th}	Thermal Diffusivity
I_{th}	Thermal Inertia
β	Thermal Expansion Coefficient
υ	Kinematic Viscosity
α	Absorptivity
γ	Reflectivity
τ	Transmissivity
ε	Emissivity
G	Irradiance
J	Radiosity
F	View Factor
h	Convective Heat Transfer Coefficient
Ra	Rayleigh Number
Nu	Nusselt Number
Fo	Fourier Number
$\vec{n}$	Unit Vector Normal to a Surface

S	Standard Deviation
φ, a, b	Arbitrary Quantity
f	Arbitrary Function
t	Time
x	Position
δ	Thickness
z	Elevation
A	Cross-Sectional Area / Surface Area
V	Volume
N	Total Count
σ	Stefan-Boltzmann Constant
g	Gravitational Acceleration Constant
Δ	Change in Value
∇	Del Operator
d, ∂	Ordinary / Partial Differential
n	Time of Interest (superscript)
0	Initial Condition (superscript)
i	Position of Interest (subscript)
∞	Ambient Condition (subscript)
j, k	Item Within a Set (subscript)
$1, 2, 3, 4$	Specific Item of Interest (subscript)
bp	Baseplate (subscript)
os	Outer Surface (subscript)
fl	Fluid (subscript)
rv	Fluid Reservoir (subscript)
cy	Cylinder (subscript)
$cond$	Conduction (subscript)
$conv$	Convection (subscript)
rad	Radiation (subscript)
eff	Effective (subscript)

Chapter 1 : Introduction

1.1: Problem Statement

During their regular work operations, firefighters are exposed to conditions involving intense thermal exposures that have the potential to cause serious injury or death unless proper protective clothing is utilized. The abilities of a firefighter to mitigate a fire hazard successfully are limited because the length of time such conditions can safely be endured is dependent on the performance of the protective clothing. As a result, it is important that firefighter protective clothing provide sufficient protection to safeguard against the intense thermal insults that are regularly encountered.

Enhancements to firefighter protective clothing are twofold in that they improve firefighter life safety by reducing burn injuries and loss of life due to thermal exposure, and increase the effectiveness of firefighter operations by allowing thermal insults to be endured for prolonged periods. The fundamental goals of this research include improving firefighter life safety and increasing the effectiveness of firefighter operations. Such improvements are achieved by enhancing the overall effectiveness of firefighter protective clothing.

There exist a number of factors contributing to the effectiveness of a firefighter protective clothing garment. These factors range from operational features such as the weight, comfort, mobility, and cost of the garment, to fundamental protective features such as reduced ignition propensity, resistance to heat and moisture transport, and dissemination of stored thermal energy. It may be initially

perceptible that improvements to the protective features of the garment are more critical than preservation of the operational features; however, it is important to note that both types of features are instrumental to providing sufficient thermal protection to firefighters while facilitating their ability to mitigate fire hazards efficiently.

It is possible to improve the thermal protection provided by a garment simply by increasing the thickness of its protective layers; however, such an improvement increases the cost and weight of the garment and reduces its mobility, rendering successful firefighter operations more difficult. Improving the efficiency of firefighter operations is a quintessential goal of firefighter safety research and such a manner of improving performance is thus unacceptable. As improvements to the protective features of a garment generally result in reductions to operational features, it is necessary to strike a balance between both types of features to ensure that neither is prohibitively relegated.

For this analysis, the fundamental performance improvements considered to increase the overall effectiveness of firefighter protective clothing include the minimization of the rate of temperature-rise at the inner surface of the garment and the maximization of the temperature-drop occurring across the garment for steady-state conditions. Such improvements occur ideally without reducing the operational features of the garment such as by increasing cost or weight, or by decreasing comfort or mobility. While there are a number of factors influencing such improvements, some of the more controlling elements include the presence and amount of moisture in the garment, and the thickness of the air-gaps separating adjacent garment layers. It is with respect to these two factors that this research makes its focus.

1.2: Firefighter Protective Clothing Design

Due to the intense thermal exposures experienced by firefighters, a multitude of protective equipment is necessary to facilitate the successful mitigation of fire hazards, while preventing resultant burn injuries. While the arsenal of protective equipment used by modern firefighters comprises a number of important devices, the focus of this analysis is limited to the coat and pants worn during normal response activities. These are collectively referred to as firefighter protective clothing, the primary purpose of which is the impedance of heat transfer. The design of such protective clothing has advanced greatly throughout history.

Early firefighter operations were mostly ineffective due to the lack of thermal protection offered by the first implementations of protective clothing. Such operations were usually limited to the exterior of a structure, as interior operations were prohibitively dangerous [1]. As a result, firefighter operations were frequently unsuccessful and most buildings burned to the ground [1]. Progressive improvements to the design of firefighter protective clothing were thus the natural result of the desire to increase the effectiveness of firefighter operations.

Initial firefighter protective clothing consisted of a single-layer wool coat, underneath which, firefighters would wear an undershirt of either cotton or wool [1]. Wool is a thick, porous material with a large amount of interstitial air between its fibers and acts as a suitable thermal insulator due to its reduced capacity to conduct heat. Despite this, wool offers no ignition protection and its thermal conductivity is greatly increased when subjected to moisture. Eventually, firefighters began wearing rubber slickers over the wool coat, as these provided an impermeable outer layer that

kept the protective clothing dry and offered additional ignition resistance [1]. Further implementation of rubber yielded long rubber trench coats and long rubber boots that effectively covered the majority of a firefighter's body [1]. Continued advancement during the 1980s brought the implementation of modern protective clothing materials such as Nomex® and Kevlar® [1].

The first standards defining firefighter protective clothing design were developed in the late 1940s. At this point, several organizations including the *National Fire Protection Association* (*NFPA*) began implementing performance tests to gauge the performance of thermal protective fabrics [1]. Initial standards mandated firefighter protective clothing to include three layers: an outer layer that offered resistance to ignition and thermal decomposition at high exposure temperatures and intense heat fluxes, a middle layer that prevented the transmission of moisture, and an inner layer that inhibited heat transfer [1].

The *NFPA* continues to monitor the design of modern firefighter protective clothing through the periodically updated *NFPA 1971: Standard on Protective Ensembles for Structural Firefighting and Proximity Firefighting* [2]. This document describes in detail the required design and performance criteria for firefighter protective clothing garments including material specifications, standardized testing procedures, and minimum scoring. While there are a number of testing standards detailed within *NFPA 1971*, some of the more important requirements with respect to garment protective performance include flame and heat resistance testing, thermal protective performance testing, and total heat loss testing. The procedural methods, performance criteria, and minimum scoring requirements of these tests are as follows.

Flame resistance tests are conducted to ensure that the materials constituting firefighter protective clothing garments exhibit sufficient ignition resistance. Such testing consists of the exposure of the cut edge of a material sample to a Bunsen burner flame for a period of twelve seconds [2]. After removal of the sample from the flame, the time duration over which the sample continues to burn and the length of the material exhibiting flame-induced damage are measured respectively as the after-flame time and char-length [2]. As required by *NFPA 1971*, materials used within firefighter protective clothing garments must measure an after-flame time of no greater than two seconds, a char-length of no greater than four inches, and must experience no melting or dripping [2].

In addition to flame resistance tests, heat resistance tests are used to gauge the thermal stability and thermal decomposition characteristics of tested materials during exposure to intense heating. Heat resistance testing requires the exposure of a material sample to an oven temperature of $260°C$ for a period of five minutes [2]. In order to qualify for inclusion within a firefighter protective clothing garment, *NFPA 1971* stipulates that tested materials must experience no ignition, melting, dripping, or separation, and cannot exhibit thermal shrinkage in excess of 10% by original length in any dimension [2].

Thermal protective performance (TPP) tests serve to measure the heat transfer resistance of a garment assembly. During testing, horizontally oriented samples are exposed from below to a combined convective and radiant thermal exposure consisting of two Bunsen burners and a radiant panel [2]. A calorimeter is used to quantify the test results and to predict a time-to-burn criterion, which signifies

the exposure time duration required to induce a second-degree burn injury. A TPP rating, given in units of calories per square centimeter, is then reported as the product of the time-to-burn criterion and the exposure heat flux [2]. *NFPA 1971* requires a minimum TPP rating of 35 for all firefighter protective clothing garments [2].

Total heat loss (THL) testing is conducted to measure the breathability of a garment assembly with respect to its ability to allow the escape of body heat. During testing, the transfer of heat through a sample is measured for dry and wet conditions utilizing a skin-simulant sweating guarded hotplate test apparatus [2]. A THL rating, given in units of watts per square meter, is then calculated based on the combined rate of heat loss through the sample due to conductive heat transfer and moisture evaporation [2]. As required by *NFPA 1971*, a minimum THL rating of 205 is required for all firefighter protective clothing garments [2].

In addition to the performance criteria previously summarized, *NFPA 1971* lists a number of additional testing requirements and design criteria that all firefighter protective clothing garments and constituent materials must respect. The fundamental purpose of these criteria is the establishment of a minimum standard design quality that defines the threshold protective performance characteristics required of all firefighter protective clothing.

Modern firefighter protective clothing consists of a multilayer garment including an outer shell, moisture barrier, and thermal liner. These layers closely mimic those mandated in the first standards developed by the *NFPA*. The outer shell is the outermost layer of the garment and serves as an outer layer of protection for the firefighter and for the garment itself. To this regard, the outer shell is durable and

resists tearing to prevent the exposure of inner layers to direct thermal insult. Additionally, the outer shell is ignition resistant and able to withstand large exposure temperatures and incident heat fluxes without undergoing thermal decomposition.

The moisture barrier is located within the garment and serves as an impermeable layer to prevent moisture transport. The moisture barrier is effective at inhibiting liquid-phase moisture movement in both directions through the garment but allows the transport of vapor-phase moisture. This prevents moisture from external sources from penetrating the inner layers of the garment while allowing vapor-phase moisture from perspiration to escape. Unlike the outer shell, the moisture barrier is relatively delicate and prone to damage through excessive wear and tear. For this reason, the impermeable film face of the moisture barrier is usually oriented inward, facing the soft insulation of the thermal liner as a means of preventing abrasion.

The thermal liner is also located within the garment and serves as the primary heat resistant layer, usually consisting of an insulation material quilted with a thinner, more durable facecloth material. The insulation is thick and contains a large amount of interstitial air between its fibers, thus providing low thermal conductivity. Like the moisture barrier, the insulation material is relatively delicate and prone to damage through wear and tear. To that effect, the facecloth serves as a guard to protect and maintain the integrity of the insulation material. The facecloth is also the innermost layer of the garment, resting either against the underclothing worn by the firefighter or directly against the skin. As such, the facecloth material acts to wick perspiration from the firefighter for added comfort and provides a slick interface between the firefighter and protective garment to improve mobility.

For this analysis, two arrangements of the thermal liner are considered: a traditional arrangement and a split arrangement. A traditionally layered thermal liner consists of a double thermal liner located entirely on the inner side of the moisture barrier. Conversely, a split-layered thermal liner consists of a single thermal liner located on each side of the moisture barrier. An illustration of these two arrangements is provided in **Figure 1.1**. In the figure, layers for both arrangements include a blue facecloth, gray insulation layer, yellow insulation layer, black moisture barrier, and gold outer shell. The purpose of distinguishing these two arrangements is to assess the influence of moisture on thermal liner performance. Considering moisture originating as perspiration from a firefighter, the entire thermal liner is exposed to moisture with a traditionally layered thermal liner, whereas only half of the thermal liner is exposed to moisture with a split-layered thermal liner. The split arrangement thus prevents exposure of half of the thermal liner to perspiration moisture.

Figure 1.1: Layers constituting a split (left) and traditionally (right) layered garment of firefighter protective clothing

1.3: Shape-Memory Materials

This research investigates the applicability of a thermally activated, expanding air-gap within a garment of firefighter protective clothing. The functionality of this expanding air-gap is achieved using shape-memory materials, the defining features of which are the abilities to remember a specific shape or orientation, and subsequently reassume that shape or orientation upon activation of the shape-memory effect. Noteworthy is that a shape-memory material can be trained to remember a particular shape of interest and that the remembered shape is reassumed even after the material is subjected to large deformations [3].

Activation of the shape-memory effect within a shape-memory material occurs via a crystallographic transformation from a martensite phase to an austenite phase. During this transformation, the microstructural properties of the material transition from the low-symmetry crystallography of the martensite phase to the high-symmetry crystallography of the austenite phase [3]. In the austenite phase, the structure of the material exists in a single, well-ordered crystal lattice that defines the austenitic shape of the material [3]. This austenitic shape also defines the remembered shape to which the material returns upon activation of the shape-memory effect.

As the material transforms from the austenite phase to the martensite phase, the high-symmetry, single-variant structure of the material reverts to a low-symmetry structure with multiple crystallographically equivalent variants in a twinned configuration [4]. In the absence of an applied stress, this transformation yields no macroscopic shape change in the material because the martensitic transformation is self-accommodating [3]. If a stress is applied to the material while in the martensite

phase, the material experiences large deformations as the multiple structural variants reorient with respect to one another [4]. This transition from twinned to deformed martensite, as caused by the application of stress, is referred to as de-twinning [3].

Upon reverse transformation from the martensite phase to the austenite phase, the material returns to the high-symmetry, single-variant austenitic crystallography and thus recovers the applied deformation, reassuming the remembered shape. This austenitic transformation defines the shape-memory effect.

The shape-memory effect exhibited by shape-memory materials is unique because the transformation between martensitic and austenitic structures is crystallographically reversible and can occur in either direction over numerous iterations [3]. This reversibility is achieved because the transformation involves a cooperative, homogenous shift of all molecules within the structure of the material and occurs without the action of localized diffusive transport [5]. Though the shift of individual molecules is microscopic, the resultant shape change of the material is large because the molecular shift occurs uniformly throughout the material [5].

Transformation between martensitic and austenitic structures occurs once a critical relationship between the free energies of the two phases is reached and can be induced by variations in either temperature or applied stress [4]. Because the transformation is independent of diffusive transport, it is independent of time and depends only on thermal and stress induced triggers. Increases in temperature or reductions in applied stress induce a martensite to austenite transformation, whereas decreases in temperature or escalations in applied stress induce an austenite to martensite transformation [4].

It is important to note that transformations in either direction occur between a characteristic start and finish criterion. For intermediate conditions during which the transformation is occurring, the material exists with some fraction of its structure in both the martensitic and austenitic phases [4]. The characteristic transformation start and finish criteria for a particular shape-memory material vary with changing temperature and applied stress conditions, and are dependent on a number of factors including the chemical and physical properties of the material [4].

For a constant applied stress condition, transformation start and finish criteria correspond to specific temperatures, whereas for a constant temperature condition, transformation criteria correspond to specific applied stresses. It should be noted that the start and finish criteria for martensitic transformation differ from the start and finish criteria for austenitic transformation. Within a garment of firefighter protective clothing, a constant applied stress condition is approximated; therefore, the start and finish criteria for transformation correspond to specific temperatures.

In order for a shape-memory material to assume a specific shape upon activation, it must first be trained to remember the desired shape. Training of a shape-memory material is achieved by heating the material to an elevated temperature above $500°C$ while restraining the material in the desired shape [3]. The material is held at this temperature for approximately 20 minutes and subsequently cooled in air [3]. In restraining the material to the desired shape, the high-symmetry crystallography of the austenite phase is forced to align with the desired shape of the material. Upon later re-transformation to the austenite phase, the material returns to the desired shape because the austenitic crystallography is aligned to that shape.

The fundamental modes by which heat transfers through a garment of firefighter protective clothing include conduction, convection, and radiation. While conduction is typically dominant, convection and radiation govern within air-gaps between garment layers. Additionally, convection and radiation are responsible for the thermal boundary conditions at the outer surface of a garment. Brief descriptions detailing the mechanisms governing these modes of heat transfer are as follows.

Conductive heat transfer is characterized by the diffusive transport of kinetic energy through a medium via molecular interactions [6]. As adjacent molecules interact, energy is transferred from high energy-state molecules to low energy-state molecules, thus heat conduction occurs in a direction from high temperature regions to low temperature regions [6]. Conductive heat transfer is dominant in solid materials because the spatial distribution of molecules is dense and molecular interactions occur readily. Heat conduction within firefighter protective clothing thus occurs primarily within and between individual garment layers.

It is important to note that adjacent layers are never in perfect thermal contact because there are a limited number of direct contact points between them. As a result, conductive heat transfer through a multilayer garment is greatly affected by the thermal contact resistance between adjacent layers. Thermal contact resistance is influenced by a number of factors including contact pressure, surface roughness, and the properties of the interstitial medium bridging the layers [6]. Because firefighter protective clothing garments consist of multiple layers, thermal contact resistance is an important factor affecting the protective performance of a garment.

Convection, like conduction, is characterized by the transport of kinetic energy through a system via molecular interactions; however, unlike conduction, convection includes the transport of energy by both diffusion and advection [6]. Convective heat transfer through advection occurs via molecular interactions caused by the bulk flow of molecules through a medium [6]. Advection is significantly more efficient than diffusion in transporting thermal energy because molecules carried by convective flows interact with far more molecules than those that remain stationary.

Convective heat transfer is important within liquid and gas-phase media because molecules in such media are allowed to move freely and advection occurs readily. For solid materials or media in which there are no convective currents, convection and conduction are approximately equal because advection is negligible and diffusive molecular interactions dominate [6]. Heat convection within firefighter protective clothing is limited to the air-gaps between garment layers, though the occurrence of sufficient advection within these air-gaps is typically negligible.

Unlike conduction and convection, which are characterized by the transport of kinetic energy through a medium, radiant heat transfer is characterized by the exchange of electromagnetic energy between mutually visible surfaces at an excited thermal state [6]. An excited thermal state refers to any surface with a temperature greater than absolute zero and thus radiant heat transfer occurs between virtually every body of matter [6]. Whereas conduction and convection require the presence of a medium to transport thermal energy, radiation requires no medium and occurs even across large distances through empty space [6]. Radiation within firefighter protective clothing garments occurs primarily within the air-gaps between garment layers.

Because all three modes of heat transfer are prevalent in some fashion, the development of a comprehensive generalized heat and mass transfer model for firefighter protective clothing is exceedingly difficult. This difficulty arises from the discontinuous nature of a multilayer garment, consisting of a composite of layered woven textile threads and interstitial air. Additionally, for a wet garment, moisture and air coexist in the interstitial medium with a varying spatial distribution of relative volume fractions. Heat transfer through such a garment depends on a wealth of spatially and thermally varying factors ranging from the thermal, physical, and optical properties, and relative spatial distributions of the fibers, air, and moisture comprising the garment; to the shape, size, and thread pattern of the individual fabric fibers.

While there are many factors affecting the mechanisms governing firefighter protective clothing performance, some of the more significant factors include the presence and amount of air and moisture within a garment. Air and moisture are significant primarily because of the differences between their associated thermal properties and those of typical firefighter protective clothing materials.

The effective thermal properties of a garment layer depend on the associated thermal properties and relative volume fractions of the fibers and interstitial medium comprising that layer. For porous fabrics, such as those utilized in the thermal liner layers of firefighter protective clothing garments, the interstitial medium comprises the majority of the layer and the thermal properties of the medium dominate. Because air and moisture serve as the primary interstitial media within firefighter protective clothing layers, their respective thermal properties have a profound impact on the protective performance of a garment.

The thermal properties of air, liquid water, and water vapor at selected temperatures are provided respectively in **Table 1.1**, **Table 1.2**, and **Table 1.3**.

Table 1.1: Thermal properties of air at selected temperatures [6]

$T\ (K)$	$\lambda\ (W/mK)$	$\rho\ (kg/m^3)$	$c\ (J/kgK)$	$D_{th}\ (m^2/s)$	$I_{th}\ (kg/s^{5/2}K)$
300	0.0263	1.1614	1007	$2.25*10^{-5}$	5.55
400	0.0338	0.8711	1014	$3.83*10^{-5}$	5.46
500	0.0407	0.6964	1030	$5.67*10^{-5}$	5.40

Table 1.2: Thermal properties of liquid water at selected temperatures [6]

$T\ (K)$	$\lambda\ (W/mK)$	$\rho\ (kg/m^3)$	$c\ (J/kgK)$	$D_{th}\ (m^2/s)$	$I_{th}\ (kg/s^{5/2}K)$
300	0.613	997.0	4179	$1.47*10^{-7}$	$1.60*10^3$
350	0.668	973.7	4195	$1.64*10^{-7}$	$1.65*10^3$
370	0.679	960.6	4214	$1.68*10^{-7}$	$1.66*10^3$

Table 1.3: Thermal properties of water vapor at selected temperatures [6]

$T\ (K)$	$\lambda\ (W/mK)$	$\rho\ (kg/m^3)$	$c\ (J/kgK)$	$D_{th}\ (m^2/s)$	$I_{th}\ (kg/s^{5/2}K)$
380	0.0246	0.5863	2060	$2.04*10^{-5}$	5.45
400	0.0261	0.5542	2014	$2.34*10^{-5}$	5.40
500	0.0339	0.4405	1985	$3.88*10^{-5}$	5.44

In viewing the property values provided in these tables, note that thermal diffusivity and thermal inertia are functions of the other thermal properties and are given respectively by the following expressions.

$$D_{th} = \frac{\lambda}{\rho c}, \qquad I_{th} = \sqrt{\lambda \rho c} \qquad\qquad (1.1, 1.2)$$

As shown in the tables, the thermal properties of air differ significantly from those of liquid water. It is thus expected that the presence of air and moisture have profoundly different effects on the rate of heat transfer through a garment. In order to

demonstrate the significance of these thermal property variations, a simple numerical simulation is conducted to evaluate the time evolution of the spatial distribution of temperature within a layer prescribed with the thermal properties of either air or liquid water. This simulation utilizes the following governing heat diffusion equation, neglecting the effects of convection and radiation and considering one-dimensional transient heat conduction only. A detailed derivation of this expression is provided in *Appendix A*.

$$\frac{\partial T}{\partial t} = D_{th} \frac{\partial^2 T}{\partial x^2} \tag{1.3}$$

In order to solve this partial differential equation, a finite difference approach is adopted utilizing an Euler implicit central differencing scheme and evaluated using MATLAB® software. A detailed description and verification of this approach is provided in *Appendix B*. In designing the simulation, a layer is prescribed with the appropriate thermal properties, a thickness of $0.01\,m$, and an initial temperature of $300\,K$. The left and right surfaces of the layer are prescribed with convective heat transfer boundary conditions with respective free-stream temperatures of $500\,K$ and $300\,K$. During the course of the simulation, heat is conducted across the layer from left to right until a steady-state condition is reached.

The solutions for each case are presented in **Figure 1.2**, which illustrates the spatial distribution of temperature within each layer at incremental discrete times. In the figure, the blue lines in each chart depict the distribution of temperature at each discrete time, whereas the red line in each chart depicts the analytical steady-state temperature distribution.
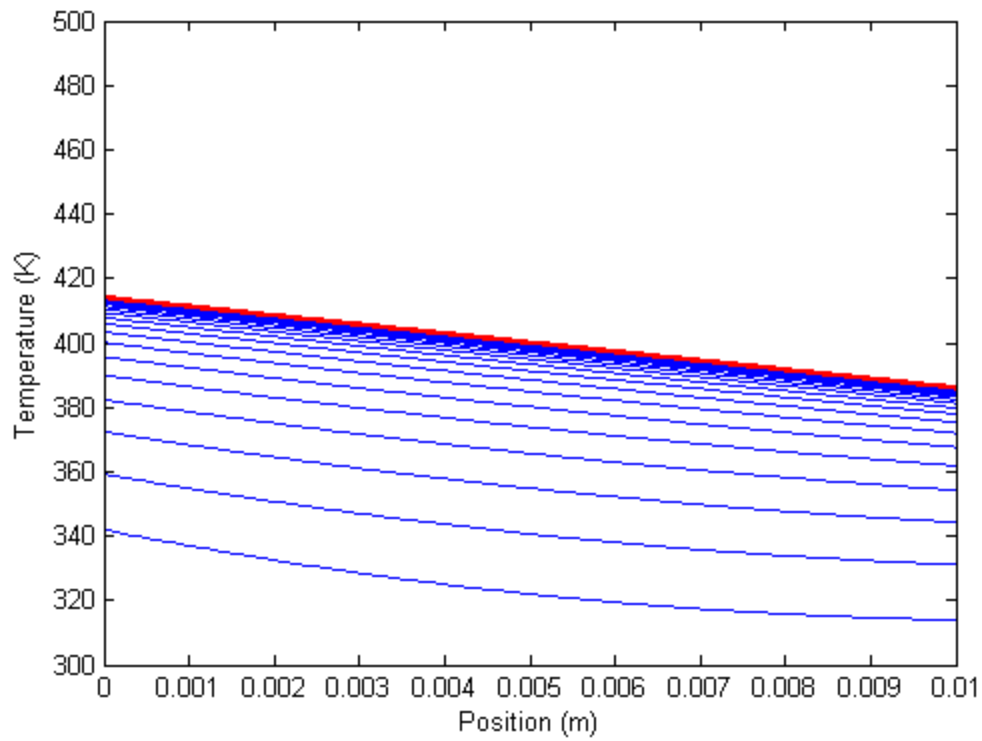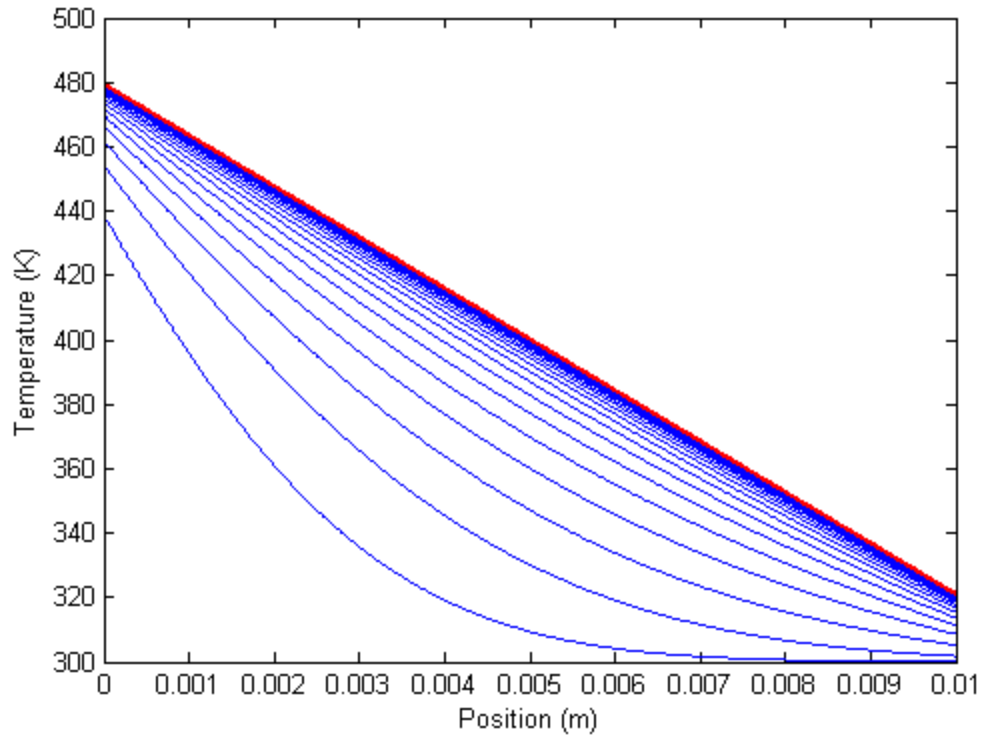
Figure 1.2: Distribution of temperature across a layer prescribed with the thermal properties of air (top) and liquid water (bottom) at selected discrete times

In viewing the results presented in **Figure 1.2**, it is imperative to note the difference between the time scales associated with the heating of each layer. For the air layer, solutions are plotted every $0.02\,s$ and a steady-state condition is reached after approximately $5\,s$. In comparison, solutions for the moisture layer are plotted every $300\,s$ and a steady-state condition is reached after approximately $7200\,s$. The air layer thus rises in temperature and reaches a steady-state condition significantly faster than the moisture layer. Despite this, it is important to note that the maximum temperature-rise occurring at the right surface of the air layer is significantly less than that for the moisture layer. This suggests that the transfer of heat through the air layer is initially faster than that through the moisture layer; however, after sufficient heating, the moisture layer transfers significantly more heat than the air layer.

Further analysis of these results reveals that they are consistent with the variations in the thermal properties of air and moisture. As shown in the figure, the steady-state temperature gradient across the air layer is significantly steeper than that across the moisture layer. This is primarily the result of the difference in the thermal conductivities of each layer, where an increase in thermal conductivity is expected to decrease the magnitude of the steady-state temperature gradient across the layer. This relationship between thermal conductivity and steady-state temperature gradient is consistent with the property values provided in **Table 1.1** and **Table 1.2**, where the thermal conductivity of air is significantly less than that of moisture.

Though not clearly shown in the figure due to the difference between the time scales associated with the heating of each layer, the rate of diffusion of heat across the air layer is significantly faster than that across the moisture layer. This heat diffusion

rate is characterized by the time delay between the temperature-rise at the exposure surface of the layer and the resultant temperature-rise at the opposite surface of the layer. The difference in the rates of heat diffusion across each layer is primarily the result of their differing thermal diffusivities, where an increase in thermal diffusivity is expected to increase the rate of heat diffusion across the layer. This relationship between thermal diffusivity and diffusion of thermal energy is also consistent with the property values provided in **Table 1.1** and **Table 1.2**, where the thermal diffusivity of air is significantly greater than that of moisture.

More clearly shown in the figure is the difference in the rate of temperature-rise at the exposure surface of each layer, which is significantly faster for the air layer than for the moisture layer. This is primarily the result of the difference between the thermal inertias of each layer, where an increase in thermal inertia is expected to decrease the rate of temperature-rise at the exposure surface. As with the other trends, this relationship between thermal inertia and rate of exposure-surface temperature-rise is consistent with the property values provided in **Table 1.1** and **Table 1.2**, where the thermal inertia of air is significantly less than that of moisture.

It is interesting to note the ratio of the rate of temperature-rise at the exposure surface to the rate of heat diffusion across each layer. For the air layer, the rate of temperature-rise at the exposure surface is faster than the rate of heat diffusion, as evidenced by the steep temperature gradients occurring throughout the layer during transient heating. In comparison, the rate of temperature-rise at the exposure surface of the moisture layer is slower than the rate of heat diffusion, as evidenced by the relatively flat and parallel temperature gradients that remain constant throughout the

simulation. The ratio of these rates is represented by the product of thermal inertia and thermal diffusivity, where an increase in this product is expected to favor heat diffusion over temperature-rise. This relationship is consistent with the property values provided in **Table 1.1** and **Table 1.2** in which the product of thermal inertia and thermal diffusivity for air is less than that for moisture.

The rate of temperature-rise at the exposure surface of each layer carries additional significance in that the flux of thermal energy entering each layer is a function of the difference between the exposure-surface temperature and the free-stream temperature on the exposure side of the layer. As the difference between these temperatures decreases, the heat flux entering the layer reduces. In a similar fashion, the heat flux leaving each layer is a function of the difference between the opposite-surface temperature and the free-stream temperature on the opposite side of the layer. At a steady-state condition, the heat fluxes entering and leaving each layer equate. These trends are illustrated in **Figure 1.3**, which provides the time evolution of the heat fluxes at the exposure and opposite surfaces of each layer.

For the air layer, whose exposure-surface temperature increases rapidly, the difference between the exposure-surface and free-stream temperatures decreases equally as rapidly. This results in the trend illustrated in **Figure 1.3**, in which the heat flux entering the air layer at the exposure surface quickly decreases. In comparison, the exposure-surface temperature of the moisture layer increases slowly, resulting in an equally slow reduction in the heat flux entering the moisture layer at the exposure surface. Because the heat flux entering each layer is directly related to the heat flux leaving each layer, these trends are equally represented at the opposite surface.
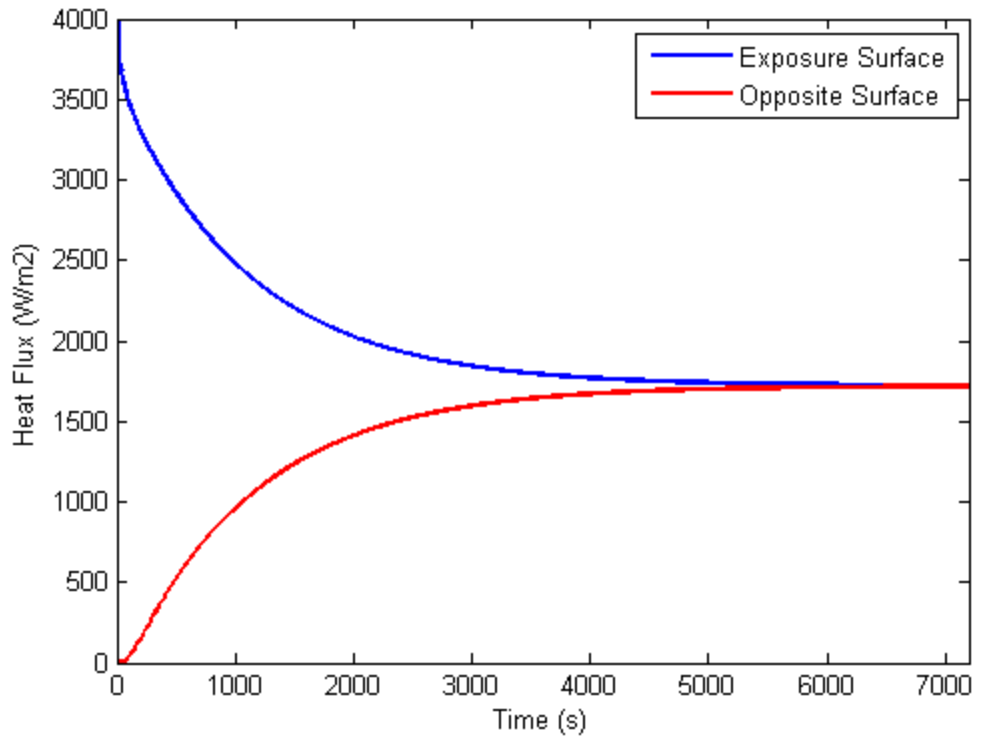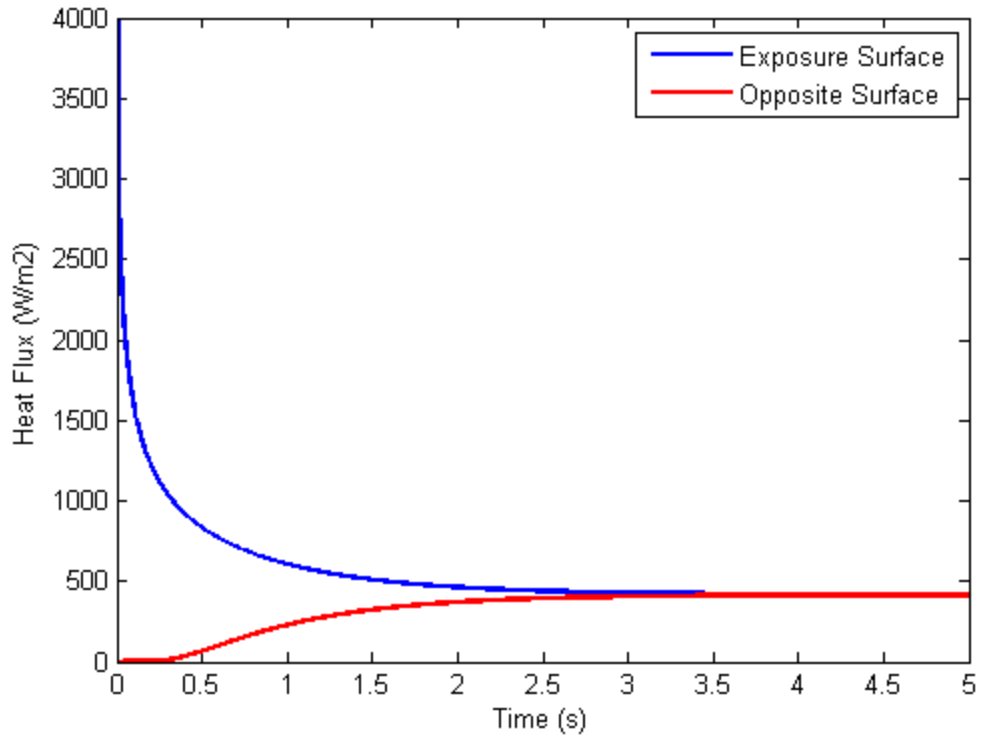
Figure 1.3: Time evolution of heat flux at the boundary surfaces of a layer prescribed with the thermal properties of air (top) and liquid water (bottom)

As shown in **Figure 1.3**, the time evolutions of the heat flux leaving the opposite surface of each layer differ significantly. This criterion characterizes the protective quality of each layer in that it provides a measure of the amount of heat felt on the opposite side of each layer for the prescribed thermal exposure conditions. The maximum heat flux leaving the air layer is significantly less than that leaving the moisture layer; however, a steady-state condition is achieved in the air layer much more rapidly than in the moisture layer. As a result, the heat flux leaving the moisture layer is initially less than that leaving the air layer, but eventually exceeds that leaving the air layer once a critical time is reached. Before this critical time, the moisture layer provides greater thermal protection than the air layer; afterwards however, the protective performance of the moisture layer rapidly decreases.

As clearly illustrated by the simulation results presented in **Figure 1.2** and **Figure 1.3**, the differences between the thermal properties of air and moisture significantly influence the transient heating of a garment layer. In reviewing these results, however, it is important to note the limitations of their applicability. The conditions utilized by the simulation characterize the transfer of heat through a single layer exposed to an elevated exterior temperature via convective boundary conditions. While this simulation is useful in illustrating the significance of the differences in the thermal properties of air and moisture, it does not accurately represent the complex boundary conditions present within a firefighter protective clothing garment. As such, the results of the simulation should not be construed to predict the actual difference in performance between the presence of air and moisture within firefighter protective clothing, and should rather be used for qualitative comparison only.

In addition to influencing the effective thermal properties of a garment, air contributes to the occurrence of convective heat transfer through its susceptibility to advection. Note that though moisture is also a mobile fluid, liquid moisture provides a minimal contribution to convection because it is typically bounded by the fibers of the garment. While moisture vapor is susceptible to advection, as shown in **Table 1.1** and **Table 1.3**, the thermal properties of air and steam are approximately equal for the temperature ranges typically encountered during firefighter operations. As a result, the convective contributions of water vapor are negligibly different from those of air.

As previously mentioned, convection occurs primarily within the air-gaps between adjacent garment layers. Convective flows within these air-gaps are induced by the buoyancy forces created due to the temperature gradients occurring across the air-gaps. Buoyancy forces are characteristically directed upward, in opposition to the gravitational force; therefore, the orientation of an air-gap has an underlying effect on the magnitude of convective heat transfer occurring across the air-gap.

Within vertical air-gaps, efficient convective flows occur as air circulates respectively upward and downward along the hot and cold sides of the air-gap [6]. Convective flows within bottom-heated horizontal air-gaps are also efficient, as air travels upward from the hot side of the air-gap toward the cold side of the air-gap, in the direction of heat flow [6]. Within top-heated horizontal air-gaps, inefficient convective flows occur as air travels upward from the cold side of the air-gap toward the hot side of the air-gap, against the flow of heat [6]. Of these cases, convective heat transfer is most efficient within vertical air-gaps and bottom-heated horizontal air-gaps, and significantly less efficient within top-heated horizontal air-gaps.

The magnitude of convective heat transfer across an air-gap is quantified by a convective heat transfer coefficient, whose value depends on a number of factors including the thickness and orientation of the air-gap, the thermal properties of air, and the local temperature gradient. Also of importance is the ratio of buoyancy forces to viscous forces within the air-gap, as quantified by a dimensionless parameter referred to as the Rayleigh number [6]. This Rayleigh number is directly related to another dimensionless parameter referred to as the Nusselt number, which quantifies the ratio of heat conduction to heat convection occurring across the air-gap [6]. The convective heat transfer coefficient, Nusselt number, and Rayleigh number are related by the following expression, where the arbitrary function, f, is determined by the geometry and orientation of the air-gap, and can be referenced from any appropriate heat transfer textbook [6].

$$\frac{h\delta}{\lambda} = Nu_\delta = f(Ra_\delta) \tag{1.4}$$

At the onset of convection, the Rayleigh number assumes a critical value that dictates the conditions for which convective and conductive heat transfer across the air-gap equate. From this critical Rayleigh number, it is possible to approximate the critical air-gap thickness at which the onset of convection occurs. This critical thickness is given by the following expression [6]. Note that for thin, horizontal air-gaps, the critical Rayleigh number is 1708, while for vertical air-gaps, the critical Rayleigh number is approximately 1000 [6].

$$\delta = \left(\frac{D_{th}\upsilon Ra_\delta}{g\beta\Delta T}\right)^{1/3} \tag{1.5}$$

24

Utilizing this expression and assuming an air-gap enclosed by adjacent layers at respective temperatures of $25°C$ and $125°C$, the critical air-gap thicknesses required to achieve convection in a horizontal and vertical air-gap are respectively $7.25\ mm$ and $6.07\ mm$. Because these thicknesses are relatively large in comparison to the typical air-gaps occurring between adjacent layers in a garment, the effects of convective heat transfer within firefighter protective clothing are typically neglected.

In addition to their contribution to convection, air-gaps provide a transparent medium through which radiant heat transfer occurs. Unlike convection, radiant heat transfer across an air-gap is independent of air-gap thickness and depends only on the absolute temperatures and optical properties of the surfaces enclosing the air-gap. Although radiation exhibits spectral and directional dependence as well, these effects are typically neglected due to their inherent complexity. While radiation is typically the dominant mode of heat transfer across an air-gap, it is also the most difficult to quantify. As a result, a detailed description of radiant heat transfer across an air-gap is avoided, though a simplified description of the relevant mechanisms is provided in *Appendix C*. This description also includes the derivation of an effective thermal conductivity for an enclosed air-gap, which combines the contributions of conductive, convective, and radiant heat transfer.

As the influence of air on the performance of firefighter protective clothing is compounded by contributions to convective and radiant heat transfer, the influence of moisture is similarly compounded by the latent heat of phase-change associated with evaporation and condensation. This latent heat dictates the amount of energy that must be respectively supplied to or removed from moisture in order for evaporation

25

and condensation to occur. Within a garment, the transfer of this latent energy occurs between the moisture and the garment; therefore, when evaporation and condensation occur, heat is respectively removed from and supplied to the garment.

Because the occurrence of evaporation removes thermal energy from a garment, the resulting cooling effect is beneficial to protective performance. It is important to note, however, that the moisture vapor created by this process is free to diffuse throughout the garment. Once this vapor relocates to a layer at a temperature below the saturation point of water, the occurrence of condensation returns that thermal energy back to the garment, negating any potential benefit provided by evaporative cooling. Because garment layers closest to the skin surface are typically at lower temperatures, condensation is more likely to occur at or near the skin surface.

Within a garment, the rate of mass diffusion of moisture vapor is roughly equal to the rate of heat diffusion by conduction; however, the rate of heat transfer by evaporation and condensation in comparison to these mechanisms is relatively instantaneous [6]. As a result, once moisture begins to condense on a surface, heat is delivered to that surface very quickly. The occurrence of condensation heat transfer within a protective garment is thus a dangerous condition that leads to a rapid rate of temperature-rise at or near the skin surface with limited forewarning.

In considering their influence on the effective thermal properties of a garment, their respective contributions to convective and radiant heat transfer, and the effects of evaporation and condensation, it is readily apparent that the presence of air and moisture within a garment of firefighter protective clothing significantly influences protective performance.

Previous research examining the performance of thermal protective clothing is widespread. Studies include the investigation of possible performance enhancements, the development of increasingly accurate heat and mass transfer models, and the determination of the applicability of standard test methods and results. The following studies summarize research that examines explicitly the influence of either moisture or the presence of air-gaps on the performance of thermal protective clothing.

<u>Moisture Related Research</u>

Research examining the effective thermal conductivity of wet clothing is presented by Takahashi et al [7]. This research focuses on the development of a heat transfer model for fabrics incorporating the effects of moisture and the geometric structure of woven fibers. Numerical predictions of effective thermal conductivity are then produced for multilayer garments with varying distributions of moisture content.

The heat transfer model proposed by Takahashi et al employs a three-dimensional heat conduction equation that neglects convection, radiation, and mass transfer. The model considers the individual thermal conductivities of fabric fibers, air, and moisture; and applies an effective thermal conductivity to the fabric based on the spatial distribution of these components. Additionally, the phase-state of the moisture and the shapes and contact areas of individual fibers are considered.

Based on the predictions of the numerical model, the effective thermal conductivity of a single-layer fabric is shown to increase slightly with rising fiber thermal conductivity and increase significantly with rising moisture content. For

multilayer fabrics, thermal conductivity is shown to vary throughout constituent layers as a function of moisture distribution and attains a maximum in the layer with the greatest moisture content. Takahashi et al conduct no experimental tests, though the numerical predictions are compared to data referenced from previous researchers. The scatter in this data is large, however, and only qualitative agreement between the trends of the simulation predictions and referenced data is suggested.

An additional study examining the effective thermal conductivity of wet fabrics is presented by Dias and Delkumburewatte [8]. This study focuses on the influences of the porosity of a fabric in addition to moisture, and includes the effects of moisture evaporation and condensation as reported by experimental measurements.

Dias and Delkumburewatte present a numerical simulation integrating a porosity model and a thermal conductivity model to predict the effects of varying moisture content on the effective thermal conductivity of a fabric. The porosity model utilizes the repeating unit cell of a knitted structure to predict the overall volume ratio of fiber to interstitial air within a fabric. The thermal conductivity model then utilizes the porosity model predictions to predict the relative thicknesses of fiber, moisture, and air occurring through the total thickness of the fabric. An expression relating the individual thermal conductivities of these components is then used to calculate an effective thermal conductivity for the fabric.

An experimental apparatus employing a parallel plate arrangement is used to validate the numerical predictions. This apparatus places a fabric sample between two copper plates with internal thermocouples and provides heat from below via an electric hotplate. Using the thermocouple measurements and the known thermal

conductivity of copper, temperatures at the upper and lower surface of the fabric are estimated. The steady-state temperature gradient across the fabric is then used to measure the effective thermal conductivity of the fabric.

Effective thermal conductivities predicted by the simulation are shown to decrease with increasing porosity at low moisture content and increase with increasing porosity at high moisture content. Thermal conductivity is additionally shown to increase with increasing moisture content for any porosity. Minimum thermal conductivity is observed for low moisture and high porosity, whereas maximum thermal conductivity is observed for high moisture and high porosity.

The numerical simulation is shown to significantly under-predict effective thermal conductivities as compared to experimental measurements. Dias and Delkumburewatte attribute this discrepancy to phase-change heat transfer, which occurs when water vapor condenses on the surface of the upper copper plate. This reasoning is supported by their observation of condensed water droplets on the upper copper plate after tests involving high moisture content. Despite the inaccuracy of the simulation predictions, the qualitative trends of thermal conductivity with varying porosity and moisture content agree well with the experimental measurements.

A study examining the coupled transport of heat and moisture in firefighter protective clothing during flash-fire exposures is presented by Chitrphiromsri and Kuznetsov [9]. This research utilizes a heat and mass transfer model originally developed by Chitrphiromsri in a PhD thesis [10], which combines the effects of conduction and radiation with the evaporation and diffusion of moisture through fabrics exposed to intense heat.

The presented model includes a one-dimensional heat diffusion equation that considers the effects of conduction and radiation through a multilayer garment, air-gap, and skin layer. Convection within the garment and air-gap are neglected. Three phases of moisture are considered including liquid moisture bounded by garment fibers, free liquid moisture, and moisture vapor. Transition between these states is modeled via an enthalpy of transition between bound and free liquid moisture and an enthalpy of vaporization between free liquid and vapor-phase moisture. The diffusion of moisture vapor through the garment and air-gap is considered as well.

The first four seconds of each simulation involve an exposure of the garment to a simulated flash-fire, with the simulation continuing for an additional minute to model a cooling period. The spatial distributions of temperature, moisture content, and vapor density are reported by the simulation at discrete times throughout the system. Additionally, the bio-heat transfer model developed by Pennes [11] is used in conjunction with the Henriques burn integral [12] to determine minimum exposure times to induce second and third-degree burn injury in the skin.

The results of the simulation suggest an oscillatory movement of moisture through the system. The initial moisture in the garment evaporates, diffuses into the air-gap toward the skin, and subsequently diffuses in the reverse direction toward the garment after cooling. Additional results indicate that the temperature in the skin layer continues to increase long after the thermal exposure ends and the garment and air-gap return to ambient temperature. The minimum exposure times to induce second and third-degree burn injury are examined for varying air-gap thicknesses, and suggest that thicker air-gaps offer longer minimum exposure times.

No experimentation is presented in the previously referenced report; however, an experimental validation and parametric study of the model developed by Chitrphiromsri is presented by Song et al [13]. The experimental setup utilized by Song et al mimics that of the numerical simulation and consists of a skin-simulant sensor protected from a thermal exposure by a fabric assembly. Two test configurations are conducted including positioning of the fabric directly in contact with the sensor, or separated from the sensor by an air-gap. Fabric assemblies representing firefighter protective clothing garments are tested including single, double, and triple-layer assemblies. These assemblies respectively consist of an outer shell; an outer shell and moisture barrier; and an outer shell, moisture barrier, and thermal liner.

Model predictions are shown to agree relatively well with experimental measurements for both contact and spaced configurations and for all three assemblies. An additional parametric study is conducted in which individual properties of the fabric are varied while holding other initial conditions constant. The effects of such variations are evaluated based on the resultant variations in the predicted minimum exposure time required to induce second-degree burn injury. Minimum exposure time is shown to increase with increased fabric density, decreased fabric thermal conductivity, increased fabric heat capacity, increased fabric thickness, decreased fabric initial temperature, and increased fabric moisture content.

Based on the research conducted by Takahashi et al and by Dias and Delkumburewatte, the presence of moisture in a fabric is shown to increase effective thermal conductivity, yielding an increase in the rate of heat transfer through the

fabric at steady-state. Additional results reported by Dias and Delkumburewatte indicate that the condensation of water vapor on a surface increases the rate of heat transfer to that surface. This occurs because the condensation of water vapor involves an immense latent heat of phase-change, which is delivered directly to the surface on which condensation occurs.

In contradiction to these results, research conducted by Song et al indicates that the presence of moisture in a protective fabric increases the thermal exposure time required to induce a second-degree burn injury in a layer of skin protected by the fabric. This improvement is attributed to the large density and heat capacity of water, which imply that more time is required to increase the temperature of a moist fabric as compared to a dry fabric. It should be noted that these results are derived for short exposures to an intense thermal insult and do not consider prolonged exposures.

The results reported by the previously referenced studies offer conflicting conclusions as to the influence of moisture on the performance of thermal protective fabrics. With respect to increasing moisture content, the trends observed by Takahashi et al and Dias and Delkumburewatte suggest reduced performance, whereas the trends observed by Song et al suggest improved performance. Interestingly, the reduction in performance suggested by Takahashi et al and Dias and Delkumburewatte is with respect to steady-state heat transfer, whereas the improvement suggested by Song et al is with respect to transient heat transfer.

It is important to note that the heat transfer model employed by Song et al neglects the effects of moisture condensation at the skin surface. As shown by Chitrphiromsri and Kuznetsov, the moisture contained within a fabric exposed to an

intense heat source evaporates and diffuses away from the heat source. With respect to a firefighter protective clothing system, this suggests that moisture in the clothing diffuses inward, toward the skin. Were the condensation of moisture to occur in such a system, it would occur at the skin. As previously referenced, the condensation of moisture on a surface significantly increases the rate of heat transfer to that surface. Coupling these results suggests that the presence of moisture in a garment of firefighter protective clothing carries an elevated risk of the occurrence of phase-change heat transfer to the skin via condensation. As this effect has not been studied in detail, further research is necessary.

As evidenced by the previously summarized studies, research investigating the influence of moisture on the performance of thermal protective fabrics is extensive, but still incomplete. Previous research has almost exclusively treated moisture content as an initial condition that is invariable with respect to time. Such research has yielded results that are at times contradictory with respect to whether moisture provides a benefit or a detriment to protective performance in either transient or steady-state conditions. While some studies have examined the coupled transfer of heat and moisture in a protective garment, little to no research has been performed investigating the influence of the skin surface. Specifically, the effects of perspiration and condensation have yet to be studied in detail.

Though the research presented in this thesis does not explicitly consider the effects of condensation, it presents a worthwhile investigation into the effects of perspiration. In this research, moisture is treated as a variable flux instead of a constant initial condition and is introduced to fabric assemblies from the skin surface.

Air-Gap Related Research

A study examining heat transfer across air-gaps is presented by Torvi et al [14], summarizing research that Torvi presents in a PhD thesis [15]. This study focuses on comparing the relative dominance of various modes of heat transfer within an air-gap, also analyzing the influence of air-gap thickness by introducing the idea of optimal air-gap thickness. Below this ideal thickness, the protective performance of an air-gap grows with increasing thickness, whereas above it, performance reduces with increasing thickness. This ideal thickness is attributed to convection, which both intensifies with increasing thickness and enhances heat transfer across the air-gap.

Several ideal air-gap thicknesses are presented in the report, each referenced from various other researchers, though few agreements among the proposed values are observed. These values range from as small as $2\ mm$ to as large as $18\ mm$, while some sources suggest that no such optimal thickness exists. The discrepancies among these values are attributed to the different methods with which they are determined including either horizontal or vertical orientation; however, a number of the sources neither specify their methods nor provide justification for their proposed values.

Unsatisfied with these discrepancies, Torvi et al utilize a numerical simulation and experimental setup to examine the influence of varying air-gap thickness. The simulation utilizes a heat transfer model that considers the effects of conduction, convection, and radiation within the air-gap via an effective thermal conductivity. For comparison, the experimental tests provide flow-field photographs visualizing the intensity of convection within a heated air-gap at various discrete thicknesses. These methods each consider horizontally oriented air-gaps heated from below.

Both the numerical and experimental methods predict the onset of convection to occur in air-gaps with a thickness of approximately 7 mm; however the magnitude of convective heat flux through the air-gap is shown to remain constant with increasing thickness. Conversely, the magnitude of radiant heat flux is shown to decrease steadily with increasing thickness and is also shown to be significantly greater than convective heat flux for all thicknesses. The reduction of radiant heat transfer with increasing thickness is attributed to the increasing amount of radiant energy lost to the surroundings that occurs as the test sensor and fabric separate.

Torvi et al attribute the observation of constant convective heat transfer with increasing air-gap thickness to the realization that the magnitude of convective heat transfer is determined by the rate of transmission of thermal energy across the air-gap via convection, not the intensity of the convective flow field. Though the convective eddies in the air-gap are shown to intensify with increasing thickness, this effect is offset by the increasing distance those eddies must carry thermal energy. The result is an approximately constant convective heat flux over a range of varying air-gap thicknesses. Based on these results, Torvi et al report the existence of no optimal air-gap thickness and suggest radiation as the dominant mode of heat transfer through an air-gap.

Research examining the effects of thermal shrinkage within aramid fabrics exposed to intense thermal insults is presented by Zhu et al [16]. Aramid fabrics are commonly used in the materials of firefighter protective clothing garments and such shrinkage can result in the compression of the garment against the body. This research focuses on the determination of the consequences of such compression.

In their research, Zhu et al utilize separate experimental devices employing planar and cylindrical geometries, where cylindrical geometries are chosen to better measure the effects of thermal shrinkage. Each apparatus consists of a skin-simulant sensor separated from a radiant heat source by a layer of fabric, which is either positioned in contact with the sensor or separated from the sensor by an air-gap. Several flame-resistant fabrics are tested including aramid fabrics such as Nomex$^®$ III and non-aramid fabrics such as Flame Retardant Cotton. Each test involves a thermal exposure of approximately 20 seconds to a radiant heat flux of 21 kW/m^2.

The results of each test are evaluated based on a critical time to reach second-degree burn injury assuming skin located at the position of the sensor. Calculation of this critical time is conducted using the time-temperature profile measured by the sensor and applying the Henriques burn integral and a thermal wave model of bio-heat transfer based on the Pennes skin model. With no fabric positioned in the test apparatus, results between the planar and cylindrical geometries are shown to be identical, indicating that the two devices yield consistent and comparable results.

For non-aramid fabrics, no significant variation in minimum exposure time is observed between planar and cylindrical geometries. This suggests that non-aramid fabrics do not suffer from thermal shrinkage. While aramid fabrics tested in the contact-orientation show consistent results between the two geometries, aramid fabrics tested in the spaced-orientation measure reduced minimum exposure times for cylindrical geometry as compared to planar geometry. This suggests that aramid fabrics suffer a decline in performance due to thermal shrinkage and the resulting reduced thickness of the air-gap separating the sensor and fabric.

36

Based on the research conducted by Torvi et al and by Zhu et al, it is readily apparent that air-gaps provide a noticeable improvement to the performance of thermal protective fabrics. This improvement is the result of the low thermal conductivity of air, yielding a reduced rate of heat transfer through the air-gap. Torvi et al suggest that the thermal resistance provided by an air-gap increases with increasing air-gap thickness. This trend is attributed to the decreasing magnitudes of conductive and radiant heat transfer through the air-gap that occur with increasing thickness. Additionally, convective heat transfer is found to remain constant with increasing thickness, despite the intensification of convective eddies.

With respect to firefighter protective clothing, residual air-gaps existing between adjacent layers within the garment and between the garment and skin dramatically improve protective performance. As suggested by Zhu et al, such air-gaps are negated due to the effects of thermal shrinkage, significantly increasing heat transfer through the garment and raising the risk of compression burns. In order to ensure the presence of these protective air-gaps, it is necessary to implement an effective method of creating a dedicated air-gap within the garment that resists compression.

As with moisture related studies, previous research investigating the influence of air-gaps on the performance of thermal protective fabrics is extensive. This research is nearly unanimous in suggesting the significant improvement to protective performance provided by air-gaps and increasing air-gap thickness; however, the air-gaps that are examined are almost exclusively those occurring between a test sensor and a layer of fabric, not those between two fabric layers.

For the type of air-gap studied by Torvi et al, radiant heat transfer occurs between the fabric, test sensor, and surroundings. Radiation exchange between the fabric and test sensor decreases with increasing thickness of the air-gap because an increasing amount of radiant energy is lost to the surroundings as the fabric and test sensor separate. For an enclosed air-gap between two fabric layers, radiant heat transfer occurs only between the two layers. Radiation exchange between these layers does not decrease with increasing thickness because the two layers exchange radiant energy only with each other regardless of their separation distance. Though a small amount of radiant energy is absorbed by the interstitial air in the air-gap, this effect is negligible over the small thicknesses of a typical air-gap. Because the mechanisms of radiant heat transfer within these two types of air-gaps are fundamentally different, additional research is necessary to examine the effects of increasing thickness for air-gaps between two fabric layers.

In addition, little to no research has been performed investigating the implementation of a dedicated air-gap within a protective garment. This is surprising considering the well-established effectiveness of air-gaps coupled with other research suggesting the negation of air-gaps resulting from compression and thermal shrinkage. Especially noteworthy is that no previous studies have been conducted examining the specific application of thermally activated shape-memory materials to firefighter safety. The research presented in this thesis thus provides a promising investigation with which to examine the applicability of shape-memory materials to a firefighter protective clothing garment, the results of which could potentially propose effective improvements to garment performance.

Research conducted in partnership with that appearing in this thesis is presented by Perry [17] and Hendrickson [18] in respective MS theses. This research is based on previous work by Spangler [19] and focuses on the development of a MATLAB® software based numerical simulation able to analyze and predict the performance of firefighter protective clothing. The simulations developed by Perry and Hendrickson utilize input parameters including the thermal properties of the layers comprising a garment of interest and boundary conditions including exposure and body temperatures. From these input parameters, each simulation generates a time evolution for the temperature distribution within the inner layers of the garment.

While the simulations developed by Perry and Hendrickson are similar in execution and design, their individual scopes differ. Perry's research focuses on the influence of perspiration moisture within firefighter protective clothing, whereas Hendrickson's research focuses on the influence of static and expanding air-gaps.

Perry proposes a one-dimensional heat conduction model that neglects the effects of convection and radiation, and includes an energy source term characterizing the latent heat of phase-change associated with moisture evaporation. This model assumes that upon evaporation, moisture vapor immediately escapes the garment and thus moisture condensation is neglected. A finite difference approach employing a Crank-Nicolson, implicit central differencing scheme is utilized to solve the model numerically. This approach utilizes a tri-diagonal matrix formulation to evaluate the governing partial differential equation of the heat transfer model in terms of a discretized spatial and temporal grid.

As referenced from research presented by Schneider [20], Perry utilizes a regain factor to quantify the relative concentration of moisture within each garment layer, defining regain as the mass ratio of moisture to fabric within a particular layer. In the proposed model, regain is tracked as a spatially averaged quantity and is considered uniform within each layer. Temporal variations of regain are evaluated according to specified boundary conditions including the rate of moisture delivery to the garment from the skin surface and the occurrence of evaporation. Based on this regain factor, the effective thermal conductivity, density, and heat capacity of each layer is modified to account for the presence of moisture.

Hendrickson proposes a one-dimensional heat conduction model similar to that developed by Perry in that it neglects convection and radiation for solid material layers; however, an effective thermal conductivity referenced from Torvi [14] is introduced for air-gap layers, accounting for the effects of convection and radiation within the air-gap. Also similar to Perry, Hendrickson utilizes a finite difference approach employing a Crank-Nicolson, implicit central differencing scheme to solve the proposed model numerically in terms of a discretized spatial and temporal grid.

Hendrickson's model features an expanding air-gap layer in that the thickness of the discretized spatial grid cells located within the air-gap are allowed to increase during the course of the simulation. A thickness ratio is introduced to model this effect, defining the ratio of the air-gap thickness at a particular time step to the initial air-gap thickness at the initiation of the simulation. According to Hendrickson, this modification to the model's spatial discretization during the course of the calculation significantly alters the formulation of the governing heat transfer equation, resulting

in the required application of a variable time factor in order to transpose the predicted temperatures in simulation time to those that coincide with physical time.

The experimental data appearing in this thesis are used to validate the heat transfer models developed by Perry and Hendrickson. In performing such validations, experimental temperature measurements serve as the exposure and body temperature boundary conditions for the models. From these boundary conditions, the models are shown to predict an internal garment temperature distribution that matches the experimental data, within the uncertainty of the measurements. As shown in their respective works, the models developed by Perry and Hendrickson both produce sufficient agreement between simulation predictions and experimental data and are appropriately validated. While some deviations are observed, these discrepancies are documented to lie within the limitations of the respective models.

Research continuing that conducted by Perry and Hendrickson, in addition to that presented in this thesis, is presented by Yates [21]. In this research, Yates proposes an integrated numerical simulation combining the models developed by Perry and Hendrickson. This integrated simulation serves to predict the combined influences of moisture and air-gaps on the performance of firefighter protective clothing for conditions that are not easily imitated with laboratory testing.

Additional research conducted by Yates examines the full-scale performance of firefighter protective clothing with the implementation of a shape-memory material derived expanding layer for exposures to live flash fire conditions. At the time of publication of this thesis, result analysis for the research conducted by Yates remains incomplete; therefore, a detailed discussion of such results is not included.

Chapter 2 : Methods and Procedures

All experiments are conducted using a custom-designed test apparatus combining a sweating guarded hotplate with a coupled fluid supply system, a radiant panel heat source, temperature control system, and data acquisition system. A photograph illustrating the test apparatus is provided in **Figure 2.1**.
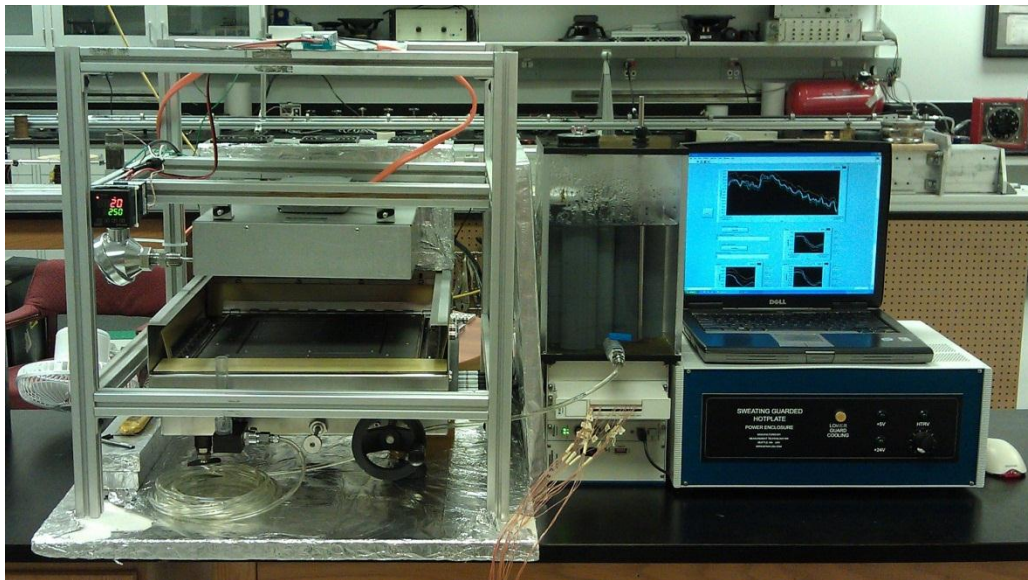
Figure 2.1: Test apparatus integrating multiple device systems

The sweating guarded hotplate device, designed by Measurement Technology Northwest, serves as the central component of the apparatus. The surface of this device is $310\ mm$ by $310\ mm$ in size and serves as the baseplate on which samples rest during testing. This baseplate features an integral sweating capability utilizing a porous wicking mechanism to seep moisture into the samples. Pores on the surface of the baseplate are spaced roughly $65\ mm$ apart. A pair of photographs demonstrating the sweating capability of the baseplate is provided in **Figure 2.2**.
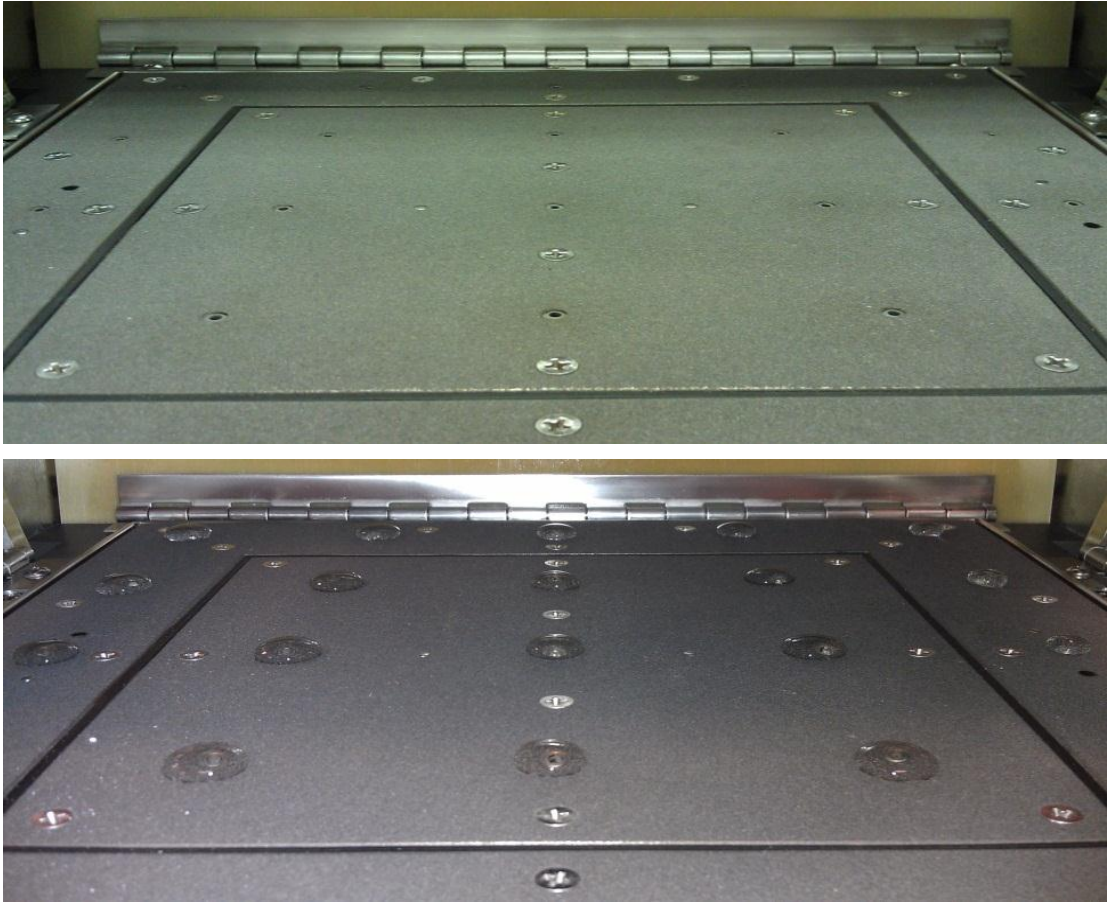
Figure 2.2: Baseplate surface of the sweating guarded hotplate for dry (top) and wet (bottom) conditions

Moisture is delivered to the sweating guarded hotplate via a gravity-driven fluid supply system consisting of a fluid reservoir, fluid level indicator, and a length of $5\ mm$ diameter connective tubing. A photograph displaying the fluid supply system is provided in **Figure 2.3**. The fluid reservoir is an airtight container with an internal cross-sectional area of $185\ mm$ by $185\ mm$ and an internal height of $285\ mm$. At the bottom of the fluid reservoir is a check valve to which the connective tubing attaches. By opening the check valve, fluid is allowed to flow from the reservoir via the connective tubing to the fluid level indicator. The fluid supply system is activated or deactivated respectively by opening or closing this check valve.
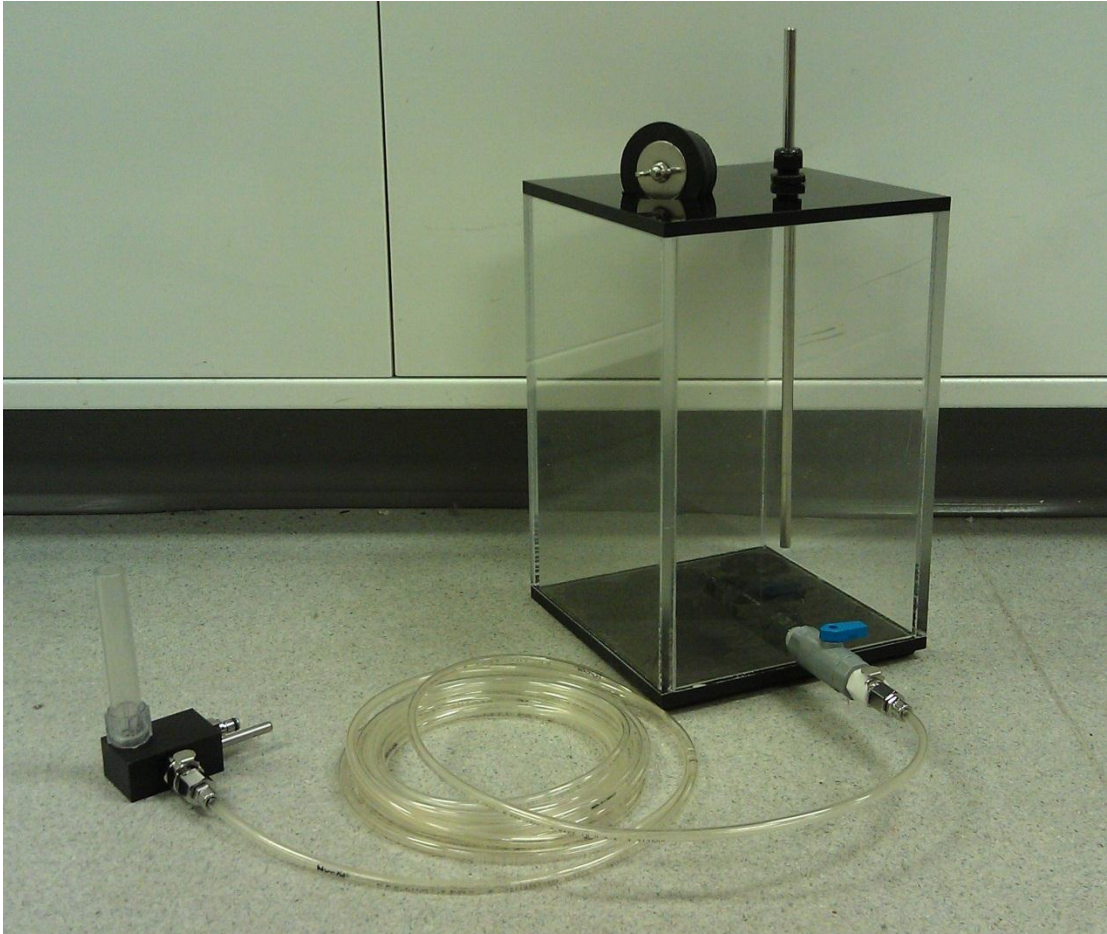
Figure 2.3: Fluid supply system consisting of a fluid reservoir, fluid level indicator, and connective tubing

On the top surface of the reservoir is a $60\ mm$ diameter, re-sealable opening used for refilling the contents of the container and a second opening occupied by a $360\ mm$ long, $5\ mm$ diameter stainless-steel tube. This tube is held in place by a tightening nut that provides an airtight seal around the tube while permitting the tube to be moved upward and downward through the opening. This movement allows the relative depth of the tube into the reservoir to be varied.

Because the fluid reservoir is hermetically sealed, the stainless-steel tube provides the only opening into the reservoir and the only means for pressure

equalization between the reservoir interior and exterior. As fluid flows out of the reservoir, the pressure inside the reservoir is reduced, drawing air into the reservoir via the stainless-steel tube. The relative elevation between the bottom of the stainless-steel tube and the point of outward fluid flow thus determines the magnitude of the static pressure driving fluid out of the reservoir. By adjusting the elevation of the tube, this static pressure can be varied allowing for an adjustable rate of fluid flow through the system.

The fluid level indicator is an approximately $100\ mm$ long, $10\ mm$ diameter, vertically oriented tube that connects to the bottom of the sweating guarded hotplate and delivers fluid to the bladder beneath the baseplate surface. This tube is open at the top and provides a visualization of the static pressure driving fluid into the sweating guarded hotplate. A photograph illustrating the fluid level indicator is provided in **Figure 2.4**. Together with the adjustable elevation of the stainless-steel tube, the fluid level indicator is used to vary the rate of fluid flow through the system by monitoring the relative elevations of the fluid in the fluid level indicator and the surface of the baseplate. Adjacent to the fluid level indicator, on the side of the sweating guarded hotplate, is a priming pump that serves as a manual action lever used to pump fluid through the system.

A standard metric ruler is attached to the front surface of the fluid reservoir and is used to monitor the change in fluid level that occurs during each test. Additionally, several solid-core PVC cylinders, approximately $200\ mm$ long and $52\ mm$ in diameter, are placed inside the fluid reservoir. A photograph illustrating typical cylinders is provided in **Figure 2.4**. These cylinders decrease the cross

sectional area of the reservoir, increasing the rate at which the fluid level drops while fluid is flowing. This allows easy measurement of the change in fluid level that occurs over the duration of a test. Note that the fluid used for all tests is deionized water at ambient temperature.
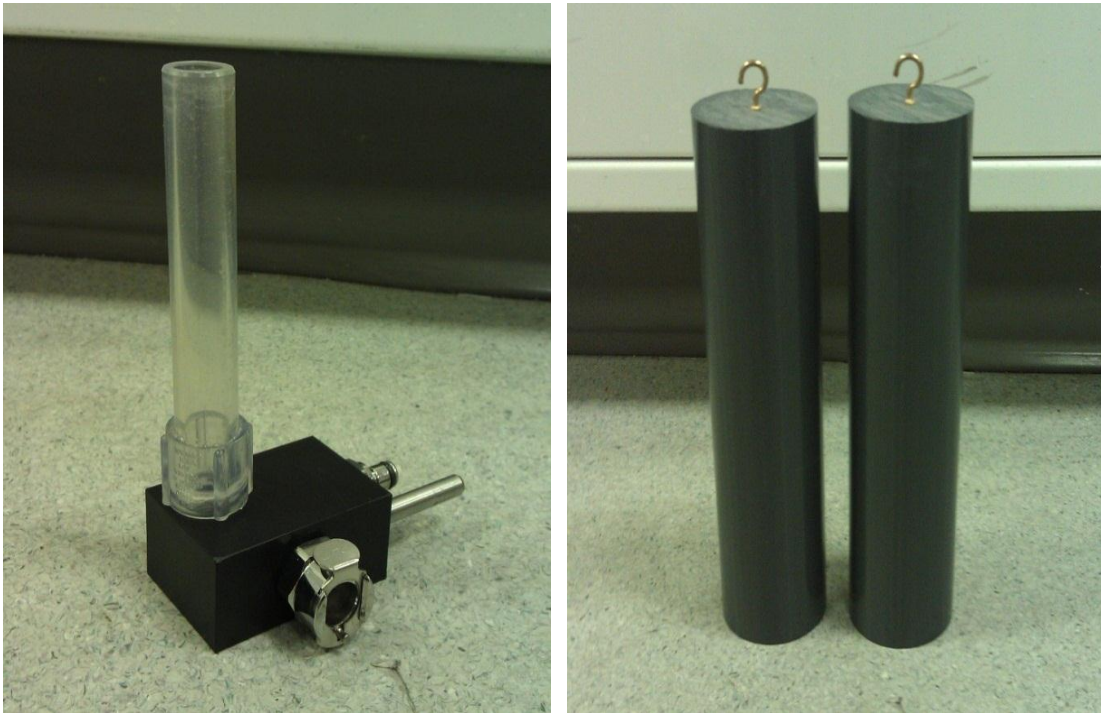
Figure 2.4: Fluid level indicator (left) and solid-core PVC cylinders (right) utilized by the fluid supply system

Directly above the baseplate of the sweating guarded hotplate is a Chromalox wide-area radiant panel, Model CPH-1224. This radiant panel serves as the thermal exposure source for each test and is connected to a temperature based control system, which provides a variable time-temperature profile and adjustable temperature setting. The $305\ mm$ by $305\ mm$ surface of the radiant panel is suspended $150\ mm$ above the baseplate by a custom-built slot steel support frame. A photograph displaying an underside view of the radiant panel is provided in **Figure 2.5**.

The output power of the radiant panel is controlled using an OGDEN microprocessor based temperature controller, Model ETR-9100. This controller utilizes a Type-J thermocouple probe and a solid-state relay to respectively monitor the air temperature directly beneath the panel and control the supply voltage to the panel. The thermocouple probe is positioned 5 mm beneath the center of the panel surface. Photographs depicting the temperature controller and the thermocouple probe are provided in **Figure 2.5**.

Figure 2.5: Radiant panel (top), thermocouple probe (bottom-left), and temperature controller (bottom-right) used to produce variable thermal exposures

Before the initiation of each test, a temperature setting is manually assigned using the temperature controller. During testing, the controller monitors the real-time temperature measurements of the thermocouple probe and regulates the supply voltage to the radiant panel accordingly. If the temperature measured by the probe is less than the assigned temperature, the supply voltage is increased, increasing the power of the radiant panel. Similarly, if the temperature measured by the probe is greater than the assigned temperature, the radiant panel is powered down, allowing convective cooling to decrease the probe temperature. By adjusting the supply voltage, the temperature controller regulates the output power of the radiant panel such that the assigned temperature is quickly achieved and subsequently maintained.

Because of the time delays associated with the latencies of the thermocouple measurements and the voltage regulation of the temperature controller, the resulting thermal exposure profiles are not perfectly constant. These inconsistencies produce variations in the heat flux incident on the samples during testing. Variable thermal exposures are desirable in that they allow the experiments to measure the effects of such variations on sample performance. Such variations are also characteristic of those experienced by firefighters during realistic fire exposures and are representative of the actual conditions in which firefighter protective clothing is used.

While it is possible to utilize a robust control method that produces a perfectly constant heat flux or temperature profile, such an implementation removes the temporal variability from the test method. As supported by the previous statements, this reduces both the profundity of the test results and the applicability of the test method to the conditions it is attempting to imitate.

The variable thermal exposures are disadvantageous in that they introduce additional difficulty to the analysis of the test results because thermal exposures are not constant among multiple tests. There is thus an inherent difference in the performance of comparable samples caused solely by thermal exposure variability. In order to alleviate this issue, it is necessary to distinguish the differences in performance caused by thermal exposure variability from those caused by sample alterations. Without such an analysis, it would be impossible to compare accurately the relative performance of different samples. The proposed solution to this issue is simple and is discussed in detail later in the analysis.

Data collection during testing is achieved via an array of 28 Omega$^®$ precision fine-wire Type-K thermocouples. The thermocouple wires utilized for testing are $0.13\ mm$ in diameter and insulated with a Teflon$^®$ insulation coating. Each thermocouple is labeled with a sequential numeral designation, numbered 1 through 28, such that the measurements of individual thermocouples are identifiable. The thermocouple wires are connected to a National Instruments *NI SCXI-1303* data acquisition system, which utilizes a standard Dell laptop computer running NI LabVIEW$^®$ software to visualize and record measured data.

Raw measurements from each thermocouple are averaged using a progressive temporal filter that gathers 100 temperature measurements per second and, once every second, averages those 100 measurements together. This process produces a time-averaged temperature measurement for each thermocouple that is updated and recorded once per second. This resolution of measurements is more than adequate to capture the temporal variations in temperature observable in the samples.

2.2: Samples and Materials

All samples utilize common firefighter protective clothing materials combined to form multilayered assemblies. The individual layers of these assemblies are square pieces of material roughly 350 mm by 350 mm in size. These layers are unattached and can be inverted and rearranged with respect to one another to construct varying assembly configurations. Once finalized, assembly configurations remain constant, utilizing the same collection of materials in the same orientation throughout testing to ensure consistent results.

Sample materials are provided by Lion Apparel from several currently available firefighter protective clothing models. These materials include two outer shell variants, *Fusion* and *PBI Matrix*; two moisture barrier variants, *Crosstech* and *RT-7100*; and five thermal liner variants, *C-Liner*, *K-Liner*, *Semper-Dri*, *V-Caldura*, and *X-Liner*. Of the thermal liner variants, *C-Liner* and *X-Liner* are split-layered, whereas *V-Caldura*, *K-Liner*, and *Semper-Dri* are traditionally layered. The thermal liner variants consist of different combinations of four primary materials including *Glide* and *Chambray* facecloth materials, and *E89-715M* and *E89-723DWR* insulation materials. Of these materials, the *Chambray* facecloth material and the *E89-715M* insulation material are treated with a moisture resistant coating, making them impermeable to moisture.

In addition to standard layers including an outer shell, moisture barrier, and thermal liner, each assembly also includes a shirt layer and a radiation shield layer. The shirt layer is the innermost layer of each assembly and consists of a commonly available Hanes® 100% cotton undershirt amended to match the dimensions of the

other layers. This shirt layer simulates a layer of underclothing worn beneath the protective garment. The radiation shield is the outermost layer of each assembly and consists of a single layer of *Fusion* outer shell material. The radiation shield serves to absorb the heat emitted by the radiant panel such that a purely conductive thermal boundary condition is approximated at the outer surface of the assembly. Additionally, the radiation shield prevents the interference of radiant effects on the measurements of the thermocouples positioned atop the outer shell layer.

In addition to the materials provided by Lion Apparel, several additional custom materials are utilized for specific applications. Suspension mounts are used to produce static air-gaps between assembly layers. These mounts are constructed using $12\ mm$ thick steel bars welded to form square frames $270\ mm$ by $270\ mm$ in size. Four $4\ mm$ diameter holes spaced roughly $50\ mm$ apart are drilled along each of the four sides of a frame and Kevlar® thread is woven through them in an alternating diagonal cross pattern. The thread ends are tightened and tied together to form a taut grid on which assembly layers are elevated and supported. Each frame provides a suspension thickness of $7\ mm$, with multiple frames being utilized to achieve increasing thickness. A photograph of a typical frame is provided in **Figure 2.6**.

In addition to the static air-gap frames, layer assemblies implementing sewn pockets of shape-memory material rings (SMR) are used to produce thermally activated, expanding air-gaps between assembly layers. A nickel-titanium alloy (*NITINOL*) manufactured by Memry Corp. is chosen as the shape-memory material for its efficient shape-memory effect useable in firefighter operation conditions. Figure-eight shaped rings are fashioned from a $0.762\ mm$ diameter wire of this alloy

with each loop of the figure eight forming a circle approximately $55\ mm$ in diameter. A crimp connection is used to attach the two loops of the figure eight and prevent the unraveling of the ring.
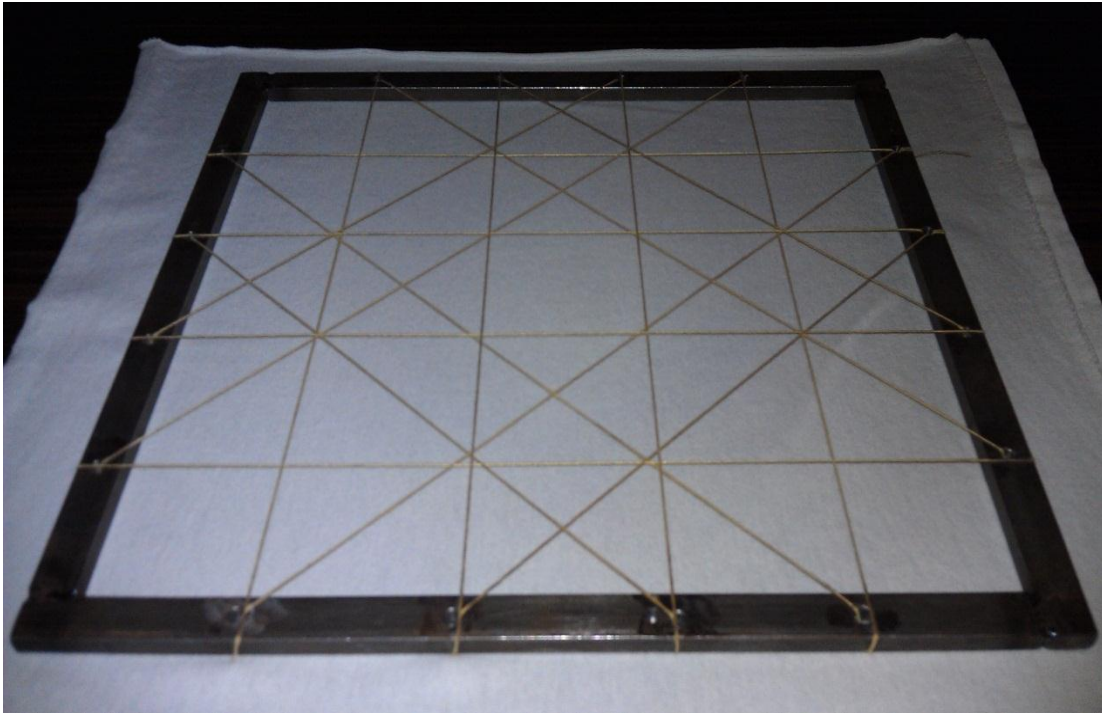
Figure 2.6: Typical static air-gap frame with woven Kevlar® thread

Two activation temperatures triggering the transformation of the shape-memory rings are utilized. These include austenite start temperatures of roughly $50°C$ and $90°C$ and respective austenite finish temperatures of roughly $70°C$ and $110°C$. In the martensite phase at room temperature, the rings are pliable and flat with both loops of the figure eight lying in the same plane. Upon activation and transformation to the austenite phase, the rings bend at the loop connection point producing a butterfly shape in which the two loops lie in mutually orthogonal planes. A pair of photographs illustrating a typical shape-memory ring for both inactivated and activated conditions is provided in **Figure 2.7**.
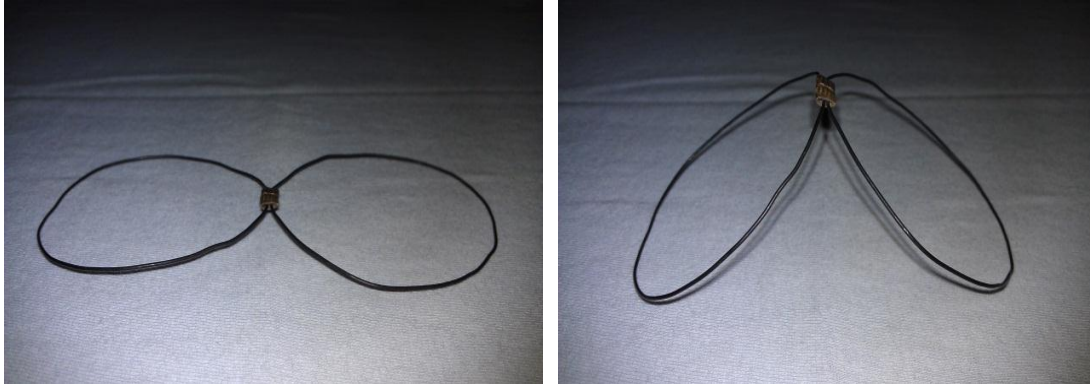
Figure 2.7: Typical shape-memory ring for inactivated (left) and activated (right) conditions

Each shape-memory ring is sewn into a pocket roughly 140 mm by 70 mm in size fashioned between two layers of *Chambray* facecloth material. In total, eight of these pockets are filled, forming a 280 mm by 280 mm square array of pockets with two rows and four columns. The rings are oriented within the pockets such that the loop connections alternatingly deflect upward or downward in adjacent pockets upon activation. A diagram depicting this alternating pattern is provided in **Figure 2.8**. Note that in the diagram, black dots indicate points on the rings that deflect upward upon activation.

The transformation of the shape-memory rings within the expanding layer produces a separation effect in which the contact points of the rings push against the two layers surrounding the expanding layer. This separation effect produces air spaces within and between the shape-memory ring pockets, effectively establishing an air-gap layer between the two surrounding layers. Due to the shape-memory effect based actuation, the establishment and expansion of this air-gap is entirely thermally induced. A pair of photographs illustrating a typical expanding layer for both inactivated and activated conditions is provided in **Figure 2.9**.
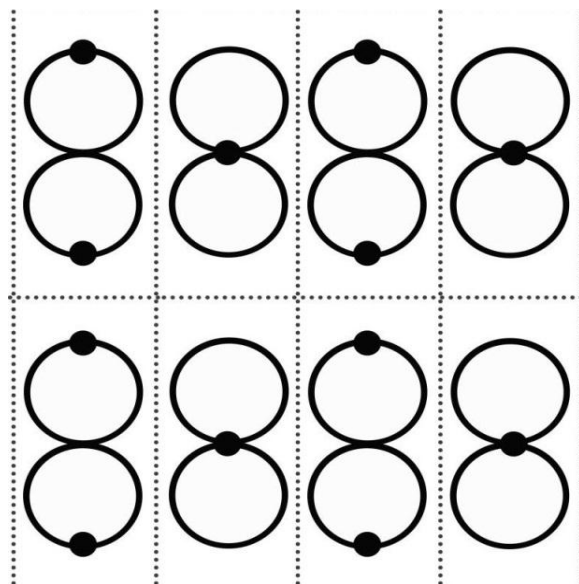
Figure 2.8: Diagram of alternating ring orientation within expanding layer pockets

Figure 2.9: Typical expanding layer for inactivated (top) and activated (bottom) conditions

A full listing of all materials used to construct the finalized sample assemblies is provided in **Table 2.1**. This table gives the names of each material categorized by material type and includes each material's average thickness and mass. Thickness and mass data for the firefighter protective clothing materials are as reported by Lion Apparel, while data for the custom materials are as measured.

Table 2.1: Listing of materials constituting individual sample assembly layers

Layer Name	Material	Thickness (mm)	Mass (kg/m^2)
Radiation Shield	*Fusion*	0.381	0.243
Outer Shell	*Fusion*	0.381	0.243
	PBI Matrix	0.406	0.247
Moisture Barrier	*Crosstech*	0.381	0.166
	RT-7100	0.762	0.156
Thermal Liner	*C-Liner*	1.016	0.275
	K-Liner	1.473	0.251
	Semper-Dri	1.499	0.231
	V-Caldura	1.575	0.278
	X-Liner	1.600	0.326
Shirt	Hanes® 100% cotton undershirt	0.457	0.164
Air-Gap	Static Air-Gap Frame	7.000	0.008[1]
SMR Assembly	2 × *Chambray* with Shape-Memory Rings	0.458[2]	0.337[3]

---

[1] The listed mass for the *Air-Gap* layer considers the mass density of air at ambient temperature.
[2] The listed thickness for the *SMR Assembly* layer neglects the contribution of the shape-memory rings.
[3] The mass of a single shape-memory ring is 1.30 grams.

Assemblies are designated by an alphanumeric label specifying constituent materials and the test series in which they are utilized. Test series include *Lion*, *Static Air-Gap*, *Moisture*, and *Expanding Air-Gap*. A description of the nomenclature used by assembly labels is provided in **Table 2.2**. A full listing of all assemblies, including component layers and thickness and mass data is provided in *Appendix D*.

**Table 2.2**: Listing of nomenclature designating individual sample assemblies

L-	*Lion* series assembly
A-	*Static Air-Gap* series assembly
M_s-	*Moisture* series assembly with split-layered thermal liner
M_t-	*Moisture* series assembly with traditionally layered thermal liner
E_o-	*Expanding Air-Gap* series assembly with outer placement of expanding layer
E_i-	*Expanding Air-Gap* series assembly with inner placement of expanding layer
-C	Designation for *Lion* series specifying a *C-Liner* thermal liner
-K	Designation for *Lion* series specifying an *K-Liner* thermal liner
-S	Designation for *Lion* series specifying a *Semper-Dri* thermal liner
-V	Designation for *Lion* series specifying a *V-Caldura* thermal liner
-X	Designation for *Lion* series specifying a *X-Liner* thermal liner
-F	Designation for *Lion* series specifying a *Fusion* outer shell
-P	Designation for *Lion* series specifying a *PBI Matrix* outer shell
-T	Designation for *Lion* series specifying a *Crosstech* moisture barrier
-R	Designation for *Lion* series specifying an *RT-7100* moisture barrier
-0	Designation for *Static Air-Gap* series specifying zero-layer air-gap
-1	Designation for *Static Air-Gap* series specifying one-layer air-gap
-2	Designation for *Static Air-Gap* series specifying two-layer air-gap
-4	Designation for *Static Air-Gap* series specifying four-layer air-gap
-D	Designation for *Moisture* series specifying dry test conditions
-W	Designation for *Moisture* series specifying wet test conditions
-∅	Designation specifying inclusion of no shape-memory rings
-50	Designation specifying $50°C$ activation shape-memory rings
-90	Designation specifying $90°C$ activation shape-memory rings

2.3: Data Collection

The methods and procedures followed for data collection during each test are as follows. Prior to the initiation of each test, material layers belonging to the assembly of interest are gathered and assembled. The completed assembly is then placed on the baseplate surface of the sweating guarded hotplate and thermocouples are positioned between each layer.

Four thermocouples are positioned between each layer at the corners of a square pattern roughly $75 \, mm$ by $75 \, mm$ in size, located at the center of each layer. For each additional layer, the orientation of this square pattern is rotated 45 degrees to ensure that thermocouples positioned on any particular layer do not lie directly above or below those on adjacent layers. This arrangement prevents the stacking of thermocouples in the same position from significantly adding to the overall thickness of the assembly. A photograph and accompanying diagrams illustrating thermocouple positioning is provided in **Figure 2.10**. In the diagrams, black and red dots respectively represent thermocouple positions for odd and even layers.

Thermocouples numbered 1 through 4 are positioned between the baseplate and the first layer of the assembly. Thermocouples numbered 5 through 8 are positioned between the first and second assembly layers, 9 through 12 between the second and third layers, and so on until thermocouples are appropriately positioned between all assembly layers. The final group of four thermocouples is always positioned between the outermost layer of the assembly and the radiation shield. Depending on the number of layers present in an assembly, not all 28 thermocouples need be used during a particular test.
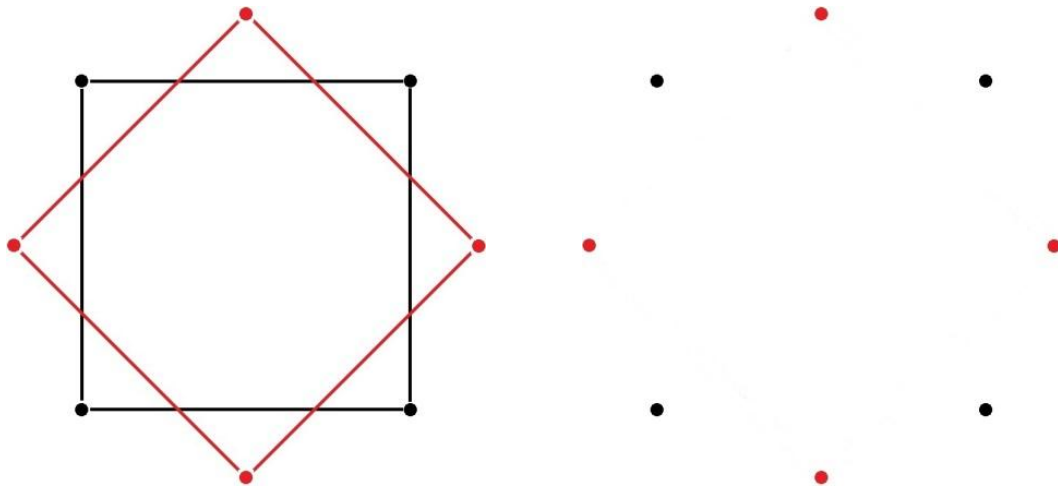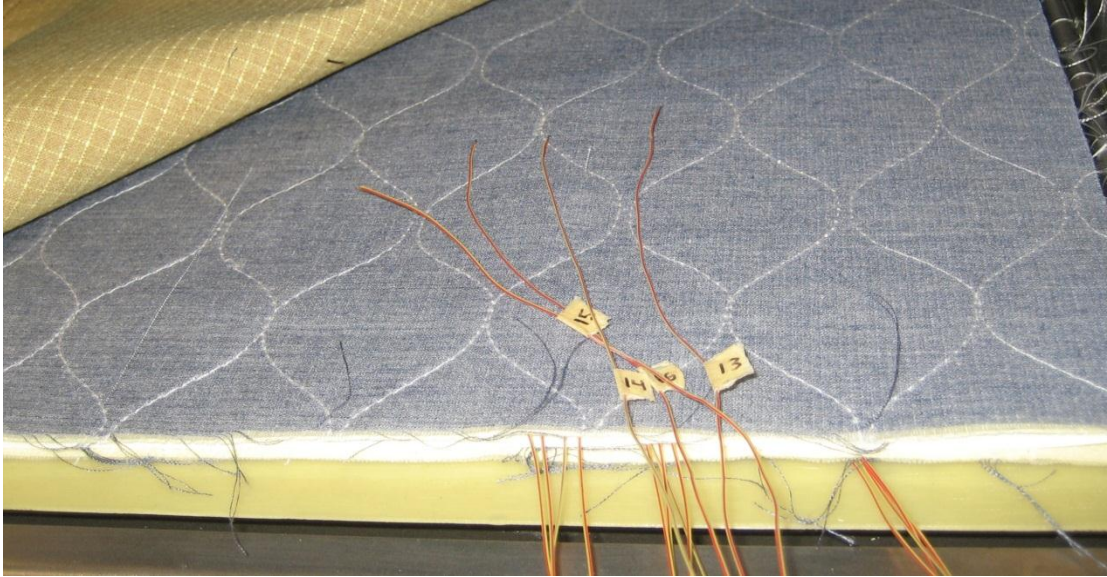
Figure 2.10: Thermocouple positioning between assembly layers prior to placement in square pattern (top) and alternating square pattern describing thermocouple placement (bottom)

Once all thermocouples are positioned, the data acquisition system is allowed to run for approximately five minutes. During this time, temperature measurements are monitored to ensure accurate temperature values are reported and to confirm that all temperature measurements adequately equilibrate with ambient conditions. Note that during this time, the data acquisition system is set to visualize but not record measured data.

After thermal equilibrium is established, the temperature controller is set to the appropriate temperature setting determined by the test series being conducted, the data visualization program is restarted, and data recording is initiated. Immediately after initiation of data recording, the radiant panel is activated. Data is collected for ten minutes, after which data recording is stopped, the radiant panel is powered down, the thermocouples are removed from the assembly, the assembly is removed from the test apparatus, and a small fan is positioned next to the radiant panel to hasten the cooling of the equipment. A standby time of one hour is allotted before the start of subsequent tests to allow the test apparatus to return to ambient temperature.

For moisture series tests, which incorporate the use of the fluid supply system, several additional procedures are followed. Prior to the initiation of each moisture series test, the fluid supply system is purged of any air bubbles and the system is primed. While the system is being primed, fluid flows freely from the pores on the baseplate surface, therefore it is necessary to prime the system before positioning the sample assembly on the baseplate.

Priming of the fluid supply system is conducted as follows. The check valve at the base of the fluid reservoir is opened and the top of the fluid level indicator is plugged shut. The priming pump is then manually actuated until air bubbles appear from the bottom of the stainless-steel tube in the fluid reservoir. While watching the fluid level indicator, the stainless-steel tube is slowly elevated until the level of fluid in the fluid level indicator sits slightly higher than the baseplate surface. The baseplate is then wiped clean to remove excess fluid, the check valve at the base of the fluid reservoir is closed, and the fluid level in the fluid reservoir is recorded.

Once these procedures are completed, the fluid supply system is ready for test initiation. For moisture series tests, the fluid supply system is activated five minutes prior to the activation of the radiant panel. This delay allows adequate time for moisture from the baseplate surface to permeate into the layers of the assembly, simulating conditions in which a firefighter enters an elevated temperature environment after perspiration is allowed to accumulate in the underclothing beneath the protective clothing.

After the five-minute presoaking delay has elapsed, test initiation procedures follow those defined previously for dry tests not involving the use of the fluid supply system. These include the simultaneous initiation of data recording and activation of the radiant panel. In order to maintain consistency with the time conventions used for dry tests, test duration is measured from the initiation of data recording. Once the ten-minute test duration has elapsed, the fluid supply system is deactivated and test completion procedures defined previously for dry tests are subsequently followed. Once other procedures have been completed, the final fluid level in the fluid reservoir is recorded and the baseplate surface is wiped clean to remove excess fluid. An additional amount of standby time is required after moisture series tests to allow assemblies to dry thoroughly before initiation of subsequent tests.

The data collected during testing include recorded temperature measurements and, for moisture series tests, the change in fluid level in the fluid reservoir. Thermocouple measurements are recorded in *.lvm* file format, which are easily imported and analyzed via a spreadsheet or data analysis program such as Microsoft Excel® or MATLAB®.

2.4: Data Analysis and Performance Criteria

For moisture series tests, initial data analysis includes calculation of the fluid flow rate. Because the cross sectional area of the fluid reservoir is known, the change in reservoir fluid level during a test provides a measure of the fluid volume delivered to the assembly. When combined with test duration and the surface area of the baseplate, this provides a measure of the average mass flux of fluid flowing into the assembly. This mass flux of fluid is calculated using the following expression.

$$\dot{m}''_{fl} = \frac{\rho_{fl}\Delta z_{fl}\left(A_{rv} - N_{cy}A_{cy}\right)}{\Delta t\, A_{bp}} \tag{2.1}$$

Further data analysis includes averaging the measurements recorded by the four thermocouples positioned between each assembly layer. This yields a single, temporally variable temperature measurement for each layer. Together, these average measurements provide a time evolution of the average temperature of each layer over the duration of a test. Though these measurements provide useful data, they cannot be compared directly to evaluate relative assembly performance.

As referenced previously, specific analysis is required to distinguish the differences in assembly performance caused by thermal insult variability from those caused by assembly alterations. This analysis is achieved through the calculation of normalized parameters that standardize the measured data with respect to the thermal exposure. A pair of parameters is calculated, including a normalized temperature-rise (NTR) parameter and a normalized temperature-gradient (NTG) parameter. These parameters respectively standardize the data by the total temperature-rise of the outer surface of an assembly and the total temperature-drop occurring across an assembly.

Both the total temperature-rise of the outer surface of an assembly and the total temperature-drop occurring across an assembly are direct measurements of thermal exposure. Because NTR and NTG parameters are respectively standardized by these measurements, they are effectively independent of thermal exposure. As a result, NTR parameters and NTG parameters for a particular assembly can be compared with the associated parameters of other assemblies to evaluate accurately the relative protective performance of each assembly.

Normalized temperature-rise parameters are calculated via the following expression.

$$NTR_j^n = \frac{T_j^n - T_j^0}{T_{os}^n - T_{os}^0} \tag{2.2}$$

In this expression, NTR_j^n gives the normalized temperature-rise parameter of assembly layer j at a discrete time n, T_j^n is the temperature of layer j at time n, T_j^0 is the temperature of layer j at test initiation, T_{os}^n is the temperature of the outermost layer at time n, and T_{os}^0 is the temperature of the outermost layer at test initiation.

NTR parameters define the temperature-rise of an assembly layer of interest, normalized by the temperature-rise of the outer surface of the assembly. Calculated NTR parameters lie between zero and unity, and represent the fraction of the outer surface temperature-rise that occurs at the layer of interest. An NTR parameter of 0.5 indicates that the temperature-rise at the layer of interest is 50% of the outer surface temperature-rise. For this NTR parameter and assuming an outer surface temperature-rise of $100°C$, the temperature-rise in the layer of interest is $50°C$.

NTR parameters for the outermost layer of an assembly remain constant at unity, whereas those for interior layers increase through the duration of a test as the temperatures in these layers converge to the temperature of the outermost layer. Because the thermal exposure produced by the radiant panel fluctuates once the set temperature is reached, consequent fluctuations occur in the temperature of the outermost layer and in *NTR* parameters for interior layers. These *NTR* parameter fluctuations are small because the temperatures of interior layers fluctuate accordantly with those of the outermost layer, but with slightly reduced amplitude.

Instantaneous *NTR* parameters among interior layers progressively decrease from outermost layer to baseplate because the temperatures in these layers progressively reduce as they become more protected from the thermal exposure. Minimum *NTR* parameters are observed at the baseplate, which is the most protected from the thermal exposure and observes the smallest relative temperature-rise.

Baseplate *NTR* parameters are representative of the overall performance of an assembly because they integrate the protective performance provided by all constituent assembly layers. Among comparable assemblies, minimum *NTR* parameters are observed for the assembly offering the greatest protective performance because such an assembly provides the lowest fractional temperature-rise at the assembly interior. *NTR* parameters are of interest because they facilitate the comparison of overall assembly performance, allowing different assemblies to be rated with respect to which provide the greatest protection. Additionally, variations in the materials and orientations of individual layers can be evaluated as to how such changes affect overall assembly performance.

Normalized temperature-gradient parameters are calculated via the following expression.

$$NTG_j^n = \frac{T_j^n - T_{j-1}^n}{T_{os}^n - T_{bp}^n} \qquad (2.3)$$

In this expression, NTG_j^n gives the normalized temperature-gradient parameter across assembly layer j at a discrete time n, T_j^n is the temperature of layer j at time n, T_{j-1}^n is the temperature of the layer directly beneath layer j at time n, T_{os}^n is the temperature of the outermost layer at time n, and T_{bp}^n is the temperature of the baseplate at time n.

NTG parameters define the instantaneous temperature-drop across an individual layer of interest, normalized by the total temperature-drop across the entire assembly at the same instant. As with NTR parameters, NTG parameters lie between zero and unity. NTG parameters represent the fraction of the total temperature-drop across an assembly that is provided by the layer of interest. An NTG parameter of 0.5 indicates that the temperature-drop across the layer of interest provides 50% of the total temperature-drop across the assembly. For this NTG parameter and assuming a $100°C$ drop in temperature across the assembly, the temperature-drop provided by the layer of interest is $50°C$.

At any instant, the summation of the individual temperature-drops across the layers within an assembly must equal the total temperature-drop across the assembly. As a result, the summation of instantaneous NTG parameters among the layers of an assembly must always equal unity. NTG parameters within an assembly vary

throughout the duration of a test as the temperature gradients across individual layers adapt to reach a steady-state condition. Because outer layers increase in temperature more quickly than inner layers, NTG parameters for outer layers are initially large and decrease until a steady-state condition is reached, whereas those for inner layers are initially small and increase until a steady-state condition is reached.

In a steady-state domain, the flux of thermal energy through an assembly is constant and the temperature-drops across constituent layers become representative of the thermal resistance of each layer. Because the relative NTG parameters among layers in an assembly depend on the respective temperature-drops across each layer, those NTG parameters at steady-state also represent the thermal resistance of each layer. Among assembly layers, maximum NTG parameters are observed for the layer offering the greatest protective performance because such a layer provides the greatest fractional temperature-drop across the assembly.

NTG parameters are of interest because they isolate the performance of individual assembly layers, allowing different layers to be rated with respect to which provide the greatest thermal resistance. Additionally, variations in the materials and orientations of each layer can be evaluated as to how such changes directly affect the individual performances of the modified layers.

In comparing assembly performance, time evolutions of NTR and NTG parameters are plotted for the constituent layers of each assembly, providing a visualization of individual layer performances. In reviewing these plots, it is important to note that it is possible for NTR and NTG parameters to yield nonphysical values if certain conditions exist. A negative value is obtained if the temperature of a

layer decreases below its initial value or if the temperature at an inner layer exceeds that at an outer layer. An infinite result is obtained if either the temperature-rise of the outermost layer or the temperature-drop across the assembly approach zero. These conditions occur easily at the initiation of each test, at which time the temperatures of all layers are approximately equal and uniform at ambient temperature. To alleviate this issue, NTR and NTG parameters are plotted only after the $100\ s$ mark of each test. This initial time allows for the establishment of an adequate temperature gradient across the assembly and prevents the occurrence of nonphysical parameter values.

In addition to plotted visualizations, assemblies are compared based on a pair of quantifiable performance criteria evaluating assembly performance in both a transient and steady-state domain. A performance criterion based on NTR parameters is utilized to evaluate the overall transient performance of each assembly, and a performance criterion based on NTG parameters is utilized to evaluate the individual steady-state performance of layers of interest.

The NTR criterion is calculated by averaging the instantaneous rate of change of baseplate NTR parameters between the $100\ s$ and $300\ s$ mark of each test. This time duration is chosen because it captures a well-defined transient domain for the majority of the conducted tests. The NTR criterion has units of inverse time and represents the fractional rate of change of the temperature at the inner surface of an assembly relative to that at the outer surface of the assembly. An NTR criterion of $0.05\ min^{-1}$ indicates that the temperature at the inner surface of an assembly is increasing at a rate of 5% per minute relative to the temperature at the outer surface of the assembly. For this NTR criterion and assuming a constant outer surface

temperature of $100°C$, the rate of temperature-rise at the inner surface of the assembly is $5°C$ per minute.

Effectively, the NTR criterion characterizes the rate at which the temperatures at the inner and outer surfaces of an assembly converge. For intense thermal exposures, a reduction in this convergence rate indicates an increase in the length of time available before untenable thermal conditions develop at the inner surface of the assembly. As a result, assemblies measuring smaller values of the NTR criterion are considered to provide improved protective performance.

The NTG criterion is calculated by averaging NTG parameters characteristic of a layer of interest over the final 200 seconds of each test. This time duration is chosen because it captures a well-defined steady-state domain for the majority of the conducted tests. The NTG criterion is dimensionless and represents the fractional temperature-drop across a layer of interest, relative to the total temperature-drop across the entire assembly. NTG criteria are equivalent to NTG parameters with the exception that NTG criteria characterize the average steady-state performance of assembly layers, whereas NTG parameters characterize the instantaneous performance of assembly layers.

As previously noted, in a steady-state domain, the relative fractional temperature-drops of the constituent layers in an assembly represent the respective thermal resistances provided by each layer. An increase in the steady-state temperature-drop across an assembly layer indicates an increase in thermal resistance and, as a result, layers measuring larger values of the NTG criterion are considered to provide improved protective performance.

It is worth noting that the previously described performance criteria bear no resemblance to the earlier referenced performance criteria described in *NFPA 1971*. This may initially be perceptible as an apparent disconnect between this analysis and the performance measures of the *NFPA*; however, it is important to note that the fundamental goal of this analysis is the direct comparison of the performances of a finite set of garment assemblies as tested within this analysis. This goal is simply accomplished by utilizing a consistent set of testing conditions and performance criteria within the domain of the analysis being conducted. It is not necessary for this analysis to replicate the testing conditions and performance criteria stipulated by the *NFPA* because this analysis does not attempt to extend the performance comparisons developed within to include assemblies not explicitly tested under the developed performance criteria.

It should also be noted that the previously introduced *TPP* criterion referenced in *NFPA 1971* provides only for the comparison of overall assembly performances, whereas the combination of *NTR* and *NTG* criteria developed in this analysis provide for the comparison of overall assembly performance and individual layer performance. In addition, *NTR* and *NTG* criteria are normalized with respect to thermal exposure conditions and thus provide predictability of garment performance for varying thermal exposures. The *TPP* criterion, however, is evaluated for a specific thermal exposure condition and provides no predictability of garment performance for alternative thermal exposures. The performance criteria developed in this analysis thus provide significantly more information conducive to a more effective comparison of garment performances than do the criteria utilized by the *NFPA*.

2.5: Uncertainty Analysis

The uncertainties associated with the average temperature measurements are calculated via the following expression, which estimates the standard deviation of the mean characterizing a sample of discrete values [22].

$$S_{\bar{T}} = \sqrt{\frac{1}{N(N-1)} \sum_{j=1}^{N} \left(T_j - \bar{T}\right)^2} \qquad (2.4)$$

In this expression, $S_{\bar{T}}$ gives the standard deviation of the average temperature among a set of temperature measurements, N is the number of measurements in the set, T_j is the value of a particular temperature measurement, and $\bar{T}$ is the average of the measurements in the set.

Two forms of uncertainty are considered in this analysis. The first includes the standard deviation among the individual temperature measurements of the four thermocouples positioned across an assembly layer. This standard deviation characterizes the uncertainty associated with the spatial distribution of temperature across the surface of a layer. The second form of uncertainty includes the standard deviation among the average temperature measurements of a particular layer across a collection of multiple tests for a single assembly. This standard deviation characterizes the uncertainty associated with the reproducibility of measurements across multiple tests and the underlying precision of the experimental method.

Each of these standard deviations is calculated for a set of temperature measurements from a representative assembly. The results of these calculations are plotted with respect to test duration and are provided in **Figure 2.11** and **Figure 2.12**.
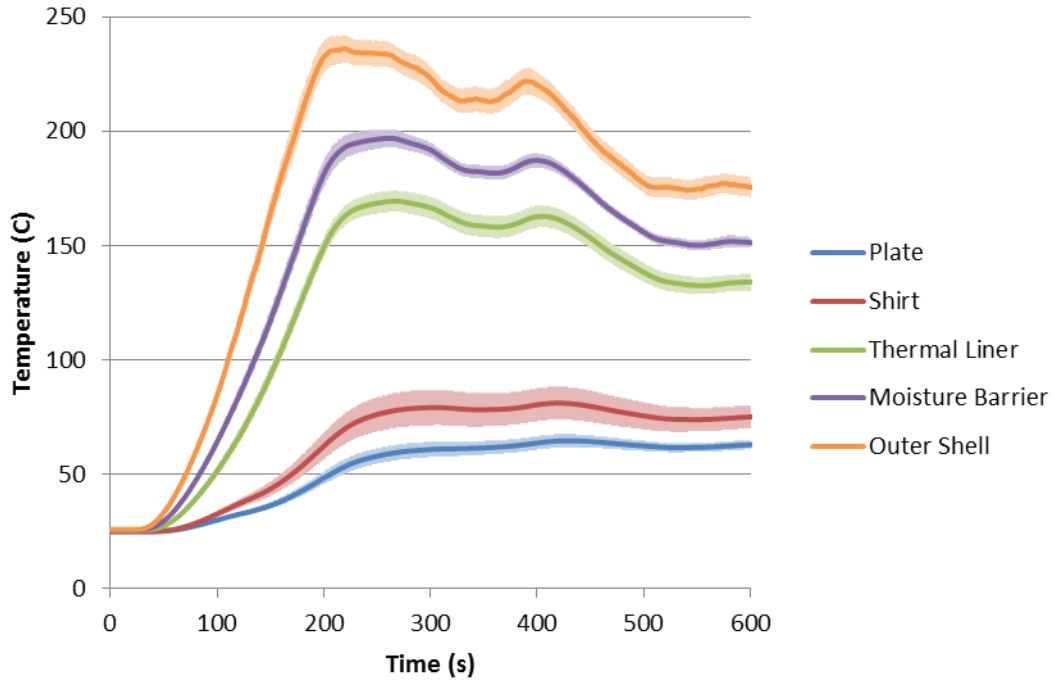
Figure 2.11: Standard deviations among individual temperature measurements within each assembly layer for a single test iteration
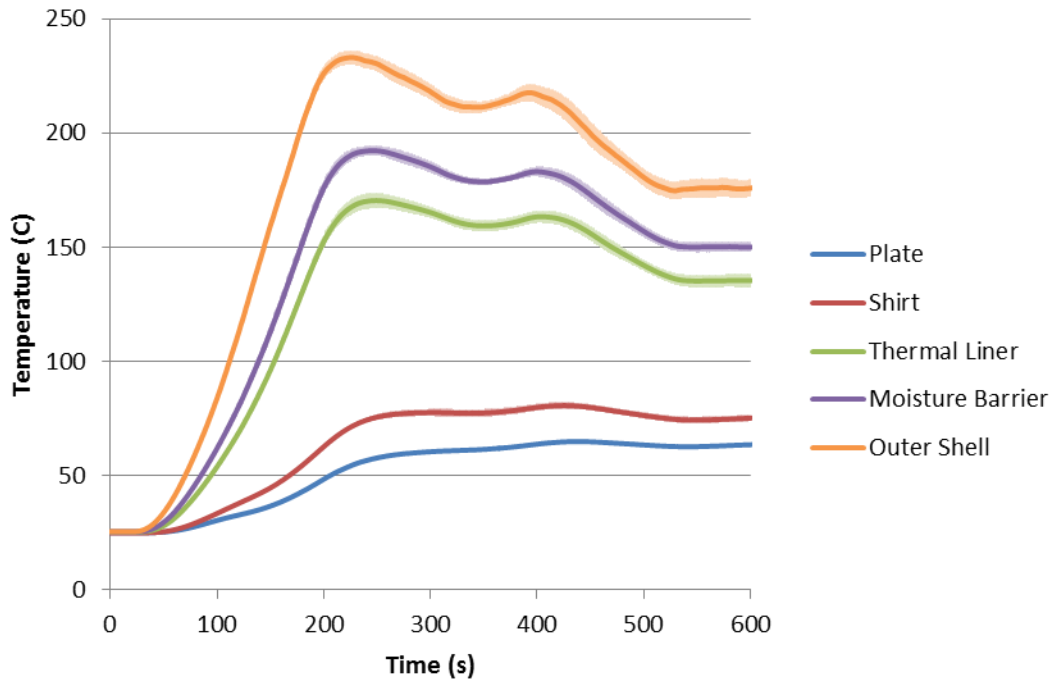
Figure 2.12: Standard deviations among average temperature measurements for each assembly layer across multiple test iterations

70

Figure 2.11 provides the time evolution of average layer temperatures among the layers of a representative assembly for a single test. In this figure, standard deviation values for each layer are calculated among the set of four temperatures measured within each layer. **Figure 2.12** provides the time evolution of average layer temperatures among the layers of the same assembly averaged across a collection of four tests. In this figure, standard deviation values for each layer are calculated among the set of four average layer temperatures across the collection of tests. As shown in these figures, the standard deviations among individual temperature measurements for a single test are significantly greater than those among average layer temperatures across multiple tests. Among individual temperature measurements, standard deviation values reach approximate maxima of $7°C$ to $8°C$, whereas among average layer temperatures, standard deviation values reach approximate maxima of $4°C$ to $5°C$.

The disparity between the two uncertainties suggests that, despite the large variation among individual temperature measurements across a particular layer, the average temperature of a particular layer remains consistent across multiple tests. This is explained by the realization that the variation among individual temperature measurements is the result of a non-uniform temperature distribution across the layer surface. That the variation among average layer temperatures is small suggests that this non-uniform temperature distribution is relatively constant across multiple tests.

The underlying goal of the test method is to establish meaningful comparisons evaluating the relative performance of different assemblies. Factors that remain constant across all tests are of little interest because they affect equally all test results

and do not influence the relative results of one test as compared to another. In assuming that the non-uniform spatial distribution of temperature across assembly layers is constant, the uncertainty associated with individual thermocouple measurements within a particular assembly layer becomes inconsequential.

The uncertainties of interest in this analysis are those associated with the variation of average temperature measurements for each assembly layer across multiple test iterations. These uncertainties characterize the reproducibility of the test results and have a far greater impact on the reliability of the performance comparisons than do the uncertainties associated with individual thermocouple measurements. As such, the standard deviation calculations that are conducted for all reported results and that appear on all data figures are those associated with the average layer temperatures among sets of multiple tests.

In extending the uncertainty analysis to NTR and NTG parameters, the following expressions are used to calculate the associated standard deviations of each parameter. A detailed derivation of these expressions is provided in *Appendix E*.

$$S_{NTR_j^n}$$

$$= \sqrt{\frac{S_{T_j^n}^2}{(T_{os}^n - T_{os}^0)^2} + \frac{S_{T_j^0}^2}{(T_{os}^n - T_{os}^0)^2} + S_{T_{os}^n}^2 \frac{\left(T_j^n - T_j^0\right)^2}{(T_{os}^n - T_{os}^0)^4} + S_{T_{os}^0}^2 \frac{\left(T_j^n - T_j^0\right)^2}{(T_{os}^n - T_{os}^0)^4}} \quad (2.5)$$

$$S_{NTG_j^n}$$

$$= \sqrt{\frac{S_{T_j^n}^2}{\left(T_{os}^n - T_{bp}^n\right)^2} + \frac{S_{T_{j-1}^n}^2}{\left(T_{os}^n - T_{bp}^n\right)^2} + S_{T_{os}^n}^2 \frac{\left(T_j^n - T_{j-1}^n\right)^2}{\left(T_{os}^n - T_{bp}^n\right)^4} + S_{T_{bp}^n}^2 \frac{\left(T_j^n - T_{j-1}^n\right)^2}{\left(T_{os}^n - T_{bp}^n\right)^4}} \quad (2.6)$$

Chapter 3 : Results and Discussion

Plotted temperatures, NTR parameters, and NTG parameters for all constituent layers of individual assemblies are provided respectively in *Appendix 0*, *Appendix G*, and *Appendix H*. Measurements for selected assembly layers characterizing the performance of each assembly and accompanying discussions of performance comparisons within each test series are presented as follows.
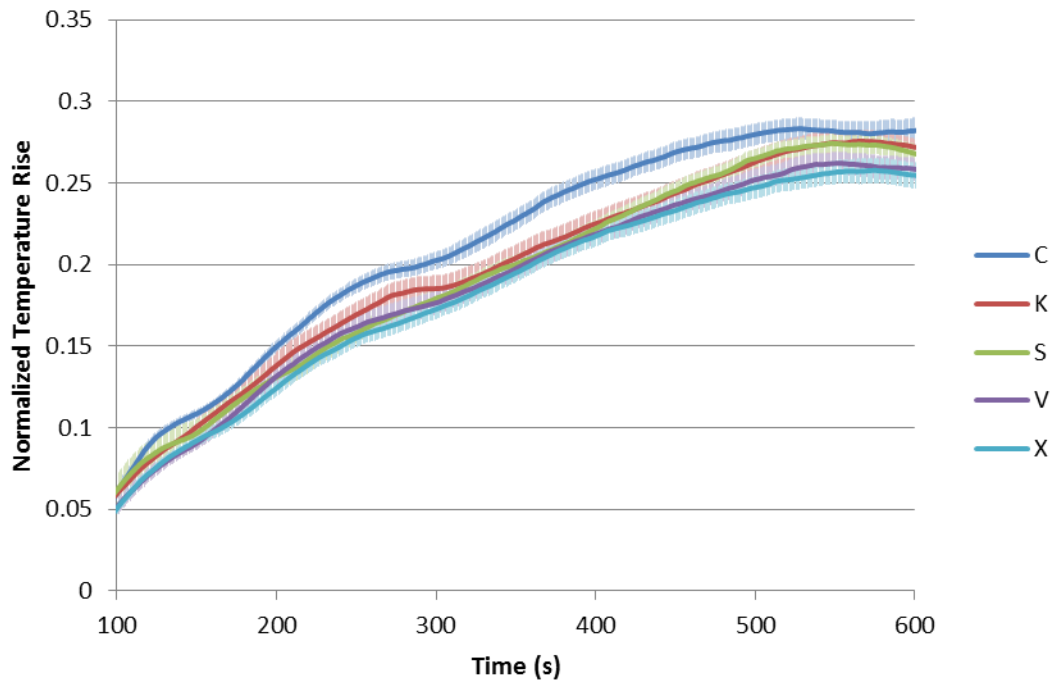
3.1: Lion Series

Lion series assemblies consist of market-available firefighter protective clothing models as received from Lion Apparel. These assemblies consist of several different combinations of outer shell, moisture barrier, and thermal liner variants. The two outer shell variants, two moisture barrier variants, and five thermal liner variants yield twenty distinct assemblies, each incorporating a unique combination of constituent layers. Notably, lion series assemblies do not include a shirt layer. All lion series tests are conducted with dry conditions and do not incorporate the use of the fluid supply system. Additionally, lion series tests utilize a radiant panel temperature setting of $150°C$.

This series serves to evaluate the relative performance of the materials offered by Lion Apparel within their market-available clothing models. Variations in these materials are then analyzed to assess which materials and combinations of materials are most effective. Because the properties of these materials are known, their expected relative performance is also known. As a result, this series serves as a calibration of the test method to ensure that measured results match expectations.

The twenty assemblies utilized in this series are designated according to the nomenclature format L-$\alpha\beta\gamma$, where α, β, and γ respectively give the labels of the thermal liner, outer shell, and moisture barrier present in each assembly. As given by α, the labels C, K, S, V, and X respectively designate inclusion of a *C-Liner*, *K-Liner*, *Semper-Dri*, *V-Caldura*, or *X-Liner* thermal liner within the assembly. Similarly, as given by β, the labels F and P respectively designate inclusion of a *Fusion* or *PBI Matrix* outer shell and, as given by γ, the labels T and R respectively designate inclusion of a *Crosstech* or *RT-7100* moisture barrier. For example, the assembly designation L-*CPT* represents an assembly containing a *C-Liner* thermal liner, *PBI Matrix* outer shell, and *Crosstech* moisture barrier.

In presenting the results of lion series tests, measurements among all assemblies containing a particular material of interest are averaged. Results are then reported in terms of the average performance among assemblies containing that material. This averaging process greatly simplifies the comparison of measurements among different materials. For example, in comparing relative performance between *PBI Matrix* and *Fusion* outer shells, each assembly containing a *PBI Matrix* outer shell is not individually compared against each assembly containing a *Fusion* outer shell. Rather, the average performance of all assemblies containing a *PBI Matrix* outer shell is compared against the average performance of all assemblies containing a *Fusion* outer shell. The performance of each outer shell and moisture barrier is thus reported as the average of ten individual assembly performances, whereas the performance of each thermal liner is reported as the average of four individual assembly performances.

74

The time evolutions of baseplate NTR parameters for assemblies containing differing thermal liners, outer shells, and moisture barriers are provided respectively in **Figure 3.1**, **Figure 3.2**, and **Figure 3.3**. As shown in **Figure 3.1**, there are slight variations in NTR parameters between thermal liners, though some of these variations are within the uncertainty of the measurements. NTR parameters are lowest for assemblies containing an X thermal liner and progressively increase for assemblies containing V, S, K, and C thermal liners. As shown in **Figure 3.2**, NTR parameters are slightly lower for assemblies containing a P outer shell as compared to an F outer shell; however, these variations are negligible and within the uncertainty of the measurements. As shown in **Figure 3.3**, NTR parameters are noticeably reduced for assemblies containing an R moisture barrier as compared to a T moisture barrier, indicating that the R moisture barrier provides improved protective performance.

Figure 3.1: Time evolution of baseplate NTR parameters among lion series assemblies with varying thermal liners
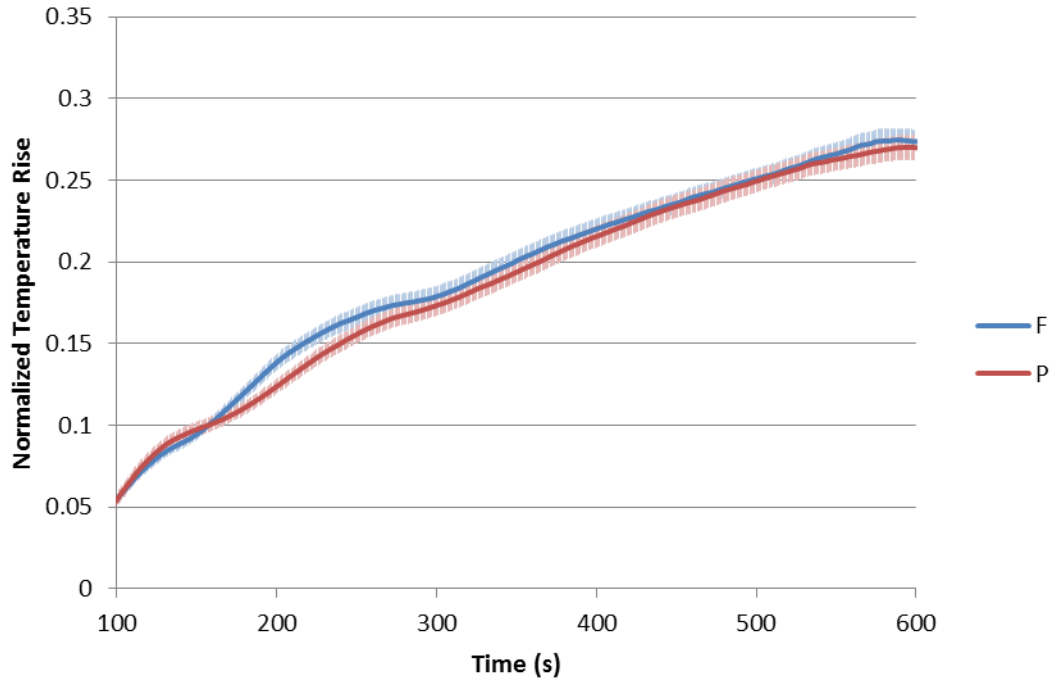
Figure 3.2: Time evolution of baseplate *NTR* parameters among lion series assemblies with varying outer shells
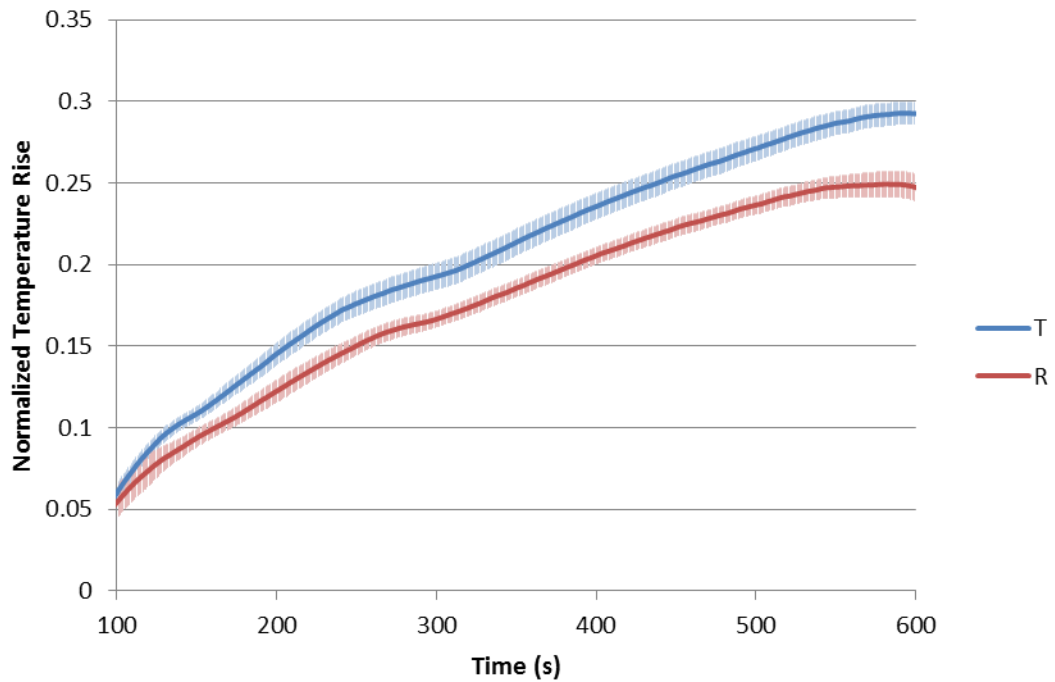
Figure 3.3: Time evolution of baseplate *NTR* parameters among lion series assemblies with varying moisture barriers

Though the NTR parameter trends among outer shells and some thermal liners are insignificant, the trends for all three material classifications closely follow the respective inverse trends of relative thickness. For the thicknesses of the constituent materials in each assembly, refer to the previously provided data in **Table 2.1**. Among thermal liners, X thermal liners are thickest with V, S, K, and C thermal liners having gradually reduced thickness. Similarly, P outer shells are slightly thicker than F outer shells, and R moisture barriers are significantly thicker than T moisture barriers. These trends indicate a coupled relationship between NTR parameters and relative thickness, suggesting that materials with increasing thickness provide a reduction in NTR parameter. This behavior is expected because with increasing thickness, the rate of heat transfer through a material is reduced.

NTR criteria for assemblies containing differing thermal liner, outer shell, and moisture barrier variants are provided respectively in **Table 3.1**, **Table 3.2**, and **Table 3.3**. As shown in **Table 3.1**, NTR criteria for assemblies containing a C, K, S, V, or X thermal liner are respectively 0.035, 0.033, 0.033, 0.032, and 0.032. Compared to a C thermal liner, K and S thermal liners measure a 5.7% reduction in NTR criterion, and V and X thermal liners measure an 8.6% reduction in NTR criterion.

As shown in **Table 3.2**, the NTR criterion for assemblies containing either an F or P outer shell is 0.033, indicating that there is no measureable difference in NTR criterion between the two outer shells. As shown in **Table 3.3**, NTR criteria for assemblies containing a T or R moisture barrier are respectively 0.034 and 0.032. Based on these values, an R moisture barrier measures a 5.9% reduction in NTR criterion as compared to a T moisture barrier.

Table 3.1: NTR criteria among lion series assemblies with varying thermal liners

Thermal Liner	Thickness (mm)	NTR Criterion (min^{-1})	Improvement
C	1.016	0.035	–
K	1.473	0.033	5.7%
S	1.499	0.033	5.7%
V	1.575	0.032	8.6%
X	1.600	0.032	8.6%

Table 3.2: NTR criteria among lion series assemblies with varying outer shells

Outer Shell	Thickness (mm)	NTR Criterion (min^{-1})	Improvement
F	0.381	0.033	–
P	0.406	0.033	0.0%

Table 3.3: NTR criteria among lion series assemblies with varying moisture barriers

Moisture Barrier	Thickness (mm)	NTR Criterion (min^{-1})	Improvement
T	0.381	0.034	–
R	0.762	0.032	5.9%

As shown by these criteria, there is a measureable increase in protective performance provided by assemblies incorporating thicker materials. This is evidenced by the reduction in NTR criterion characteristic of assemblies utilizing materials with increasing thickness. Additionally, the performance improvements provided by increasing thickness correlate directly with the magnitude of the increase in thickness. This indicates that greater increases in thickness produce greater resultant improvements to protective performance. These results agree with expected trends and support the accuracy of the measurements.
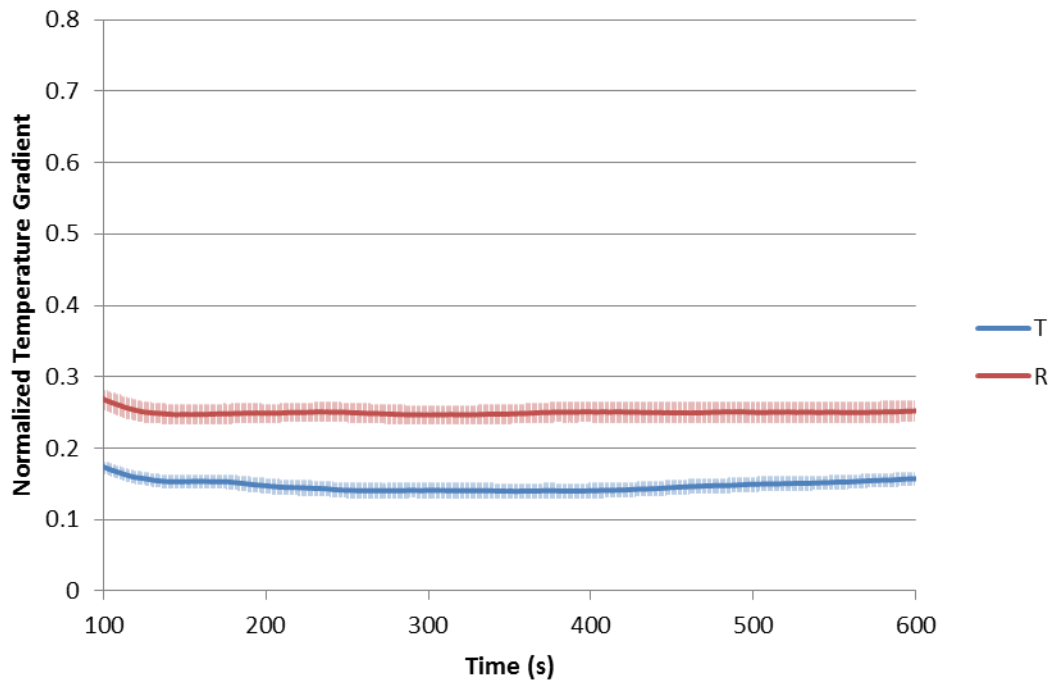
The time evolutions of NTG parameters for assemblies containing differing thermal liners, outer shells, and moisture barriers are provided respectively in **Figure 3.4**, **Figure 3.5**, and **Figure 3.6**. In each of these figures, reported NTG parameters are respectively characteristic of the thermal liner, outer shell, or moisture barrier layer within each assembly. As shown in **Figure 3.4**, NTG parameters are greatest for X thermal liners and progressively decrease for V, S, K, and C thermal liners; however, as with the NTR parameters, some of these variations are within the uncertainty of the measurements. Similarly, as shown in **Figure 3.5**, variations in NTG parameters between assemblies containing F or P outer shells are also nearly negligible and within the uncertainty of the measurements. As shown in **Figure 3.6**, NTG parameters are noticeably greater for assemblies containing an R moisture barrier as compared to a T moisture barrier.
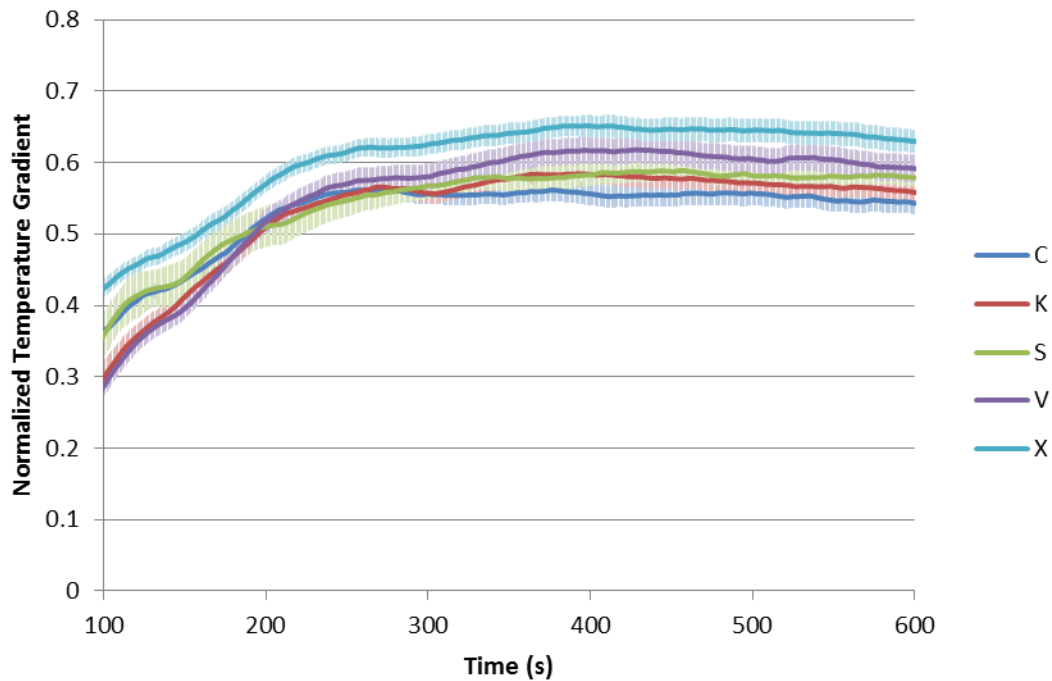
Figure 3.4: Time evolution of NTG parameters across the thermal liner layer among lion series assemblies with varying thermal liners
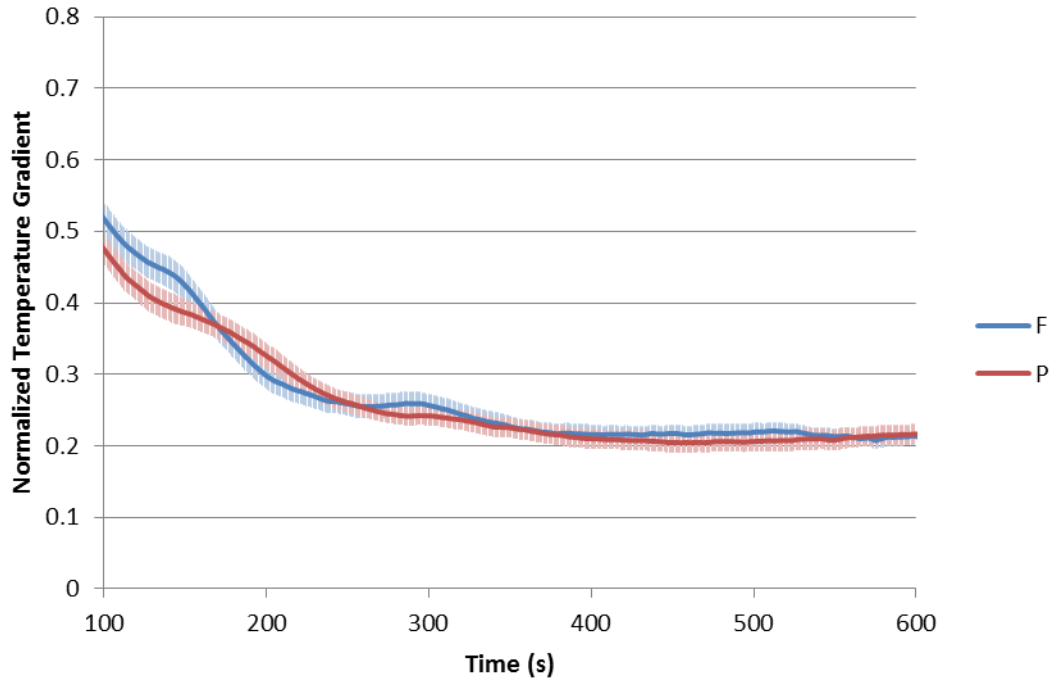
Figure 3.5: Time evolution of NTG parameters across the outer shell layer among lion series assemblies with varying outer shells

Figure 3.6: Time evolution of NTG parameters across the moisture barrier layer among lion series assemblies with varying moisture barriers

80

As with the NTR parameter trends, the NTG parameter trends for all three material classifications closely follow the respective trends of relative thickness. This suggests that NTG parameters also bear a coupled relationship with relative thickness and that materials with increasing thickness provide an increase in NTG parameter. Because increasing the thickness of a material forces a resultant increase in the steady-state temperature-drop across the material, the observed increases in NTG parameter are expected. These results provide additional support for the accuracy of the measurements and further evidence of the increased protective performance provided by assemblies incorporating thicker materials.

NTG criteria for assemblies containing differing thermal liner, outer shell, and moisture barrier variants are provided respectively in **Table 3.4**, **Table 3.5**, and **Table 3.6**. As shown in **Table 3.4**, NTG criteria of the thermal liner layer within assemblies containing a C, K, S, V, or X thermal liner are respectively 0.545, 0.561, 0.580, 0.595, and 0.634. Based on these values, K thermal liners measure a 2.9% increase in NTG criterion as compared to C thermal liners. Similarly, S, V, and X thermal liners measure respective increases of 6.4%, 9.2%, and 16.3% as compared to C thermal liners.

As shown in **Table 3.5**, NTG criteria of the outer shell layer within assemblies containing an F or P outer shell are respectively 0.213 and 0.215, where P outer shells measure a 0.9% increase as compared to F outer shells. Similarly, as shown in **Table 3.6**, NTG criteria of the moisture barrier layer within assemblies containing a T or R moisture barrier are respectively 0.155 and 0.251, where R moisture barriers measure a 61.9% increase as compared to T moisture barriers.

Table 3.4: NTG criteria of the thermal liner layer among lion series assemblies with varying thermal liners

Thermal Liner	Thickness (mm)	NTG Criterion	Improvement
C	1.016	0.545	–
K	1.473	0.561	2.9%
S	1.499	0.580	6.4%
V	1.575	0.595	9.2%
X	1.600	0.634	16.3%

Table 3.5: NTG criteria of the outer shell layer among lion series assemblies with varying outer shells

Outer Shell	Thickness (mm)	NTG Criterion	Improvement
F	0.381	0.213	–
P	0.406	0.215	0.9%

Table 3.6: NTG criteria of the moisture barrier layer among lion series assemblies with varying moisture barriers

Moisture Barrier	Thickness (mm)	NTG Criterion	Improvement
T	0.381	0.155	–
R	0.762	0.251	61.9%

As with the NTR criteria, these NTG criteria indicate that thicker assembly layers provide a measurable improvement to thermal resistance. This is evidenced by the increase in NTG criterion characteristic of layers with increasing thickness. These improvements correlate with the magnitude of the increase in thickness and are significant for large increases in thickness, but are insignificant for small increases in thickness. These results agree with expected trends and provide additional support for the accuracy of the measurements.

It is interesting to note the variations in NTG criterion between different materials. For all materials, NTG criteria among the thermal liners are significantly higher than NTG criteria among the outer shells and moisture barriers. This indicates that the total temperature-drop occurring across a given assembly is contained primarily within the thermal liner and suggests that the thermal liner is the premier protective layer within an assembly with respect to thermal resistance. This is expected because the thermal liner is the thickest layer within the tested assemblies.

Comparably, NTG criteria among the outer shells and moisture barriers are approximately equal. The outer shells and moisture barriers each provide some resistance to heat transfer, though significantly less than that provided by the thermal liners. This is also expected because the average thicknesses of the outer shells and moisture barriers are significantly less than those of the thermal liners. Though the outer shells and moisture barriers provide reduced resistance to heat transfer, they remain integral parts of effective firefighter protective clothing and it is important to note that heat transfer resistance is not their primary purpose.

From the observed trends, it is readily apparent that the thickness of individual layers is a primary factor affecting the protective performance of firefighter protective clothing. Irrespective of other thermal properties, increasing the thickness of the constituent layers of an assembly is shown to produce noticeable improvements to thermal protection for both transient and steady-state conditions. These results agree with the expected behavior of the differing materials based on fundamental heat transfer concepts. As a result, the test method is shown to produce justifiable results within an understandable and reasonable degree of uncertainty.

83

Static air-gap series assemblies contain four layers of *Fusion* outer shell material with a variable number of air-gap frames positioned between the second and third layers. Notably these assemblies contain no shirt layer and do not include moisture barriers or thermal liners. Outer shell materials are chosen for their rigidity and unlikeliness to sag between the supports of the air-gap frames. Four distinct assemblies are utilized, each employing a different number of frames to achieve a range of air-gap thicknesses. All static air-gap series tests are conducted with dry conditions and do not incorporate the use of the fluid supply system. Additionally, static air-gap series tests utilize a radiant panel temperature setting of $150°C$.

This series serves to examine the impact of a dedicated air-gap on the protective performance of tested assemblies. An assembly including no frames and hence no air-gap is tested to establish a reference performance to which the assemblies containing air-gaps are compared. Identical assemblies with air-gaps of varying discrete thicknesses are then evaluated to determine the variations in performance associated with increasing air-gap thickness.

The four assemblies utilized in this series include assemblies A-0, A-1, A-2, and A-4. These assemblies respectively incorporate the use of 0, 1, 2, and 4 air-gap frames, creating respective air-gap thicknesses of $0\ mm$, $7\ mm$, $14\ mm$, and $28\ mm$. The layers utilized in these assemblies are progressively labeled from baseplate to radiation shield as *Plate*, *Layer 1*, *Layer 2*, *Air Gap*, *Layer 3*, and *Outer Shell*. Positioning of thermocouples inside the *Air Gap* layer includes two groups of four thermocouples respectively fastened to the top surface of *Layer 2* and the bottom

surface of *Layer 3*. As there is no material layer between these two groups of thermocouples, their relative measurements establish the temperature gradient across the air-gap separating the *Layer 2* and *Layer 3* materials.

The time evolution of baseplate *NTR* parameters for each assembly is provided in **Figure 3.7**. As shown in the figure, *NTR* parameters decrease significantly with the introduction of the single layer air-gap and continue to decrease with increasing air-gap thickness. This indicates that the introduction of the air-gap to the assembly and the continued thickening of that air-gap results in a reduced rate of temperature-rise at the inner surface of the assembly. According to these trends, the assembly offering the greatest protective performance is *A-4*, with *A-2*, *A-1*, and *A-0* offering progressively reduced performance. Also of interest, is the relative improvement in performance occurring with each increase in air-gap thickness.
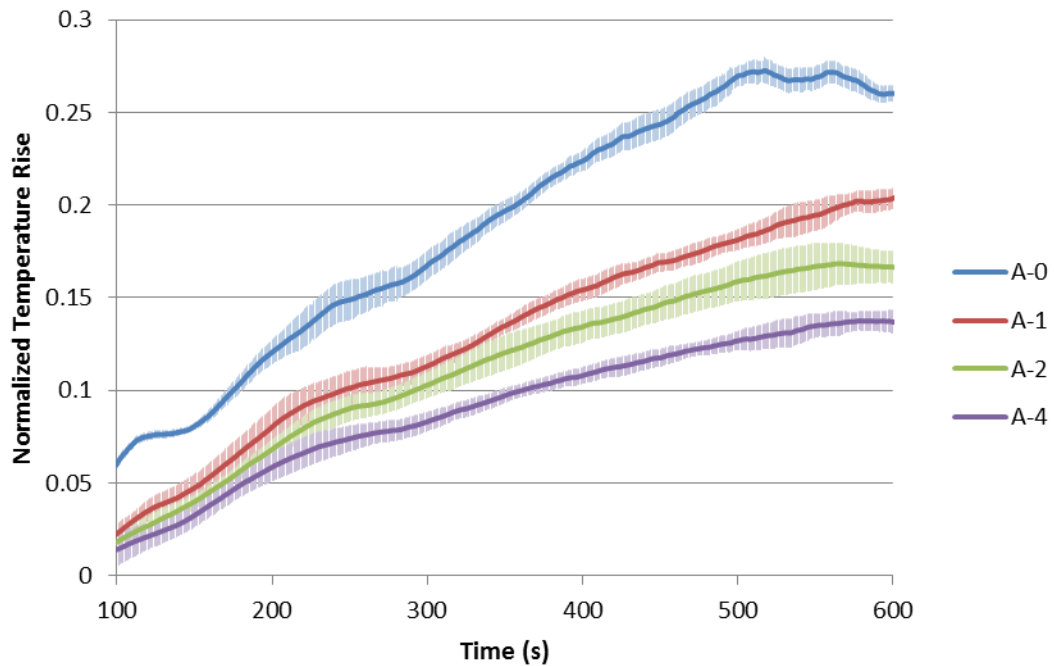
Figure 3.7: Time evolution of baseplate *NTR* parameters among static air-gap series assemblies

The NTR criteria for assemblies A-0, A-1, A-2, and A-4 are respectively 0.032, 0.024, 0.021, and 0.017. Based on these values, assembly A-1 measures a 25.0% reduction in NTR criterion as compared to assembly A-0. Similarly, assembly A-2 measures a 12.5% reduction as compared to assembly A-1 and assembly A-4 measures a 19.0% reduction as compared to assembly A-2. Between assemblies A-0 and A-1 there is a 3.6% reduction in NTR criterion that occurs per $1\ mm$ increase in air-gap thickness. Between assemblies A-1 and A-2, this falls to 1.8% per mm and between assemblies A-2 and A-4, falls again to 1.4% per mm. A summary of these data is provided in **Table 3.7**.

While there is a significant and definitive reduction in NTR criterion that occurs with increasing air-gap thickness, the magnitude of that reduction per-unit-thickness decreases with increasing thickness of the air-gap. In effect, the protective performance per-unit-thickness provided by the air-gap decreases with increasing thickness. Considering cost-effectiveness, this indicates that the ideal implementation of a dedicated air-gap within a garment of firefighter protective clothing is limited to thin air-gaps.

Table 3.7: NTR criteria among static air-gap series assemblies

Assembly	Air-Gap Thickness (mm)	NTR Criterion (min^{-1})	Improvement	Improvement per mm
A-0	$0\ mm$	0.032	–	–
A-1	$7\ mm$	0.024	25.0%	3.6%
A-2	$14\ mm$	0.021	12.5%	1.8%
A-4	$28\ mm$	0.017	19.0%	1.4%

The time evolution of NTG parameters characteristic of the air-gap layer within each assembly is provided in **Figure 3.8**. As shown in the figure, NTG parameters increase significantly with the introduction of the single layer air-gap and continue to increase with rising air-gap thickness. This indicates that the thickening of the air-gap increases the thermal resistance between the two layers separated by the air-gap. According to these trends, the air-gap offering the greatest thermal resistance is the $28\,mm$ air-gap with the $14\,mm$, $7\,mm$, and $0\,mm$ air-gaps offering progressively reduced thermal resistance.
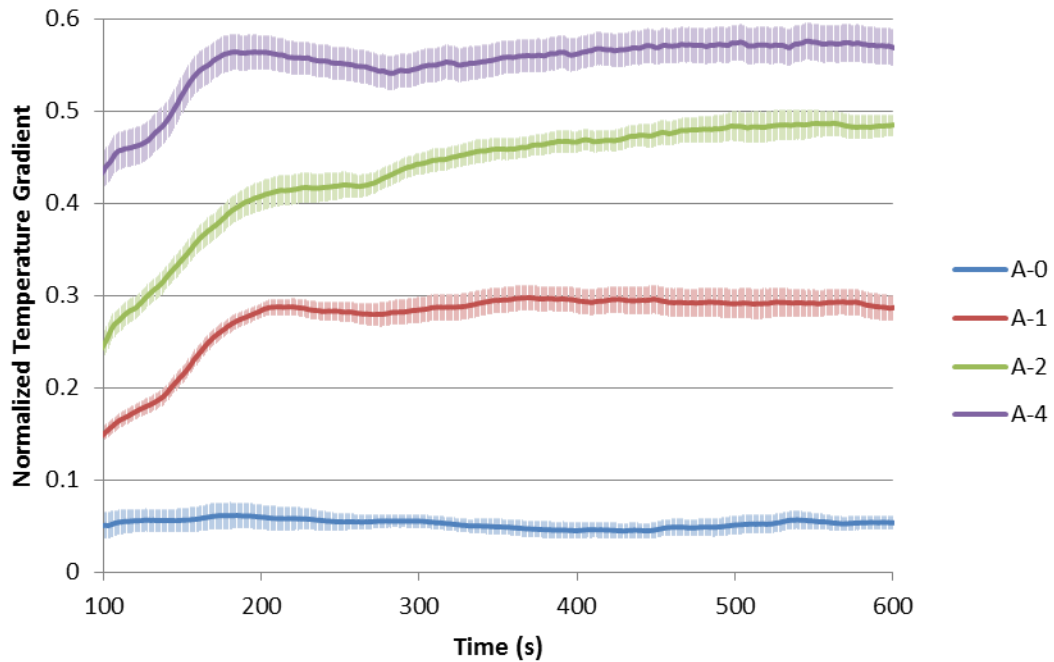
Figure 3.8: Time evolution of NTG parameters across the air-gap layer among static air-gap series assemblies

It is interesting to note that the NTG parameters for the assembly utilizing no air-gap frames measure nonzero values. This indicates that, even without the presence of a dedicated air-gap, there is a small residual air-gap existing between adjacent layers in the assembly. The NTG parameters for this condition are characteristic of

the residual temperature gradient occurring between adjacent layers and provide a measurement of the thermal contact resistance between those layers.

The NTG criteria of the air-gap layer in assemblies A-0, A-1, A-2, and A-4 are respectively 0.050, 0.291, 0.473, and 0.566. Based on these values, assembly A-1 measures a 482.0% increase in NTG criterion as compared to assembly A-0. Similarly, assembly A-2 measures a 62.5% increase over assembly A-1 and assembly A-4 measures a 19.7% increase over assembly A-2. Between assemblies A-0 and A-1 there is a 68.9% increase in NTG criterion that occurs per $1\ mm$ increase in air-gap thickness. Between assemblies A-1 and A-2, this falls to 8.9% per mm and between assemblies A-2 and A-4, falls again to 1.4% per mm. A summary of these data is provided in **Table 3.8**.

As observed with NTR criteria, the influence of increasing air-gap thickness on NTG criteria reduces with increasing thickness. With each incremental increase in thickness, there is a reduced increase in NTG criterion and a reduced increase in the protective performance of the air-gap layer. This trend is further evidence that the cost-effectiveness of a dedicated air-gap reduces with increasing air-gap thickness.

Table 3.8: NTG criteria of the air-gap layer among static air-gap series assemblies

Assembly	Air-Gap Thickness (mm)	NTG Criterion	Improvement	Improvement per mm
A-0	$0\ mm$	0.050	–	–
A-1	$7\ mm$	0.291	482.0%	68.9%
A-2	$14\ mm$	0.473	62.5%	8.9%
A-4	$28\ mm$	0.566	19.7%	1.4%

Based on this analysis, it is apparent that the introduction of a dedicated air-gap to a garment of firefighter protective clothing significantly improves thermal protection. This improvement is the result of a reduction in the rate of heat transfer through the garment and the rate of temperature-rise at the interior of the garment. These effects are observable for both transient and steady-state conditions and yield an overall improvement to the protective performance of the garment.

While the performance of the air-gap improves with increasing thickness, the improvement resulting from incremental thickening of the air-gap reduces with increasing thickness. No optimal air-gap thickness is discovered in this analysis, though this is likely a result of the minimized convective heat transfer occurring with the chosen experimental setup. Due to the horizontal orientation of the air-gap and the application of heat from above, buoyant effects produce a negligible flow directed opposite to the flow of heat. For other configurations including a vertical air-gap, buoyant effects are expected to produce non-negligible flows. For these orientations, such flows likely alter the mechanisms of heat transfer through the air-gap.

Particularly noteworthy is that an air-gap itself comprises no additional material or weight and consists simply of empty space. Additionally, for air-gaps that are relatively small in thickness, large improvements in performance can be gained with limited impact to the comfort and mobility of a garment. The difficulty in air-gap implementation arises with achieving the separation between adjacent layers without the use of a bulky interstitial material. Assuming this difficulty is overcome, the improvements offered by air-gaps are extremely cost-effective in that their implementation yields limited relegation to the operational features of a garment.

3.3: Moisture Series

Moisture series assemblies consist of *PBI Matrix* outer shells, *RT-7100* moisture barriers, and two quilted *Glide / E89 723DWR* thermal liners. These thermal liner materials are used because they freely accept moisture. Two distinct assemblies are utilized, one with a split-layered thermal liner and the other with a traditionally layered thermal liner. These assemblies are identical except for the ordering of their constituent layers. Moisture series tests are conducted with dry and wet conditions, with wet tests incorporating the use of the fluid supply system. All wet tests utilize a constant fluid mass flux of approximately $1.4 \ g/m^2 s$. Additionally, moisture series tests utilize a radiant panel temperature setting of $250°C$.

The traditional thermal liner layering allows moisture from the baseplate to penetrate both layers of the thermal liner, whereas the split layering allows moisture to penetrate only the inner thermal liner permitting the outer thermal liner to remain dry. This series serves to examine the impact of moisture presence in the thermal liner on the protective performance of tested assemblies. The difference in results between the split and traditional arrangements is evaluated to determine the variations in performance associated with maintaining dry conditions in the thermal liner.

It is important to note that dry and wet condition tests are not directly compared because the thermal boundary condition at the baseplate differs between dry and wet tests. For wet tests, the baseplate is continuously supplied with ambient temperature fluid, altering the rate at which it increases in temperature as compared to dry tests. This also alters the rate of heat transfer through the assembly, preventing accurate comparison between the results of the two conditions.

Given the two variations of layer arrangement and two test conditions, there are four distinct assembly designations utilized for this series. These designations include M_s-D, M_t-D, M_s-W, and M_t-W. The subscripts s and t respectively designate a split or traditional arrangement of layers and the labels D and W respectively designate dry or wet conditions. The layers utilized in the split arrangement are progressively labeled from baseplate to radiation shield as *Plate*, *Shirt*, *Thermal Liner 1*, *Moisture Barrier*, *Thermal Liner 2*, and *Outer Shell*. Note that for the traditional arrangement, the *Moisture Barrier* and *Thermal Liner 2* layers are switched.

The time evolution of baseplate NTR parameters for each assembly is provided in **Figure 3.9** for dry conditions and **Figure 3.10** for wet conditions. As shown in **Figure 3.9**, there is no significant difference in NTR parameters between the split and traditional arrangements when tested in dry conditions. While some variations are observed, these lie within the uncertainty of the measurements. This indicates that, for dry conditions, the difference between the two arrangements produces roughly no change in the rate of temperature-rise at the inner surface of the assembly and that both offer equivalent protective performance.

As shown in **Figure 3.10**, NTR parameters decrease significantly for the split arrangement as compared to the traditional arrangement, indicating that the rate of temperature-rise is reduced at the inner surface of the split-layered assembly for wet conditions. This observation suggests that the wetting of the outer thermal liner in the traditionally layered assembly reduces its protective performance. Based on this trend, the assembly offering greater protective performance for wet conditions is M_s-W, with M_t-W offering reduced performance.
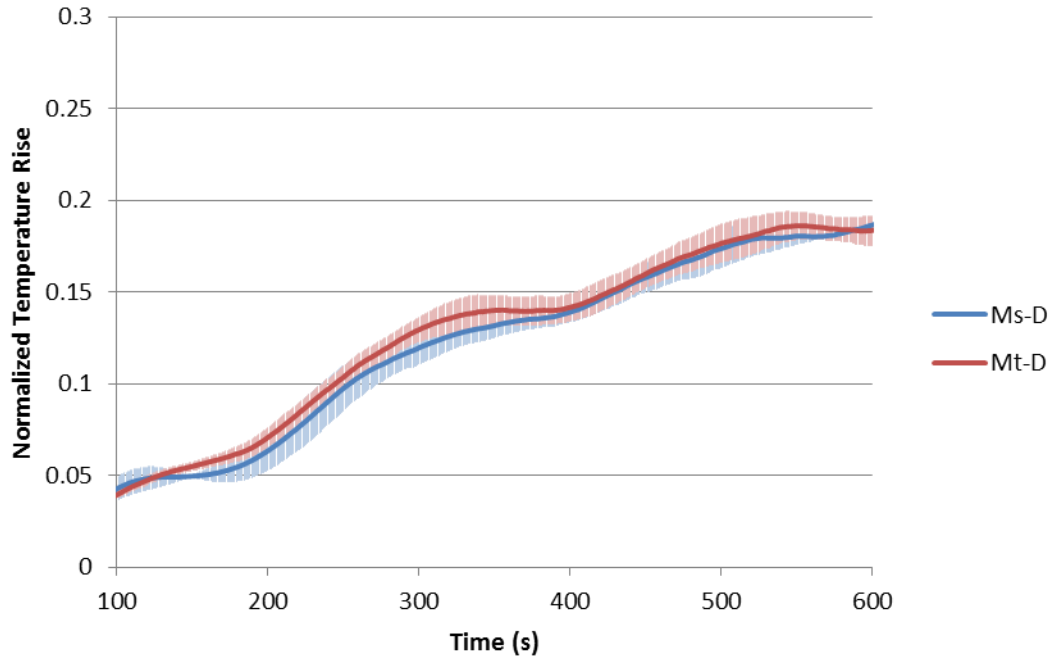
Figure 3.9: Time evolution of baseplate *NTR* parameters among moisture series assemblies for dry conditions
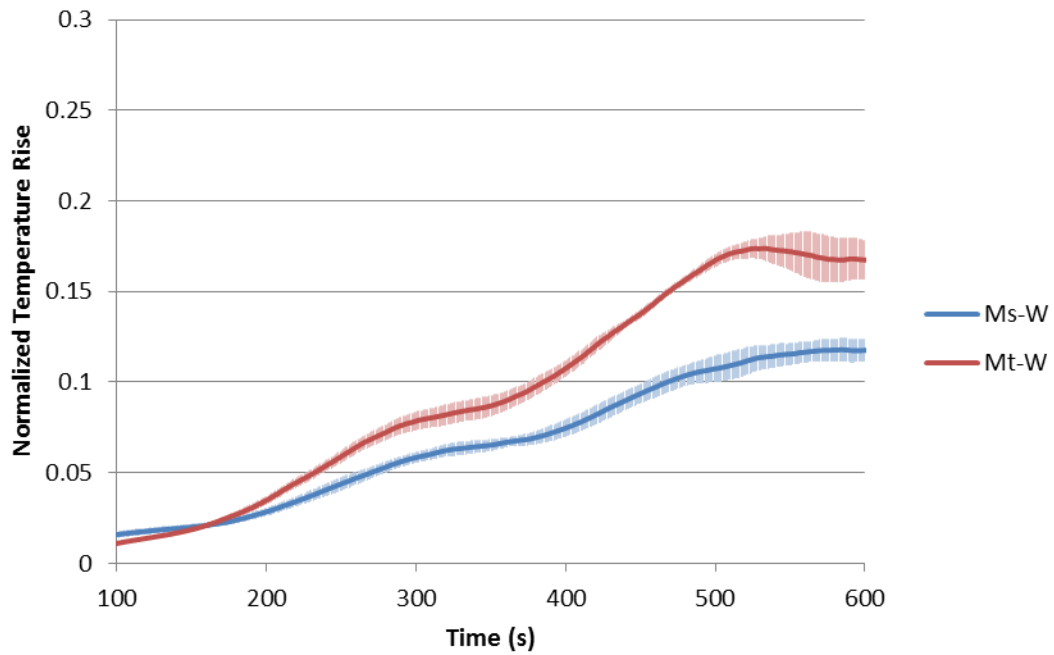
Figure 3.10: Time evolution of baseplate *NTR* parameters among moisture series assemblies for wet conditions

The NTR criteria for assemblies M_s-D, M_t-D, M_s-W, and M_t-W are respectively 0.020, 0.021, 0.012, and 0.020. Based on these values, assembly M_s-D measures a 4.8% reduction in NTR criterion as compared to assembly M_t-D. Similarly, assembly M_s-W measures a 40.0% reduction in NTR criterion as compared to assembly M_t-W. A summary of these data is provided in **Table 3.9**.

For dry conditions, the split arrangement provides a slight reduction in NTR criterion over the traditional arrangement; however, this reduction is within the uncertainty of the measurements. For wet conditions, the reduction in NTR criterion provided by the split arrangement is significant, indicating that maintaining dry conditions in the thermal liner improves the protective performance of the assembly.

Table 3.9: NTR criteria among moisture series assemblies

Layer Arrangement	Dry Conditions		Wet Conditions	
	NTR Criterion (min^{-1})	Improvement	NTR Criterion (min^{-1})	Improvement
Traditional	0.021	–	0.020	–
Split	0.020	4.8%	0.012	40.0%

The time evolution of NTG parameters characteristic of the inner and outer thermal liners within each assembly is provided in **Figure 3.11** for dry conditions and **Figure 3.12** for wet conditions. As shown in **Figure 3.11**, differences in NTG parameters between the two arrangements are negligible and within the uncertainty of the measurements when tested in dry conditions. This indicates that variation between the two arrangements provides roughly no change in the temperature gradient across either thermal liner layer and that both offer equivalent thermal resistance. This observation agrees with the NTR parameter trends for dry conditions.
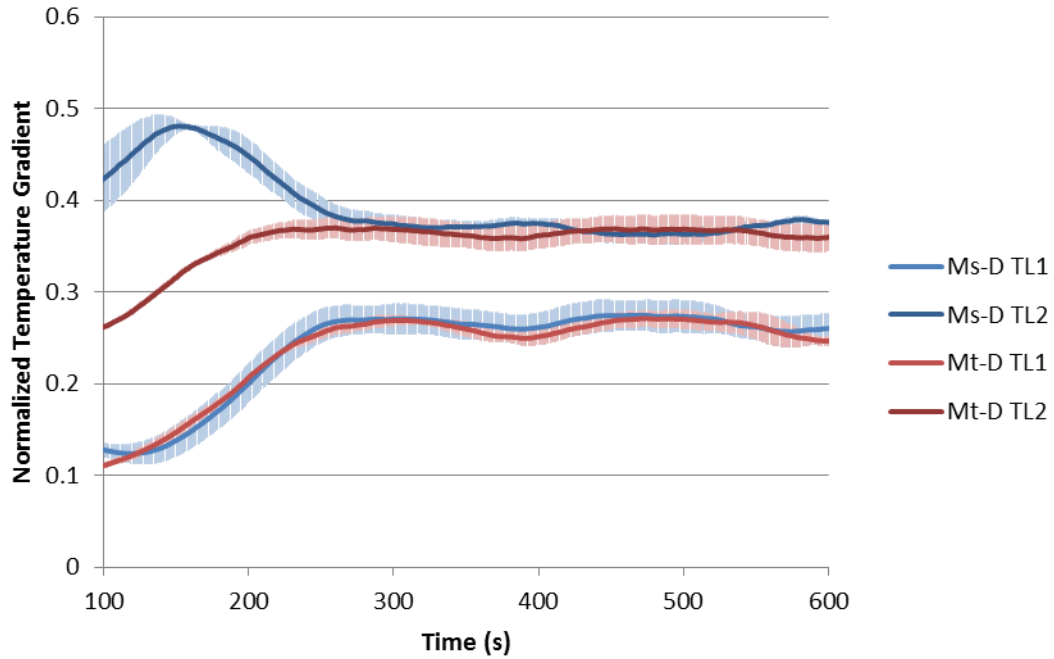
Figure 3.11: Time evolution of *NTG* parameters across the inner and outer thermal liner layers among moisture series assemblies for dry conditions
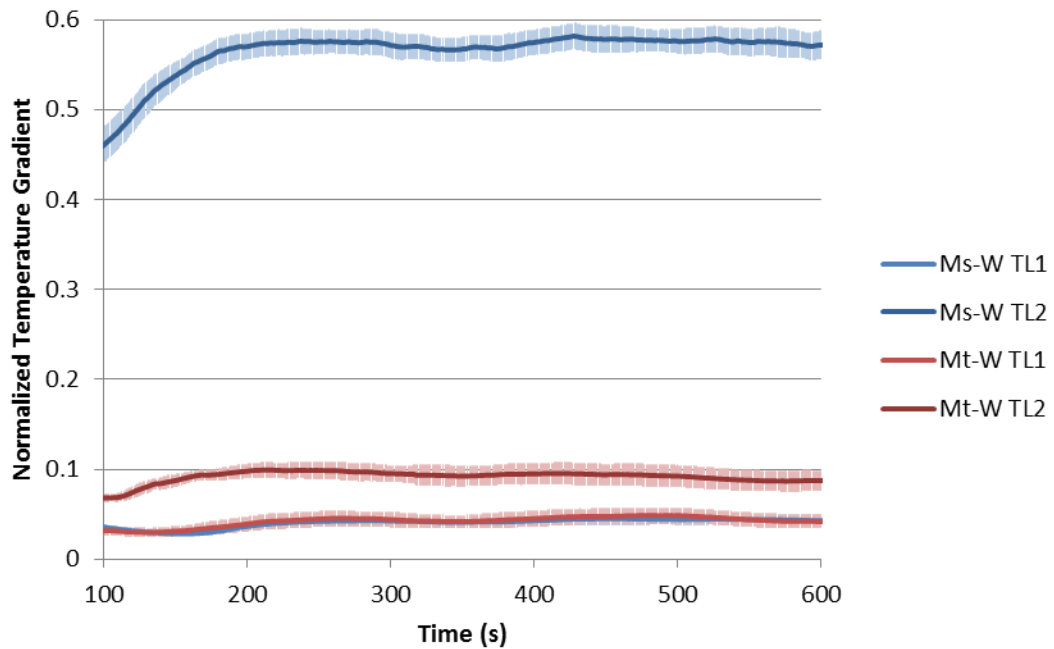
Figure 3.12: Time evolution of *NTG* parameters across the inner and outer thermal liner layers among moisture series assemblies for wet conditions

94

As shown in **Figure 3.12**, the outer thermal liner in the split arrangement measures significantly greater NTG parameters for wet conditions. This indicates that the temperature gradient across the outer thermal liner in the split arrangement is significantly greater than that for the traditional arrangement. The outer thermal liner in the split arrangement thus offers improved thermal resistance. This is expected because the outer thermal liner remains dry in the split arrangement, whereas it is subjected to moisture in the traditional arrangement. In comparison, there is no significant difference in NTG parameters for the inner thermal liner between the two arrangements because it is subjected to moisture in both.

The NTG criteria of the inner thermal liner layer for assemblies M_s-D, M_t-D, M_s-W, and M_t-W are respectively 0.259, 0.254, 0.044, and 0.043. Based on these values, assembly M_s-D measures a 2.0% increase in NTG criterion as compared to assembly M_t-D, and assembly M_s-W measures a 2.3% increase in NTG criterion as compared to assembly M_t-W. A summary of these data is provided in **Table 3.10**.

For both dry and wet conditions, the difference in NTG criterion of the inner thermal liner is negligible between the two arrangements and within the uncertainty of the measurements. This observation is expected because the position of the inner thermal liner does not change between split and traditionally layered assemblies.

Table 3.10: NTG criteria of the inner thermal liner layer among moisture series assemblies

Layer Arrangement	Dry Conditions		Wet Conditions	
	NTG Criterion	Improvement	NTG Criterion	Improvement
Traditional	0.254	–	0.043	–
Split	0.259	2.0%	0.044	2.3%

The NTG criteria of the outer thermal liner layer for assemblies M_s-D, M_t-D, M_s-W, and M_t-W are respectively 0.375, 0.362, 0.574, and 0.088. Based on these values, assembly M_s-D measures a 3.6% increase in NTG criterion as compared to assembly M_t-D, and assembly M_s-W measures a 552.3% increase in NTG criterion as compared to assembly M_t-W. A summary of these data is provided in **Table 3.11**.

The NTG criterion of the outer thermal liner is shown to increase for the split arrangement as compared to the traditional arrangement. For dry conditions, this increase is negligible and within the uncertainty of the measurements; however, for wet conditions the difference is significant. The observed increase for wet conditions is characteristic of a significant increase in the temperature gradient across the outer thermal liner and indicates that maintaining dry conditions in the outer thermal liner provides improved protective performance.

Table 3.11: NTG criteria of the outer thermal liner layer among moisture series assemblies

Layer Arrangement	Dry Conditions		Wet Conditions	
	NTG Criterion	Improvement	NTG Criterion	Improvement
Traditional	0.362	–	0.088	–
Split	0.375	3.6%	0.574	552.3%

As shown in this analysis, preventing moisture absorption in the thermal liner of a garment of firefighter protective clothing is found to increase greatly the thermal resistance provided by the thermal liner. This results in a reduction of both the rate of heat transfer through the garment and the rate of temperature-rise at the interior of the garment. Improvements are noted for both transient and steady-state conditions and yield an overall improvement to the thermal protection provided by the garment.

While the change in layer arrangement from a traditionally layered thermal liner to a split-layered thermal liner offers a negligible performance improvement for dry conditions, the observed improvement for wet conditions is significant. This is important because conditions encountered during the majority of firefighter operations involve some effect of moisture, whether by external sources such as hose streams or internal sources such as perspiration. As a result, improvements noted for wet conditions are more representative of the conditions experienced by firefighters during actual response activities. Though this analysis only considers moisture originating from internal sources, the results suggest maintaining dry conditions within the garment to be beneficial regardless of the origins of the moisture. This is because splitting the thermal liner into two separate layers prevents the simultaneous absorption of moisture by both layers from a single source of moisture.

It should be noted that the observed improvements to protective performance are achieved simply by rearranging the order of layers within a garment. No individual layers are modified and no additional layers are included. In effect, the observed improvements are achieved without negatively influencing the operational features of the garment such as by adding weight or reducing mobility. Interestingly, the accumulation of moisture actually increases the weight of a garment due to the additional mass of the moisture, also reducing both comfort and mobility. Maintaining dry conditions within the garment thus improves the operational features by preventing such moisture accumulation. The conversion from a traditional to a split-layered thermal liner is thus extremely cost-effective in that both the protective and operational features of the garment are improved.

3.4: Expanding Air-Gap Series

Expanding air-gap series assemblies consist of *PBI Matrix* outer shells, *Crosstech* moisture barriers, *Glide / E89 715M* thermal liners, and expanding layers containing shape-memory alloy rings. Six distinct assemblies are utilized, each including different combinations of expanding layer location and activation temperature. The two locations include placement of the expanding layer on either the outer or inner side of the moisture barrier, and the two activation temperatures include $50°C$ and $90°C$. Two additional assemblies are tested, lacking inclusion of the shape-memory rings. Expanding air-gap series tests are conducted with dry conditions and do not incorporate the use of the fluid supply system. Additionally, expanding air-gap series tests utilize a radiant panel temperature setting of $250°C$.

This series serves to evaluate the successful applicability of shape-memory materials to firefighter protective clothing design and to examine the influence of their presence on protective performance. Differences in performance between the different expanding layer placements and activation temperatures are also evaluated to determine the ideal implementation of shape-memory materials offering the greatest improvement to thermal protection.

The six assemblies used in this series include assemblies E_o-50, E_o-90, E_o-∅, E_i-50, E_i-90, and E_i-∅. The subscripts o and i respectively designate the outer or inner placement of the expanding layer and the labels 50 and 90 respectively designate the use of $50°C$ or $90°C$ activation temperature rings. The ∅ label indicates assemblies for which the shape-memory rings are removed from the pockets of the expanding layer. The layers within the inner placement assemblies are progressively

labeled from baseplate to radiation shield as *Plate*, *Shirt*, *SMR Assembly*, *Moisture Barrier*, *Thermal Liner*, and *Outer Shell*. Note that for outer placement assemblies, the order of the *SMR Assembly* and *Thermal Liner* layers is reversed.

The time evolution of baseplate NTR parameters for each assembly is provided in **Figure 3.13**. As shown in the figure, there is a significant reduction in NTR parameters for assemblies containing shape-memory rings as compared to assemblies without. This trend indicates that activation of the shape-memory rings successfully produces an expanding air-gap and that this effect significantly reduces the rate of temperature-rise at the inner surface of the assemblies.
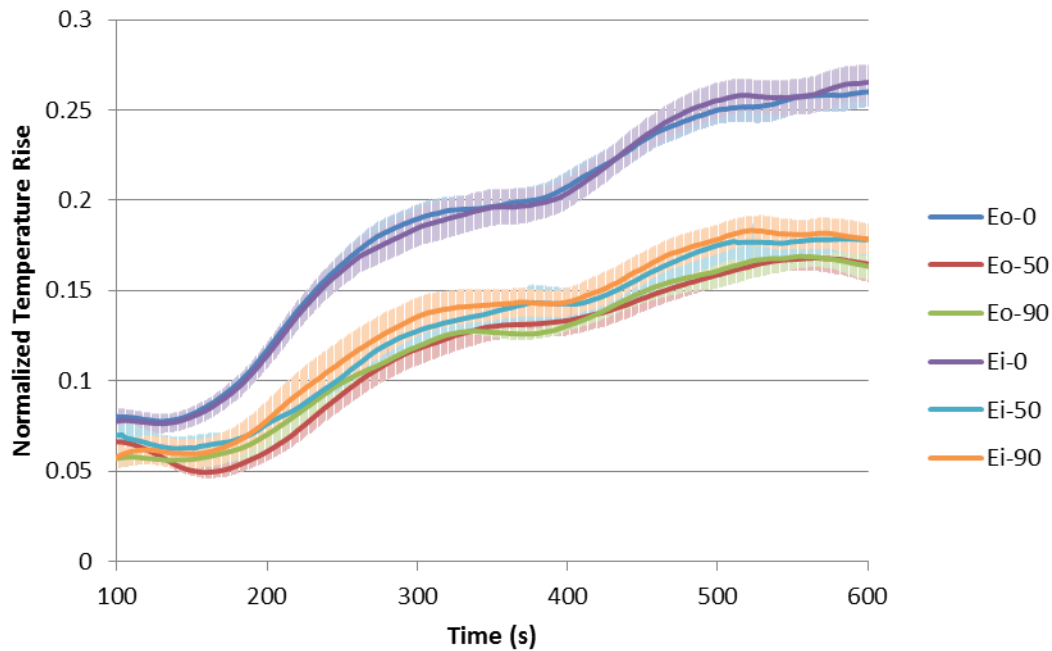
Figure 3.13: Time evolution of baseplate NTR parameters among expanding air-gap series assemblies

Comparing assemblies containing shape-memory rings, NTR parameters decrease slightly for outer placement of the expanding layer as compared to inner placement. Similarly, NTR parameters decrease slightly for $50°C$ activation as

99

compared to $90°C$ activation. These trends are expected because both outer placement and lower activation temperature reduce the response time of the expanding layer to the thermal exposure. It should be noted that though these trends are expected, they are insignificant in that they lie within the uncertainty of the measurements.

Between the two assemblies lacking shape-memory rings, there is no significant difference in NTR parameters, with slight variations lying within the uncertainty of the measurements. This indicates that, without the expansion effect, expanding layer placement does not affect performance. Considering these trends, assembly E_o-50 offers the greatest protective performance, with E_o-90, E_i-50, E_i-90, E_o-$\emptyset$, and E_i-$\emptyset$ offering progressively reduced protection.

The NTR criteria for assemblies E_o-50, E_o-90, E_i-50, E_i-90, E_o-$\emptyset$, and E_i-$\emptyset$ are respectively 0.013, 0.015, 0.015, 0.017, 0.026, and 0.026. Based on these values, assemblies containing shape-memory rings show a significant reduction in NTR criterion as compared to assemblies without. With outer expanding layer placement, inclusion of the shape-memory rings offers a reduction in NTR criterion of 42.3% for $90°C$ activation and 50.0% for $50°C$ activation. With inner placement, reductions decrease slightly to 34.6% for $90°C$ and 42.3% for $50°C$.

Inclusion of the shape-memory rings provides a slightly greater benefit to protective performance for outer placement of the expanding layer as compared to inner placement, and for $50°C$ activation as compared to $90°C$. It is important to note that these variations in NTR criterion lie within the uncertainty of the measurements and that only the performance improvements noted by inclusion of the shape-memory rings are significant. A summary of these data is provided in **Table 3.12**.

Table 3.12: NTR criteria among expanding air-gap series assemblies

SMR Inclusion	Outer Placement		Inner Placement	
	NTR Criterion (min^{-1})	Improvement	NTR Criterion (min^{-1})	Improvement
No SMR	0.026	–	0.026	–
90°C SMR	0.015	42.3%	0.017	34.6%
50°C SMR	0.013	50.0%	0.015	42.3%

The time evolution of NTG parameters characteristic of the expanding layer within each assembly is provided in **Figure 3.14**. As shown in the figure, NTG parameters are significantly greater for assemblies containing the shape-memory rings as compared to assemblies without. As with the NTR parameters, this indicates that activation of the shape-memory rings successfully produces an expanding air-gap within the assembly, increasing the thermal resistance of the expanding layer.

Among assemblies containing shape-memory rings, variations in NTG parameters between differing activation temperatures are negligible. This observation is expected because, for steady-state conditions in which expansion has already occurred, activation temperature does not affect the thermal resistance of the expanding layer. Conversely, NTG parameters noticeably increase with outer placement as compared to inner placement, indicating that outer placement provides an increase in the thermal resistance of the expanding layer.

As was the case for NTR parameters, differences in expanding layer placement yield a negligible impact on NTG parameters for the two assemblies lacking shape-memory rings. This indicates that, without the expansion effect, layer order does not significantly affect the thermal resistance of the expanding layer.
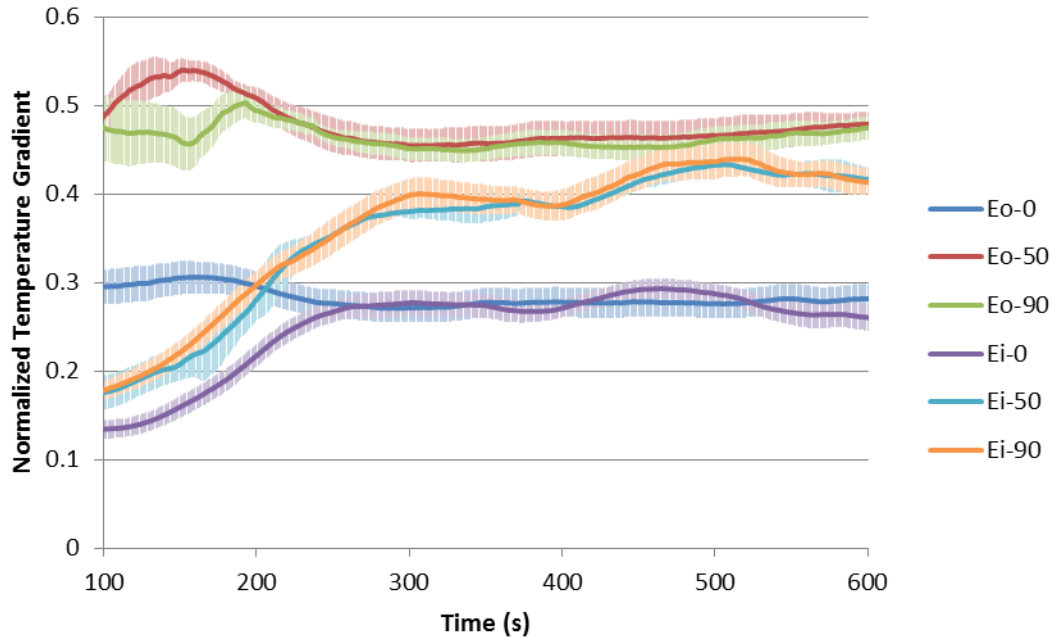
Figure 3.14: Time evolution of NTG parameters across the expanding layer among expanding air-gap series assemblies

The NTG criteria for assemblies E_o-50, E_o-90, E_i-50, E_i-90, E_o-Ø, and E_i-Ø are respectively 0.476, 0.472, 0.419, 0.418, 0.281, and 0.263. Based on these values, assemblies containing shape-memory rings show a significant increase in NTG criterion as compared to assemblies without. With outer expanding layer placement, inclusion of the shape-memory rings provides an increase in NTG criterion of 68.0% for 90°C activation and 69.4% for 50°C activation. With inner placement, increases reduce slightly to 58.9% for 90°C and 59.3% for 50°C.

The improvements provided by inclusion of the shape-memory rings are greater for outer placement as compared to inner placement, and slightly greater for 50°C activation as compared to 90°C. As with the NTR criteria, differences in NTG criteria between differing activation temperatures are negligible and lie within the uncertainty of the measurements. A summary of these data is provided in **Table 3.13**.

Table 3.13: NTG criteria of the expanding layer among expanding air-gap series assemblies

SMR Inclusion	Outer Placement		Inner Placement	
	NTG Criterion	Improvement	NTG Criterion	Improvement
No SMR	0.281	–	0.263	–
90°C SMR	0.472	68.0%	0.418	58.9%
50°C SMR	0.476	69.4%	0.419	59.3%

As evidenced by the observed trends, the implementation of a thermally activated expanding layer within a garment of firefighter protective clothing is shown to effectively improve thermal protection. This improvement is the result of an expanding air-gap within the garment that reduces the rate of temperature-rise at the garment interior. Improvements are shown for both transient and steady-state conditions and yield an overall increase in the performance of the garment.

In testing different placements of the expanding layer, it is shown that placement between the outer layers of a garment provides improved performance as compared to inner placement; however, this improvement is only with respect to the individual thermal resistance of the expanding layer. Though slight improvement with respect to overall assembly performance is noted for outer placement, these variations lie within the uncertainty of the data and do not justify a significant result.

It is also found that no significant performance differences are obtained by varying the activation temperature of the expanding layer. Though slight performance improvements are observed with lower activation temperatures, these variations also lie within the uncertainty of the data. Despite this observation, the activation temperature of the shape-memory material remains an important factor. While

arbitrarily low activation temperatures result in a constant state of activation that causes unnecessary reductions to comfort and mobility, arbitrarily high activation temperatures result in the failed activation of the expanding layer and an unnecessary loss of protection. In order to ensure the effective operation of the expanding layer, activation temperatures must represent expected thermal exposure conditions.

Interestingly, because the air-gap created by the expanding layer comprises an array of enclosed pockets, the effects of convective heat transfer are minimized. This is because the convective eddies that form within the air-gap are confined to each pocket and are not able to freely transport thermal energy through the air-gap. As a result, the expanding layer can assume large thicknesses in any orientation without suffering a reduction in performance due to convective heat transfer.

Considering the numerous benefits provided by the expanding layer, it is important to note that such benefits are achieved without prohibitively relegating the operational features of a garment. The increased cost associated with the expanding layer is minor because only a small amount of shape-memory material is required to achieve a significant performance improvement. Similarly, increased weight is minor because a layer of shape-memory rings weighs no more than an additional layer of fabric. Due to the shape-memory effect derived activation, expansion of the expanding layer is entirely thermally induced. As a result, additional protection is provided only when necessary, ensuring that nonessential reductions to comfort and mobility due to increased bulkiness do not occur. Considering these features, implementation of a shape-memory expanding layer provides a cost-effective means of improving the protective performance of firefighter protective clothing.

Chapter 4 : Conclusions

4.1: Summary of Results

In this thesis, an experimental analysis is presented examining the protective performance of a collection of firefighter protective clothing assemblies. Several series of tests are conducted, each assessing the influence of various modifications on assembly performance. These performances are rated using normalized parameters, including NTR and NTG criteria, each derived from measured temperature data. In summarizing the test results, it is important to evaluate the quality of comparison provided by each of these criteria in order to establish which criterion is best suited to compare assembly performance across all test series.

While NTR and NTG criteria are both useful in evaluating the performance of an assembly, the scopes of their comparative qualities differ. NTG criteria isolate the performance of individual layers within an assembly. In comparison, NTR criteria integrate the performance of all layers, quantifying the overall performance of an assembly. When an individual layer in an assembly is modified, the NTG criteria characteristic of the modified layer vary directly with the impact of those modifications on the performance of the modified layer. Conversely, NTR criteria vary with the impact of those modifications on the modified layer filtered by the relative influence of the modified layer on the overall performance of the assembly.

For assemblies in which the modified layer is crucial, variations in NTR and NTG criteria remain roughly equal. For assemblies in which the modified layer is trivial, variations in NTR criteria are significantly less than variations in NTG

criteria. NTG criteria are useful in examining the direct effects of modifications on the performance of individual layers; however, they do not provide an accurate measure of the net effects of modifications on overall assembly performance. As a result, NTR criteria serve as the basis for comparing the influence of assembly modifications on protective performance across all test series.

As evidenced by the several test series presented in this analysis, it is possible to improve the performance of firefighter protective clothing through a number of varying garment modifications. These modifications range from increasing the thickness of protective layers to altering layer position and orientation. A summary of the performance improvements provided by the various assembly modifications investigated in this analysis, organized by test series, are provided in **Table 4.1**.

Table 4.1: Summary of performance improvements provided by various assembly modifications

Test Series	Assembly	NTR Criterion (min^{-1})	Improvement
Lion	L-C	0.035	–
	L-X	0.032	8.9%

Static Air-Gap	A-0	0.032	–
	A-1	0.024	25.0%
	A-2	0.021	34.3%
	A-4	0.017	46.8%

Moisture	M_t-W	0.020	–
	M_s-W	0.012	40.0%

Expanding Air-Gap	E_o-$\emptyset$	0.026	–
	E_o-50	0.013	50.0%

As shown in **Table 4.1**, there are significant differences in the improvements provided by the various assembly modifications. For lion series tests, performance improvements are noted for increasing the thickness of assembly layers. Considering thermal liners, an 8.9% reduction in NTR criterion is measured for assemblies including an *X-Liner* thermal liner as compared to a *C-Liner* thermal liner, where the *X-Liner* includes an additional layer of insulation that the *C-Liner* lacks. As a result, the measured reduction in NTR criterion is representative of the improvement provided by including an additional insulation layer within a protective garment.

For static-air gap series tests, performance improvements are noted for inclusion of a dedicated air-gap between assembly layers. Reductions in NTR criterion of 25.0%, 34.3%, and 46.8% are measured for respective air-gap thicknesses of $7\ mm$, $14\ mm$, and $28\ mm$. With each increase in air-gap thickness, assembly performance is improved; however, the observed improvement per-unit-thickness of the air-gap decreases with increasing thickness. These reductions in NTR criterion are representative of the improvement provided by increasing the thickness of the air-gaps occurring between adjacent layers within a protective garment.

For moisture series tests, performance improvements are noted for rearranging the ordering of assembly layers. With a traditional thermal liner arrangement, the entire thermal liner is exposed to perspiration moisture. With a split thermal liner arrangement, only the inner thermal liner layer is exposed to perspiration moisture, allowing the outer thermal liner layer to remain dry. For wet conditions, a 40.0% reduction in NTR criterion is measured for a split arrangement as compared to a traditional arrangement. This reduction in NTR criterion is representative of the

improvement provided by maintaining dry conditions in the thermal liner of a protective garment.

For expanding air-gap series tests, performance improvements are noted for including a shape-memory material expanding layer within assemblies. Activation of the shape-memory materials comprising this layer produces a separation effect that creates an expanding air-gap within the assembly. For outer placement of the expanding layer with an activation temperature of $50°C$, a 50.0% reduction in NTR criterion is measured with the expanding layer. This reduction in NTR criterion is representative of the improvement provided by the implementation of a dynamic, thermally responsive air-gap within a protective garment.

Ideally, garment modifications improve performance without relegating operational features such as cost, comfort, weight, and mobility. Rearranging the order of layers and increasing the thickness of air-gaps between layers are ideal improvements because they have a minimal negative influence on operational features. Adding an insulation layer and implementing a shape-memory expanding layer are not as ideal because these modifications have a measurable negative influence on operational features. It is important to note that these two modifications have an approximately equal negative influence on operational features.

As shown in **Table 4.1**, the performance improvement provided by the shape-memory expanding layer is the greatest of the assembly modifications considered in this analysis and profoundly greater than that provided by an additional insulation layer. As a result, implementation of a shape-memory expanding layer remains a beneficial modification with respect to the overall effectiveness of a garment.

The body of research examining firefighter protective clothing is extensive, specifically with respect to the influence of moisture and air-gaps. Still, this body of research is incomplete and additional studies are necessary to promote a more accurate understanding of the physical mechanisms governing the performance of firefighter protective clothing. Several topics that specifically continue the research presented in this thesis and have yet to be studied in detail are presented as follows.

In this thesis, the influence of moisture transport within firefighter protective clothing is considered, but only with respect to a constant flow rate of moisture originating at the inner surface of a garment. In order to analyze the influence of moisture further, it is recommended that future studies examine moisture originating from external sources or simultaneously from internal and external sources. In addition, varying flow rates of moisture should be studied to examine the influence of parameters such as perspiration rate on firefighter protective clothing performance.

While this thesis considers moisture, it does not directly examine the effects of moisture phase-change. Considering the large latent heat associated with moisture phase-change, condensation and evaporation effects potentially have a profound impact on the performance of firefighter protective clothing. A comprehensive theoretical model combining the simultaneous transport of heat and moisture through a multilayer fabric in the presence of perspiration, condensation, and evaporation has yet to be developed. It is recommended that future studies strive to develop such a model, as this would greatly advance an accurate understanding of the fundamental phenomena governing the performance of firefighter protective clothing.

Though this thesis considers the effects of both static and expanding air-gaps, only a single orientation is studied involving a horizontal air-gap with application of heat from above. It is necessary for future studies to examine alternative air-gap orientations and directional applications of heat, particularly those involving vertical air-gaps heated from below. This orientation maximizes the occurrence of convective heat transfer within the air-gap and allows analysis of the coupled effects of convection and increasing air-gap thickness in a worst-case orientation. In addition, future studies should investigate which air-gap sizes and orientations are most representative of those occurring within firefighter protective clothing during normal usage. Such research provides a basis for understanding how residual air-gaps contribute to the performance of firefighter protective clothing.

This thesis provides a pioneering investigation of the applicability of shape-memory materials within firefighter protective clothing; however, only a single type and orientation of shape-memory material is utilized. It is recommended that future studies analyze alternative implementations, including different shape-memory alloys or polymers in varying shapes and orientations. Additionally, this thesis utilizes laboratory testing with a static layered assembly exposed to a controlled, primarily radiant thermal exposure. It is necessary for future studies to conduct further testing of shape-memory materials within actual garments of firefighter protective clothing and exposures to actual fire conditions. Such research ensures that the bench-scale results observed in this thesis translate to actual conditions.

It is important to note that this list of recommendations is not exhaustive and that there exist a number of firefighter safety topics yet to be explored in detail.

Appendices

A: Derivation of the Heat Diffusion Equation

The following generalized approach describes the derivation of the mathematical expressions governing the diffusion of heat within a system. Applying the first law of thermodynamics to an arbitrary system with constant volume and assuming no net transfer of work or mass between the system and its surroundings yields the following statement of energy conservation.

$$\frac{dE}{dt} = \dot{q} \tag{A.1}$$

In this expression, E is the total energy contained within the system and $\dot{q}$ is the rate of heat transfer between the system and surroundings. Considering a system comprised of a collection of individual elements, each with a characteristic uniform temperature, the energy contained within the system can be re-expressed as follows.

$$\frac{dE}{dt} = \oiiint \left(\rho c \frac{\partial T}{\partial t} \right) dV \tag{A.2}$$

In this expression, ρ, c, and T are respectively the mass density, heat capacity, and temperature of each element within the system. Following a similar formulation, the rate of heat transfer between the system and surroundings is expressed as follows.

$$\dot{q} = - \oiint (\dot{\boldsymbol{q}}'' \cdot \vec{\boldsymbol{n}}) dA + \oiiint \dot{q}''' dV \tag{A.3}$$

In this expression, $\dot{\boldsymbol{q}}''$ and $\vec{\boldsymbol{n}}$ are vector quantities respectively designating the heat flux into, and the outward directed unit vector normal to, a surface element at the interface between the system and surroundings. $\dot{q}'''$ is a source-term designating the

volumetric rate of change of heat within the system. Note that the first term in this expression simply represents the flux of heat into or out of the system, while the second term represents the generation or consumption of heat within the system.

By the Divergence Theorem, the first term in equation $(A.3)$ can be re-expressed as follows [23].

$$\oiint (\dot{\boldsymbol{q}}'' \cdot \vec{\boldsymbol{n}})dA = \oiiint (\nabla \cdot \dot{\boldsymbol{q}}'')dV \qquad (A.4)$$

Applying equation $(A.4)$ to equation $(A.3)$ then yields the following.

$$\dot{q} = -\oiiint (\nabla \cdot \dot{\boldsymbol{q}}'')dV + \oiiint \dot{q}''' dV \qquad (A.5)$$

Combining this result with equations $(A.1)$ and $(A.2)$ yields the following.

$$\oiiint \left(\rho c \frac{\partial T}{\partial t}\right)dV = -\oiiint \nabla \cdot \dot{\boldsymbol{q}}'' dV + \oiiint \dot{q}''' dV \qquad (A.6)$$

Because the integrations within this expression are all with respect to the total volume of the system, collecting the integrands in each term allows the following simplification.

$$\oiiint \left(\rho c \frac{\partial T}{\partial t} + \nabla \cdot \dot{\boldsymbol{q}}'' - \dot{q}'''\right)dV = 0 \qquad (A.7)$$

Note that this expression is satisfied for any arbitrarily defined volume within the system. This condition is met if and only if the integrand itself is equal to zero at all locations within the system, implying the following result.

$$\rho c \frac{\partial T}{\partial t} + \nabla \cdot \dot{\boldsymbol{q}}'' - \dot{q}''' = 0 \qquad (A.8)$$

It is important to note that equation $(A.8)$ is valid throughout any arbitrarily defined system satisfying the original assumptions. In order to close this expression to a useable form, it is necessary to provide an independent expression relating the heat flux and temperature within the system. Assuming heat transfer within the system consists only of conduction, such an expression is obtained through the following statement of Fourier's Law [6].

$$\dot{q}'' = -\lambda \nabla T \qquad (A.9)$$

In this expression, $\dot{q}''$ gives the conduction heat flux within the system, λ is the thermal conductivity of the system, and ∇T is the temperature gradient within the system. Applying this relationship to equation $(A.8)$ yields the following.

$$\rho c \frac{\partial T}{\partial t} = \nabla \cdot \lambda \nabla T + \dot{q}''' \qquad (A.10)$$

Assuming the thermal conductivity of the system is a constant isotropic scalar quantity, neglecting the heat source-term, and only considering heat transfer in a single dimension, this expression is then simplified to the following result.

$$\frac{\partial T}{\partial t} = \frac{\lambda}{\rho c} \frac{\partial^2 T}{\partial x^2} \qquad (A.11)$$

Equation $(A.11)$ provides a partial differential relationship describing the spatial distribution of temperature within an arbitrary system as a function of time. Note that it is convenient to combine the system properties in equation $(A.11)$ into a single quantity by defining the thermal diffusivity of the system, D_{th}.

$$\frac{\partial T}{\partial t} = D_{th} \frac{\partial^2 T}{\partial x^2} \qquad (A.12)$$

B: Numerical Solution of the Heat Diffusion Equation

The previously derived heat diffusion equation, provided in *Appendix A* as equation $(A.12)$, is solved numerically by adopting a finite difference approach utilizing an Euler implicit, central differencing scheme. This approach produces a numerical approximation that is first order accurate in time, second order accurate in space, and can be shown to be unconditionally stable. The adopted scheme yields the following expression, where the partial derivatives of the governing equation are simply evaluated in terms of discretized approximations.

$$\frac{T_i^{n+1} - T_i^n}{\Delta t} = D_{th} \frac{T_{i-1}^{n+1} - 2T_i^{n+1} + T_{i+1}^{n+1}}{\Delta x^2} \qquad (B.1)$$

In this expression, T_i^n gives the temperature within an arbitrary system at position i and time n, D_{th} is the thermal diffusivity of the system, and Δt and Δx are respectively the temporal and spatial increments of the discretization. In order to solve this expression, it is necessary to rearrange the terms such that the temperature distribution within the system at a particular time step is given as a function of the temperature distribution at the previous time step. In so doing, it is useful to introduce the Fourier number, Fo, which characterizes the ratio of heat diffusion to thermal energy storage within the system. Rearranging equation $(B.1)$ in this manner yields the following time advancement scheme.

$$Fo = \frac{D_{th}\Delta t}{\Delta x^2} \qquad (B.2)$$

$$(-Fo)T_{i-1}^{n+1} + (1 + 2Fo)T_i^{n+1} + (-Fo)T_{i+1}^{n+1} = T_i^n \qquad (B.3)$$

The time advancement scheme given in equation $(B.3)$ is subsequently re-expressed to yield the following matrix formulation, which is easily evaluated by a mathematical software package such as MATLAB®. Note that the left-hand-side of equation $(B.3)$ forms a tri-diagonal matrix in which only the cells along the main diagonal and the diagonals directly above and below the main diagonal assume nonzero values equal to the Fourier number coefficients from the expression.

$$\begin{bmatrix} 1 & 0 & 0 & \cdots & \cdots & \cdots & 0 & 0 & 0 \\ -Fo & 1+2Fo & -Fo & 0 & \cdots & \cdots & \cdots & 0 & 0 \\ 0 & \ddots & \ddots & \ddots & \ddots & \ddots & \ddots & \ddots & 0 \\ \vdots & \ddots & -Fo & 1+2Fo & -Fo & 0 & 0 & \ddots & \vdots \\ \vdots & \ddots & 0 & -Fo & 1+2Fo & -Fo & 0 & \ddots & \vdots \\ \vdots & \ddots & 0 & 0 & -Fo & 1+2Fo & -Fo & \ddots & \vdots \\ 0 & \ddots & \ddots & \ddots & \ddots & \ddots & \ddots & \ddots & 0 \\ 0 & 0 & \cdots & \cdots & \cdots & 0 & -Fo & 1+2Fo & -Fo \\ 0 & 0 & 0 & \cdots & \cdots & \cdots & 0 & 0 & 1 \end{bmatrix}$$

$$\times \begin{bmatrix} T_1 \\ T_2 \\ \vdots \\ T_{i-1} \\ T_i \\ T_{i+1} \\ \vdots \\ T_{\delta-1} \\ T_\delta \end{bmatrix}^{n+1} = \begin{bmatrix} T_1 \\ T_2 \\ \vdots \\ T_{i-1} \\ T_i \\ T_{i+1} \\ \vdots \\ T_{\delta-1} \\ T_\delta \end{bmatrix}^{n} \qquad (B.4)$$

It is important to note that this formulation is only valid for positions within the system and it is necessary to develop independent expressions governing the heat transfer conditions at the system boundaries. Assuming these boundary conditions are given by convective heat transfer, the following expressions define the time evolution of temperature at the system boundaries.

$$-\lambda \frac{\partial T_1^{n+1}}{\partial x} = h_1\left(T_{\infty,1} - T_1^n\right), \qquad -\lambda \frac{\partial T_\delta^{n+1}}{\partial x} = h_\delta\left(T_\delta^n - T_{\infty,\delta}\right) \qquad (B.5, B.6)$$

In equations $(B.5)$ and $(B.6)$, λ is the thermal conductivity of the system, T_∞ is the free-stream temperature of the system surroundings, and h is the convective heat transfer coefficient between the system and surroundings. Note that for the one-dimensional system considered in this analysis, the subscripts 1 and δ respectively refer to the left and right system boundaries. Applying numerical approximations to the derivatives in these expressions yields the following.

$$T_1^{n+1} = T_2^{n+1} + \frac{h_1 \Delta x}{\lambda} \left(T_{\infty,1} - T_1^n\right) \qquad (B.7)$$

$$T_\delta^{n+1} = T_{\delta-1}^{n+1} - \frac{h_\delta \Delta x}{\lambda} \left(T_\delta^n - T_{\infty,\delta}\right) \qquad (B.8)$$

Combining these boundary conditions with the previous matrix formulation given by equation $(B.4)$ allows the temperature distribution within the system to be evaluated by a computational algorithm. For this analysis, a MATLAB® script is used to construct and evaluate such an algorithm. The system of interest is prescribed to consist of a one-dimensional layer of material specified with the thermal properties of either air or liquid water, a thickness of $0.01\ m$, and a uniform initial temperature distribution of $300\ K$. The free-stream temperatures of the system surroundings at the left and right boundaries are respectively defined as $500\ K$ and $300\ K$, each with an associated convective heat transfer coefficient of $20\ W/m^2K$.

For the system with air thermal properties, the algorithm is defined with a spatial and temporal discretization of respectively $1 * 10^{-5}\ m$ and $2 * 10^{-5}\ s$ and a simulation time of $5\ s$. Similarly, the algorithm for the system with liquid water thermal properties is defined with a spatial and temporal discretization of respectively $5 * 10^{-5}\ m$ and $5 * 10^{-3}\ s$ and a simulation time of $7200\ s$.

The MATLAB® script utilized to solve the numerical formulation for the system with air thermal properties is provided below. Note that for the system with liquid water thermal properties, the thermal conductivity, mass density, heat capacity, time duration, and spatial and temporal discretization are appropriately modified.

```matlab
%Thermal properties of air
k = 0.0263;         %Thermal conductivity (W/mK)
p = 1.1614;         %Mass density (kg/m3)
c = 1007.0;         %Heat capacity (J/kgK)

Dth = (k/p/c);      %Thermal diffusivity of system (m2/s)
Ith = (k*p*c);      %Thermal inertia of system (kg2/s5K2)
h1 = 20;            %Convection coefficient at left boundary (W/m2K)
hL = 20;            %Convection coefficient at right boundary (W/m2K)
To = 300;           %Initial temperature of system (K)
Tf1 = 500;          %Free-stream temperature at left boundary (K)
TfL = 300;          %Free-stream temperature at right boundary (K)

Lx = 0.01;          %Thickness of system (m)
dx = 0.00001;       %Spatial step (m)
x = (0:dx:Lx);
nx = numel(x);

Lt = 5.0;           %Time duration (s)
dt = 0.00002;       %Time step (s)
t = (0:dt:Lt);
nt = numel(t);

Fo = (Dth*dt)/(dx^2); %Fourier number

%Form tri-diagonal coefficient matrix
M = zeros(nx,nx);
M(1,1)      = 1;
M(1,2)      = 0;
for i = 2:(nx-1)
    M(i,i-1) = (-Fo);
    M(i,i)   = (1+(2*Fo));
    M(i,i+1) = (-Fo);
end
M(nx,nx-1)  = 0;
M(nx,nx)    = 1;

%Define initial temperature distribution within system
T = To*ones(nx,nt);

%Advance temperature distribution at each time step
for n = 2:nt
    T(:,n) = M\T(:,(n-1));
    T(1,n) = T(2,n)+(h1*dx/k*(Tf1-T(1,n-1)));      %Left boundary
    T(nx,n)= T(nx-1,n)+(hL*dx/k*(TfL-T(nx,n-1))); %Right boundary
end
```

117

In order to verify the solutions produced by the previously described numerical approach, the numerical solutions are compared against an analytical solution for steady-state conditions and an additional analytical solution for transience that assumes an infinite back boundary condition.

The analytical solution for steady-state conditions is derived as follows. At steady-state, the flux of thermal energy throughout the system is constant, including positions at the system boundaries. This condition is defined by the following expression.

$$\dot{q}'' = h_1(T_{\infty,1} - T_1) = \frac{\lambda}{\delta}(T_1 - T_\delta) = h_\delta(T_\delta - T_{\infty,\delta}) \qquad (B.9)$$

Solving these expressions simultaneously for the temperature distribution within the system yields the following.

$$T_1 = T_{\infty,1} - \frac{(T_{\infty,1} - T_{\infty,\delta})}{1 + \dfrac{h_1}{h_\delta} + \dfrac{h_1\delta}{\lambda}}, \qquad T_\delta = T_{\infty,\delta} + \frac{(T_{\infty,1} - T_{\infty,\delta})}{1 + \dfrac{h_\delta}{h_1} + \dfrac{h_\delta\delta}{\lambda}} \qquad (B.10, B.11)$$

$$T(x) = (T_\delta - T_1)\frac{x}{\delta} + T_1 \qquad (B.12)$$

This solution is evaluated within the previously introduced MATLAB® script with the addition of the following lines of code. The solutions of the numerical approach and the analytical steady-state expression are compared in **Figure B.1**. As shown in the figure, the blue numerical solutions appropriately converge to the red steady-state solution as the steady-state condition is approached.

```
%Solve steady-state temperature distribution
T1 = Tf1-((Tf1-TfL)/(1+((h1*Lx)/k)+(h1/hL)));
TL = TfL+((Tf1-TfL)/(1+((hL*Lx)/k)+(hL/h1)));
Ts = T1+((TL-T1)*(x./Lx));
```
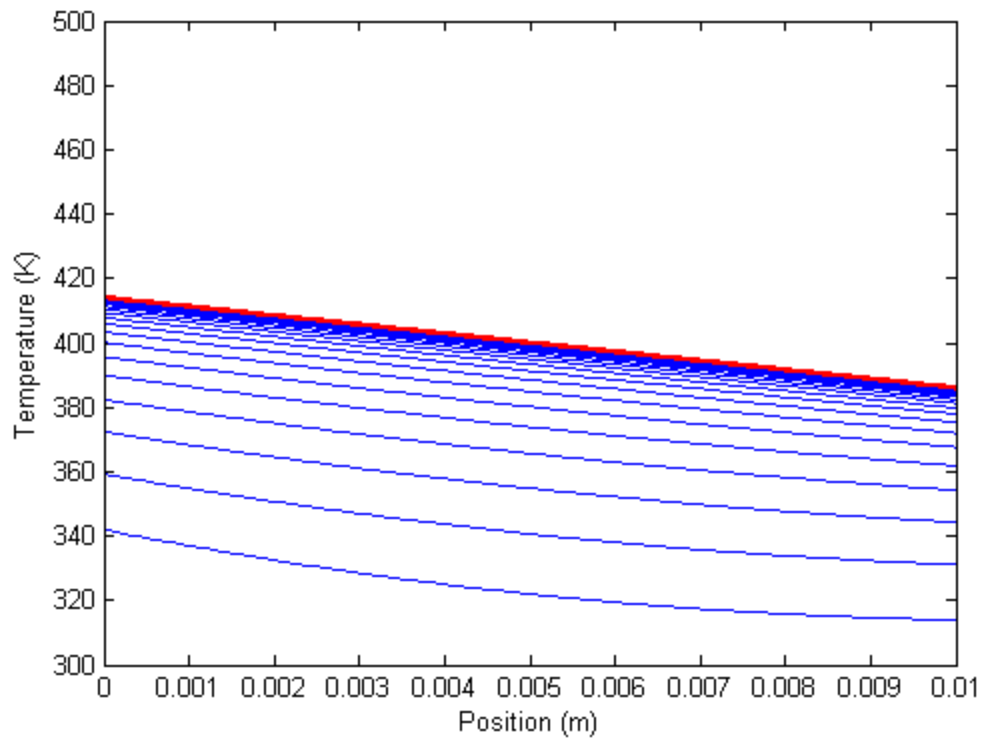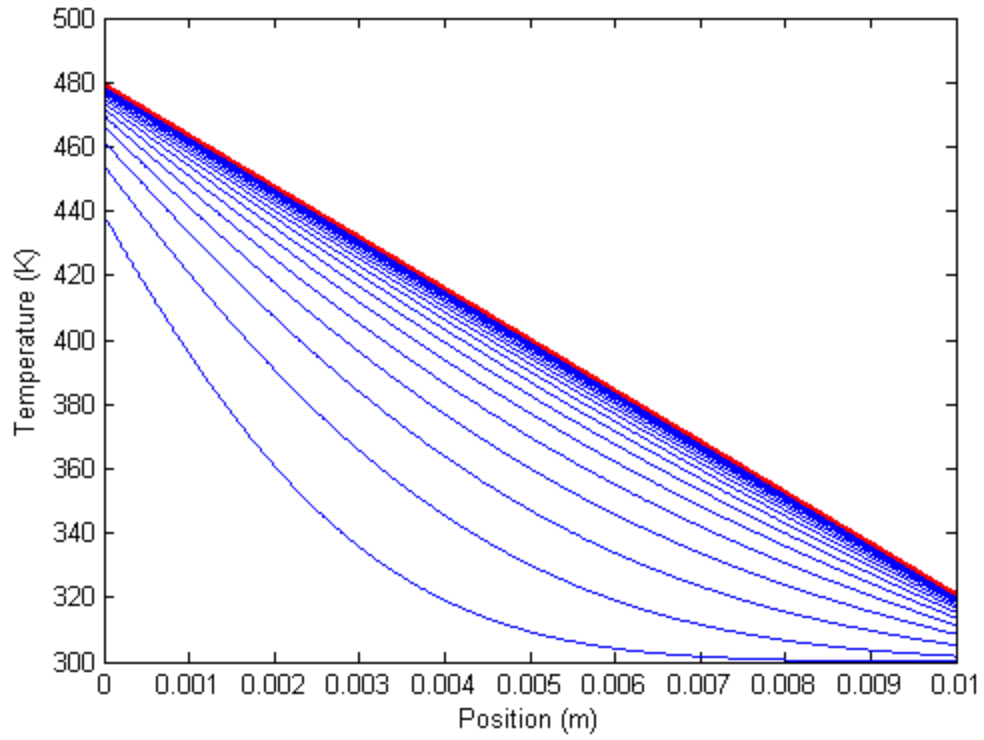
Figure B.1: Comparison between the numerical and analytical steady-state solutions for a system with the thermal properties of air (top) and moisture (bottom)

Though not expressly derived in this analysis, the analytical solution for transient conditions is given by the following expressions [24].

$$erfc(a) = 1 - \frac{2}{\sqrt{\pi}} \int_0^a exp(-b^2) db \qquad (B.13)$$

$$T(x,t) = T_{\infty,\delta} + \left(T_{\infty,1} - T_{\infty,\delta}\right) \left[erfc\left(\frac{x}{2\sqrt{D_{th}t}}\right) \right.$$

$$\left. - exp\left(\frac{h_1 x}{\lambda} + \frac{h_1^2 t}{\lambda \rho c}\right) erfc\left(\frac{x}{2\sqrt{D_{th}t}} + \sqrt{\frac{h_1^2 t}{\lambda \rho c}}\right) \right] \qquad (B.14)$$

It is important to note that this solution is only applicable to systems with approximately infinite thickness in which the propagation of thermal energy through the system is unaffected by the back boundary condition. As a result, this solution is only valid for the system of interest at initial time steps before a temperature-rise is noted at the right system boundary. As with the steady-state solution, the analytical transient solution is evaluated within the previously introduced MATLAB® script with the addition of the following lines of code. The solutions of the numerical approach and the analytical transient expression are compared in **Figure B.2**. As shown in the figure, the blue numerical solutions appropriately match the red analytical solutions for all plotted time steps.

```
%Solve analytical temperature distribution at each time step
Ta = To*ones(nx,nt);
for n = 2:nt
    for i = 1:nx
        Ta(i,n) = TfL+((Tf1-TfL)*((erfc(((i-1)*dx)/(2*((Dth*((n-1)*
        dt))^(1/2)))))-((exp(((h1*((i-1)*dx))/k)+(((h1^2)*((n1)*dt))
        /Ith)))*(erfc((((i-1)*dx)/(2*((Dth*((n-1)*dt))^(1/2))))+((((
        h1^2)*((n-1)*dt))/Ith)^(1/2)))))));
    end
end
```
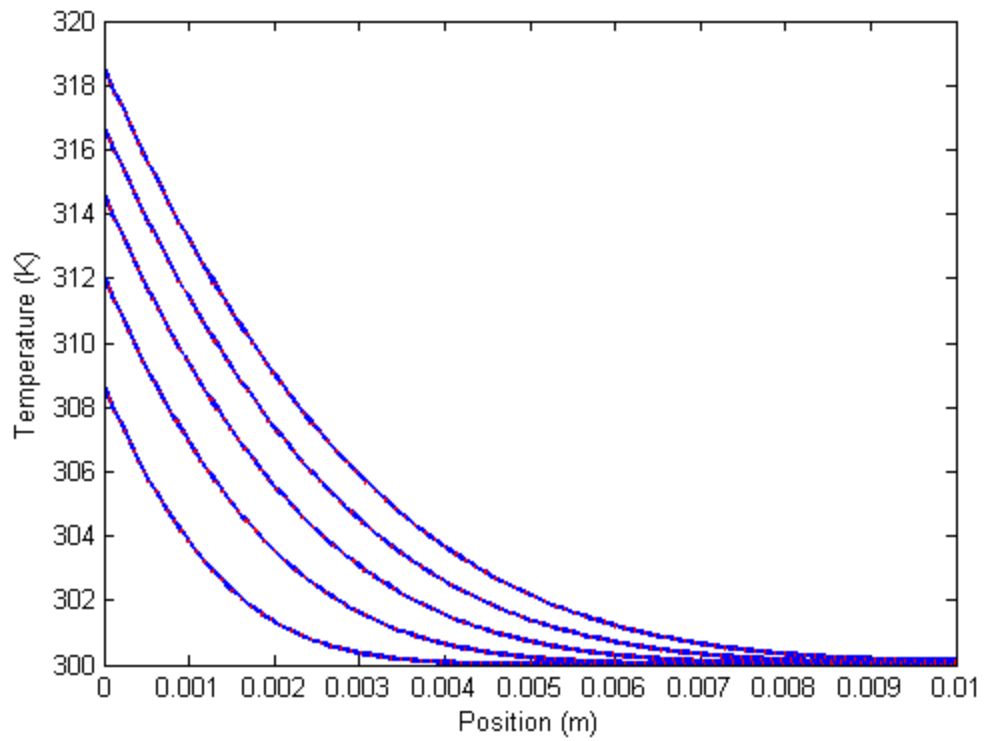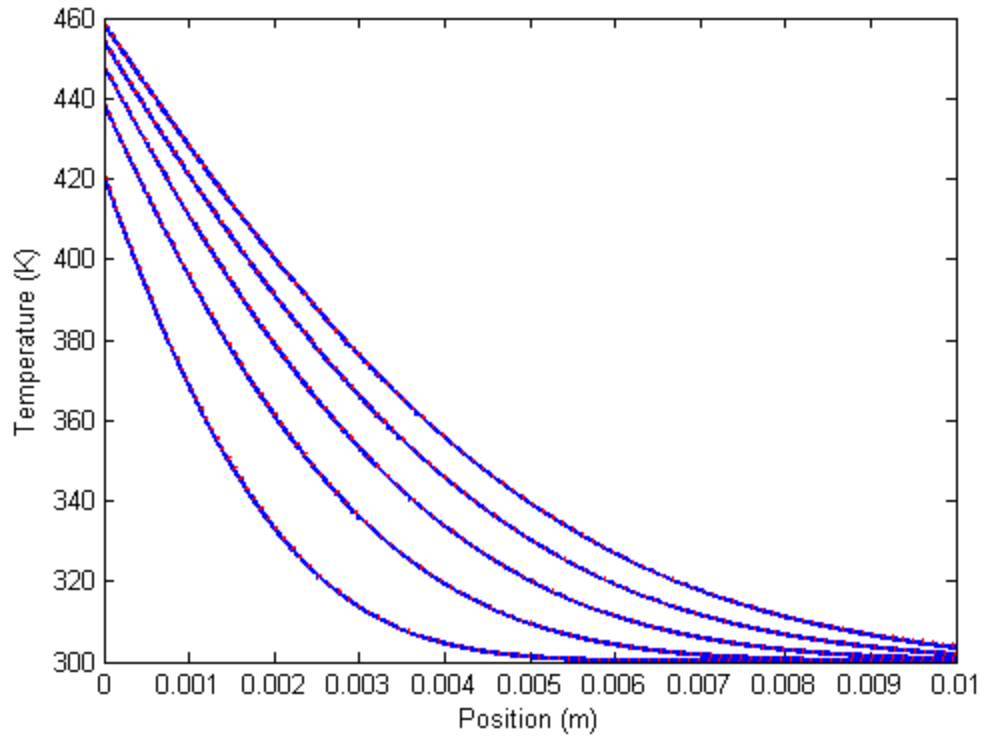
Figure B.2: Comparison between the numerical and analytical transient solutions for a system with the thermal properties of air (top) and moisture (bottom)

The following additional lines of code are used within the previously introduced MATLAB® script to produce the various figures provided in this analysis.

Figure 1.2 and **Figure B.1**:

```
(Air Layer)                              (Moisture Layer)
figure;                                  figure;
hold on                                  hold on
plot(x,T(:,(round(0.2/dt)+1)))           plot(x,T(:,(round(300/dt)+1)))
plot(x,T(:,(round(0.4/dt)+1)))           plot(x,T(:,(round(600/dt)+1)))
plot(x,T(:,(round(0.6/dt)+1)))           plot(x,T(:,(round(900/dt)+1)))
plot(x,T(:,(round(0.8/dt)+1)))           plot(x,T(:,(round(1200/dt)+1)))
plot(x,T(:,(round(1.0/dt)+1)))           plot(x,T(:,(round(1500/dt)+1)))
plot(x,T(:,(round(1.2/dt)+1)))           plot(x,T(:,(round(1800/dt)+1)))
…                                        …
plot(x,T(:,(round(4.4/dt)+1)))           plot(x,T(:,(round(6300/dt)+1)))
plot(x,T(:,(round(4.6/dt)+1)))           plot(x,T(:,(round(6600/dt)+1)))
plot(x,T(:,(round(4.8/dt)+1)))           plot(x,T(:,(round(6900/dt)+1)))
plot(x,T(:,(round(5.0/dt)+1)))           plot(x,T(:,(round(7200/dt)+1)))
plot(x,Ts)                               plot(x,Ts)
```

Figure 1.3:

```
(Both Air and Moisture Layer)
%Solve heat flux at boundary surfaces of slab
q1 = h1.*(Tf1-T(1,:));
qL = hL.*(T(nx,:)-TfL);
figure;
hold on
plot(t,q1)
plot(t,qL)
```

Figure B.2:

```
(Air Layer)                              (Moisture Layer)
figure;                                  figure;
hold on                                  hold on
plot(x,T(:,(round(0.1/dt)+1)))           plot(x,T(:,(round(10/dt)+1)))
plot(x,Ta(:,(round(0.1/dt)+1)))          plot(x,Ta(:,(round(10/dt)+1)))
plot(x,T(:,(round(0.2/dt)+1)))           plot(x,T(:,(round(20/dt)+1)))
plot(x,Ta(:,(round(0.2/dt)+1)))          plot(x,Ta(:,(round(20/dt)+1)))
plot(x,T(:,(round(0.3/dt)+1)))           plot(x,T(:,(round(30/dt)+1)))
plot(x,Ta(:,(round(0.3/dt)+1)))          plot(x,Ta(:,(round(30/dt)+1)))
plot(x,T(:,(round(0.4/dt)+1)))           plot(x,T(:,(round(40/dt)+1)))
plot(x,Ta(:,(round(0.4/dt)+1)))          plot(x,Ta(:,(round(40/dt)+1)))
plot(x,T(:,(round(0.5/dt)+1)))           plot(x,T(:,(round(50/dt)+1)))
plot(x,Ta(:,(round(0.5/dt)+1)))          plot(x,Ta(:,(round(50/dt)+1)))
```

C: Radiant Heat Transfer across an Enclosed Air-Gap

Radiant heat transfer between surfaces is characterized by the conversion of the thermal energy contained within a surface into electromagnetic energy via the vibration and transition of electrons between excited states [6]. This electromagnetic energy radiates from a surface in a particular direction, propagating outward at a characteristic wavelength until it is absorbed, transmitted, or reflected by another surface [6]. Radiant heat transfer exhibits both spectral and directional dependence in that the intensity of the radiant energy emitted by a surface varies with the wavelength of the emitted energy and the direction at which the energy is emitted [6].

A generalized derivation of radiant heat transfer is exceedingly difficult due to these dependencies; therefore, it is typically assumed that radiant heat transfer occurs between gray, diffuse, and opaque surfaces separated by a transparent medium [6]. These assumptions allow the spectral and directional dependencies, the transmittance of a surface, and the dissipation of radiation through a medium to all be neglected. With these simplifications, the interaction of radiant energy with a surface is limited to either absorption or reflection and the participation of the medium is negligible.

The net flux of radiant energy into a surface is characterized by the intensity of the radiant energy incident on the surface less the re-radiation of the surface back to its surroundings. These factors are respectively designated as irradiance and radiosity and are given by the following expressions [6].

$$G = \alpha G + \gamma G + \tau G \qquad (C.1)$$

$$J = \varepsilon \sigma T^4 + \gamma G \qquad (C.2)$$

In equation $(C.1)$, G gives the irradiance on a surface, where α, γ, and τ are respectively the absorptivity, reflectivity, and transmissivity of the surface. These three terms respectively designate the fraction of the incident radiation that is absorbed, reflected, or transmitted by the surface.

In equation $(C.2)$, J gives the radiosity of a surface, where ε is the emissivity of the surface, σ is the Stefan-Boltzmann constant for radiant heat transfer, and T is the absolute temperature of the surface. The first term in this expression designates the fraction of radiosity that is emitted directly by the surface, whereas the second term designates the fraction of radiosity consisting of reflected irradiance.

It should be noted that α, γ, τ, and ε together define the optical properties of a surface and that each are dependent on the direction and wavelength of the radiant energy incident upon the surface and the absolute temperature of the surface. Given the previous assumptions, however, the spectral and directional dependencies of these properties are neglected and transmissivities are assumed zero. For these assumptions, the following simplified statement of Kirchhoff's Law also applies, relating the emissivity and absorptivity of a surface at a specific temperature [6].

$$\varepsilon = \alpha \qquad (C.3)$$

By applying equation $(C.3)$ and the stated assumptions to the previous expressions for irradiance and radiosity given by equations $(C.1)$ and $(C.2)$, the net radiant heat flux incident upon a surface is then given by the following expressions.

$$\dot{q}'' = (G - J) = (\alpha G + \gamma G) - (\varepsilon \sigma T^4 + \gamma G) \qquad (C.4)$$

$$\dot{q}'' = \varepsilon G - \varepsilon \sigma T^4 \qquad (C.5)$$

It is important to note that equation $(C.5)$ is valid only for infinitesimally small surface elements. In extending this expression to radiant heat transfer between finite-size surfaces, it is necessary to introduce geometrical factors defining the orientation of such surfaces with respect to each other.

Radiant heat transfer between finite-size surfaces is characterized by the following expression [6].

$$\dot{q}_{j \rightarrow k} = F_{j \rightarrow k} J_j A_{j \rightarrow k} \qquad (C.6)$$

In this expression, $\dot{q}_{j \rightarrow k}$ gives the rate of radiant heat transfer from surface j to surface k, $F_{j \rightarrow k}$ is a geometrical view factor characterizing the visibility of surface j from surface k, J_j is the radiosity emitted by surface j, and $A_{j \rightarrow k}$ is the area of surface j that is visible to surface k. While view factors are exceedingly difficult to quantify for some geometries, the following pair of relational properties allow them to be determined with relative ease [6].

$$F_{j \rightarrow k} A_{j \rightarrow k} = F_{k \rightarrow j} A_{k \rightarrow j} \qquad (C.7)$$

$$\sum_{k=1}^{N} F_{j \rightarrow k} = 1 \qquad (C.8)$$

Equation $(C.7)$ is a statement of the reciprocity relation, where the view factors between two surfaces are related by the ratio of their visible surface areas. Equation $(C.8)$ is a statement of the summation relation, where the summation of all view factors out of a particular surface must equal unity. This relation simply states that the summation of all fractional radiosities emitted by a surface must equal the total radiosity emitted by that surface.

For a system consisting of a collection of mutually visible radiating surfaces, applying equations $(C.7)$ and $(C.8)$ to equation $(C.6)$ yields the following.

$$G_k A_k = \sum_{j=1}^{N} F_{j \to k} J_j A_{j \to k} = \sum_{j=1}^{N} F_{k \to j} J_j A_{k \to j} \qquad (C.9)$$

$$A_k = \sum_{j=1}^{N} A_{k \to j} \qquad (C.10)$$

$$G_k A_k = A_k \sum_{j=1}^{N} F_{k \to j} J_j \qquad (C.11)$$

$$G_k = \sum_{j=1}^{N} F_{k \to j} J_j \qquad (C.12)$$

In these expressions, G_k gives the total irradiance incident on surface k, A_k is the total surface area of surface k, and the summations are performed over all surfaces visible to surface k. Applying equation $(C.12)$ to equation $(C.5)$ yields the following result.

$$\dot{q}''_k = \varepsilon_k \sum_{j=1}^{N} F_{k \to j} J_j - \varepsilon_k \sigma T_k^4 \qquad (C.13)$$

In this expression, $\dot{q}''_k$ gives the net radiant heat flux incident upon surface k, and ε_k and T_k are respectively the emissivity and absolute temperature of surface k.

For the relevant system of radiant heat transfer between two layers of material separated by an enclosed air-gap, a semi-infinite parallel plate analogy is adopted, allowing the following simplifications to the pertinent view factors. Note that the subscripts 1 and 2 in the following expressions respectively refer to the surfaces on each side of the air-gap.

$$F_{1 \to 1} = F_{2 \to 2} = 0, \qquad F_{1 \to 2} = F_{2 \to 1} = 1 \qquad (C.14, C.15)$$

126

Equations $(C.14)$ and $(C.15)$ utilize the reciprocity and summation relations, through which it is noted that the only surface visible to the surface on one side of the air-gap is the surface on the other side of the air-gap and vice versa. It is also noted that either surface on each side of the air-gap is invisible to itself. Applying equations $(C.14)$ and $(C.15)$ to equation $(C.12)$ yields the following.

$$G_1 = F_{1\to1} J_1 + F_{1\to2} J_2 = J_2 \qquad (C.16)$$

$$G_2 = F_{2\to1} J_1 + F_{2\to2} J_2 = J_1 \qquad (C.17)$$

The application of equations $(C.16)$ and $(C.17)$ to the original radiosity expression provided in equation $(C.2)$ then yields the following.

$$J_1 = \varepsilon_1 \sigma T_1{}^4 + (1 - \varepsilon_1)J_2 \qquad (C.18)$$

$$J_2 = \varepsilon_2 \sigma T_2{}^4 + (1 - \varepsilon_2)J_1 \qquad (C.19)$$

Simultaneous solution of equations $(C.18)$ and $(C.19)$ yields the following.

$$J_1 = \frac{\varepsilon_1 \sigma T_1{}^4 + (1 - \varepsilon_1)\varepsilon_2 \sigma T_2{}^4}{\varepsilon_1 + \varepsilon_2 - \varepsilon_1 \varepsilon_2} \qquad (C.20)$$

$$J_2 = \frac{\varepsilon_2 \sigma T_2{}^4 + (1 - \varepsilon_2)\varepsilon_1 \sigma T_1{}^4}{\varepsilon_1 + \varepsilon_2 - \varepsilon_1 \varepsilon_2} \qquad (C.21)$$

Utilizing these results, the final resulting expressions defining the net radiant heat flux incident upon the surfaces on either side of the air-gap are then as follows.

$$\dot{q}''_1 = \frac{\sigma}{\dfrac{1}{\varepsilon_1} + \dfrac{1}{\varepsilon_2} - 1}(T_2{}^4 - T_1{}^4) \qquad (C.22)$$

$$\dot{q}''_2 = \frac{\sigma}{\dfrac{1}{\varepsilon_1} + \dfrac{1}{\varepsilon_2} - 1}(T_1{}^4 - T_2{}^4) \qquad (C.23)$$

By combining the preceding radiant heat flux expressions given by equations $(C.22)$ and $(C.23)$ with similar expressions for conduction and convection, it is possible to derive an effective thermal conductivity quantifying heat transfer across an air-gap by all three modes of heat transfer. The respective heat fluxes via conduction, convection, and radiation across an air-gap are as follows [6].

$$\dot{q}''_{cond} = \frac{\lambda}{\delta}(T_1 - T_2), \qquad \dot{q}''_{conv} = h(T_1 - T_2) \qquad\qquad (C.24, C.25)$$

$$\dot{q}''_{rad} = \frac{\sigma}{\frac{1}{\varepsilon_1} + \frac{1}{\varepsilon_2} - 1}(T_1{}^4 - T_2{}^4) = \frac{\sigma(T_1{}^2 + T_2{}^2)(T_1 + T_2)}{\frac{1}{\varepsilon_1} + \frac{1}{\varepsilon_2} - 1}(T_1 - T_2) \qquad (C.26)$$

Assuming these three expressions are uncoupled, the effective heat flux across the air-gap, incorporating all three modes of heat transfer, is defined as follows. Note that conductive heat transfer is included as a subset of convective heat transfer. For air-gaps in which convection is negligible, the convective heat transfer coefficient is replaced with the quotient of true thermal conductivity divided by air-gap thickness.

$$\dot{q}''_{eff} = h + \frac{\sigma(T_1{}^2 + T_2{}^2)(T_1 + T_2)}{\frac{1}{\varepsilon_1} + \frac{1}{\varepsilon_2} - 1}(T_1 - T_2) \qquad\qquad (C.27)$$

Rearranging equation $(C.27)$ to reflect the form of equation $(C.24)$ yields the following, where λ_{eff} defines the effective thermal conductivity of the air-gap incorporating heat transfer by all three modes of heat transfer.

$$\dot{q}''_{eff} = \frac{\lambda_{eff}}{\delta}(T_1 - T_2) \qquad\qquad (C.28)$$

$$\lambda_{eff} = \delta h + \frac{\delta\sigma(T_1{}^2 + T_2{}^2)(T_1 + T_2)}{\frac{1}{\varepsilon_1} + \frac{1}{\varepsilon_2} - 1} \qquad\qquad (C.29)$$

Table D.1: Individual layers comprising *C-Liner* variant *Lion* series assemblies

Assembly Designation	Layer		Thickness (mm)	Mass (kg/m^2)
L-CFT	Fusion	Outer Shell	0.381	0.243
	Chambray	Thermal Liner 2	0.229	0.102
	Crosstech	Moisture Barrier	0.381	0.166
	E89 715M	Thermal Liner 1	0.584	0.051
	Glide		0.203	0.122
			1.778	**0.684**

L-CFR	Fusion	Outer Shell	0.381	0.243
	Chambray	Thermal Liner 2	0.229	0.102
	RT-7100	Moisture Barrier	0.762	0.156
	E89 715M	Thermal Liner 1	0.584	0.051
	Glide		0.203	0.122
			2.159	**0.674**

L-CPT	PBI Matrix	Outer Shell	0.406	0.247
	Chambray	Thermal Liner 2	0.229	0.102
	Crosstech	Moisture Barrier	0.381	0.166
	E89 715M	Thermal Liner 1	0.584	0.051
	Glide		0.203	0.122
			1.803	**0.688**

L-CPR	PBI Matrix	Outer Shell	0.406	0.247
	Chambray	Thermal Liner 2	0.229	0.102
	RT-7100	Moisture Barrier	0.762	0.156
	E89 715M	Thermal Liner 1	0.584	0.051
	Glide		0.203	0.122
			2.184	**0.678**

Table D.2: Individual layers comprising *K-Liner* variant *Lion* series assemblies

Assembly Designation	Layer		Thickness (mm)	Mass (kg/m^2)
L-KFT	*Fusion*	*Outer Shell*	0.381	0.243
	Crosstech	*Moisture Barrier*	0.381	0.166
	E89 715M	*Thermal Liner*	0.584	0.051
	E89 723DWR		0.686	0.078
	Glide		0.203	0.122
			2.235	**0.660**

L-KFR	*Fusion*	*Outer Shell*	0.381	0.243
	RT-7100	*Moisture Barrier*	0.762	0.156
	E89 715M	*Thermal Liner*	0.584	0.051
	E89 723DWR		0.686	0.078
	Glide		0.203	0.122
			2.616	**0.650**

L-KPT	*PBI Matrix*	*Outer Shell*	0.406	0.247
	Crosstech	*Moisture Barrier*	0.381	0.166
	E89 715M	*Thermal Liner*	0.584	0.051
	E89 723DWR		0.686	0.078
	Glide		0.203	0.122
			2.260	**0.664**

L-KPR	*PBI Matrix*	*Outer Shell*	0.406	0.247
	RT-7100	*Moisture Barrier*	0.762	0.156
	E89 715M	*Thermal Liner*	0.584	0.051
	E89 723DWR		0.686	0.078
	Glide		0.203	0.122
			2.641	**0.654**

Table D.3: Individual layers comprising *Semper-Dri* variant *Lion* series assemblies

Assembly Designation	Layer		Thickness (mm)	Mass (kg/m^2)
L-SFT	*Fusion*	*Outer Shell*	0.381	0.243
	Crosstech	*Moisture Barrier*	0.381	0.166
	E89 715M	*Thermal Liner*	0.584	0.051
	E89 723DWR		0.686	0.078
	Chambray		0.229	0.102
			2.261	**0.640**

Assembly Designation	Layer		Thickness (mm)	Mass (kg/m^2)
L-SFR	*Fusion*	*Outer Shell*	0.381	0.243
	RT-7100	*Moisture Barrier*	0.762	0.156
	E89 715M	*Thermal Liner*	0.584	0.051
	E89 723DWR		0.686	0.078
	Chambray		0.229	0.102
			2.642	**0.630**

Assembly Designation	Layer		Thickness (mm)	Mass (kg/m^2)
L-SPT	*PBI Matrix*	*Outer Shell*	0.406	0.247
	Crosstech	*Moisture Barrier*	0.381	0.166
	E89 715M	*Thermal Liner*	0.584	0.051
	E89 723DWR		0.686	0.078
	Chambray		0.229	0.102
			2.286	**0.644**

Assembly Designation	Layer		Thickness (mm)	Mass (kg/m^2)
L-SPR	*PBI Matrix*	*Outer Shell*	0.406	0.247
	RT-7100	*Moisture Barrier*	0.762	0.156
	E89 715M	*Thermal Liner*	0.584	0.051
	E89 723DWR		0.686	0.078
	Chambray		0.229	0.102
			2.667	**0.634**

Table D.4: Individual layers comprising *V-Caldura* variant *Lion* series assemblies

Assembly Designation	Layer		Thickness (mm)	Mass (kg/m^2)
L-VFT	*Fusion*	*Outer Shell*	0.381	0.243
	Crosstech	*Moisture Barrier*	0.381	0.166
	E89 723DWR		0.686	0.078
	E89 723DWR	*Thermal Liner*	0.686	0.078
	Glide		0.203	0.122
			2.337	**0.687**

Assembly Designation	Layer		Thickness (mm)	Mass (kg/m^2)
L-VFR	*Fusion*	*Outer Shell*	0.381	0.243
	RT-7100	*Moisture Barrier*	0.762	0.156
	E89 723DWR		0.686	0.078
	E89 723DWR	*Thermal Liner*	0.686	0.078
	Glide		0.203	0.122
			2.718	**0.677**

Assembly Designation	Layer		Thickness (mm)	Mass (kg/m^2)
L-VPT	*PBI Matrix*	*Outer Shell*	0.406	0.247
	Crosstech	*Moisture Barrier*	0.381	0.166
	E89 723DWR		0.686	0.078
	E89 723DWR	*Thermal Liner*	0.686	0.078
	Glide		0.203	0.122
			2.362	**0.691**

Assembly Designation	Layer		Thickness (mm)	Mass (kg/m^2)
L-VPR	*PBI Matrix*	*Outer Shell*	0.406	0.247
	RT-7100	*Moisture Barrier*	0.762	0.156
	E89 723DWR		0.686	0.078
	E89 723DWR	*Thermal Liner*	0.686	0.078
	Glide		0.203	0.122
			2.743	**0.681**

Table D.5: Individual layers comprising *X-Liner* variant *Lion* series assemblies

Assembly Designation	Layer		Thickness (mm)	Mass (kg/m^2)
L-XFT	Fusion	Outer Shell	0.381	0.243
	Chambray	Thermal Liner 2	0.229	0.102
	E89 715M		0.584	0.051
	Crosstech	Moisture Barrier	0.381	0.166
	E89 715M	Thermal Liner 1	0.584	0.051
	Glide		0.203	0.122
			2.362	**0.735**

Assembly Designation	Layer		Thickness (mm)	Mass (kg/m^2)
L-XFR	Fusion	Outer Shell	0.381	0.243
	Chambray	Thermal Liner 2	0.229	0.102
	E89 715M		0.584	0.051
	RT-7100	Moisture Barrier	0.762	0.156
	E89 715M	Thermal Liner 1	0.584	0.051
	Glide		0.203	0.122
			2.743	**0.725**

Assembly Designation	Layer		Thickness (mm)	Mass (kg/m^2)
L-XPT	PBI Matrix	Outer Shell	0.406	0.247
	Chambray	Thermal Liner 2	0.229	0.102
	E89 715M		0.584	0.051
	Crosstech	Moisture Barrier	0.381	0.166
	E89 715M	Thermal Liner 1	0.584	0.051
	Glide		0.203	0.122
			2.387	**0.739**

Assembly Designation	Layer		Thickness (mm)	Mass (kg/m^2)
L-XPR	PBI Matrix	Outer Shell	0.406	0.247
	Chambray	Thermal Liner 2	0.229	0.102
	E89 715M		0.584	0.051
	RT-7100	Moisture Barrier	0.762	0.156
	E89 715M	Thermal Liner 1	0.584	0.051
	Glide		0.203	0.122
			2.768	**0.729**

Table D.6: Individual layers comprising *Static Air-Gap* series assemblies

Assembly Designation	Layer		Thickness (mm)	Mass (kg/m^2)
A-0	*Fusion*	*Outer Shell*	0.381	0.243
	Fusion	*Layer 3*	0.381	0.243
	–	*Air Gap*	–	–
	Fusion	*Layer 2*	0.381	0.243
	Fusion	*Layer 1*	0.381	0.243
			1.524	**0.972**

Assembly Designation	Layer		Thickness (mm)	Mass (kg/m^2)
A-1	*Fusion*	*Outer Shell*	0.381	0.243
	Fusion	*Layer 3*	0.381	0.243
	Static Frame	*Air Gap*	7.000	0.008
	Fusion	*Layer 2*	0.381	0.243
	Fusion	*Layer 1*	0.381	0.243
			8.524	**0.980**

Assembly Designation	Layer		Thickness (mm)	Mass (kg/m^2)
A-2	*Fusion*	*Outer Shell*	0.381	0.243
	Fusion	*Layer 3*	0.381	0.243
	Static Frame	*Air Gap*	7.000	0.008
	Static Frame		7.000	0.008
	Fusion	*Layer 2*	0.381	0.243
	Fusion	*Layer 1*	0.381	0.243
			15.524	**0.988**

Assembly Designation	Layer		Thickness (mm)	Mass (kg/m^2)
A-4	*Fusion*	*Outer Shell*	0.381	0.243
	Fusion	*Layer 3*	0.381	0.243
	Static Frame	*Air Gap*	7.000	0.008
	Static Frame		7.000	0.008
	Static Frame		7.000	0.008
	Static Frame		7.000	0.008
	Fusion	*Layer 2*	0.381	0.243
	Fusion	*Layer 1*	0.381	0.243
			29.524	**1.004**

Table D.7: Individual layers comprising *Moisture* series assemblies

Assembly Designation	Layer		Thickness (*mm*)	Mass (*kg/m²*)
M_s-D M_s-W	*PBI Matrix*	*Outer Shell*	0.406	0.247
	Glide	*Thermal Liner 2*	0.203	0.122
	E89 723DWR		0.686	0.078
	E89 723DWR		0.686	0.078
	RT-7100	*Moisture Barrier*	0.762	0.156
	E89 723DWR	*Thermal Liner 1*	0.686	0.078
	E89 723DWR		0.686	0.078
	Glide		0.203	0.122
			4.318	**0.959**

M_t-D M_t-W	*PBI Matrix*	*Outer Shell*	0.406	0.247
	RT-7100	*Moisture Barrier*	0.762	0.156
	Glide	*Thermal Liner 2*	0.203	0.122
	E89 723DWR		0.686	0.078
	E89 723DWR		0.686	0.078
	E89 723DWR	*Thermal Liner 1*	0.686	0.078
	E89 723DWR		0.686	0.078
	Glide		0.203	0.122
			4.318	**0.959**

Table D.8: Individual layers comprising *Expanding Air-Gap* series assemblies

Assembly Designation	Layer		Thickness (mm)	Mass (kg/m^2)
E_o-Ø	*PBI Matrix*	*Outer Shell*	0.406	0.247
	Chambray	*SMR Assembly*	0.229	0.102
	Chambray		0.229	0.102
	Crosstech	*Moisture Barrier*	0.381	0.166
	E89 715M	*Thermal Liner*	0.584	0.051
	Glide		0.203	0.122
			2.032	**0.790**

Assembly Designation	Layer		Thickness (mm)	Mass (kg/m^2)
E_i-Ø	*PBI Matrix*	*Outer Shell*	0.406	0.247
	Glide	*Thermal Liner*	0.203	0.122
	E89 715M		0.584	0.051
	Crosstech	*Moisture Barrier*	0.381	0.166
	Chambray	*SMR Assembly*	0.229	0.102
	Chambray		0.229	0.102
			2.032	**0.790**

Assembly Designation	Layer		Thickness (mm)	Mass (kg/m^2)
E_o-50 E_o-90	*PBI Matrix*	*Outer Shell*	0.406	0.247
	Chambray	*SMR Assembly*	0.229	0.102
	SMR		−	0.133
	Chambray		0.229	0.102
	Crosstech	*Moisture Barrier*	0.381	0.166
	E89 715M	*Thermal Liner*	0.584	0.051
	Glide		0.203	0.122
			2.032	**0.923**

Assembly Designation	Layer		Thickness (mm)	Mass (kg/m^2)
E_i-50 E_i-90	*PBI Matrix*	*Outer Shell*	0.406	0.247
	Glide	*Thermal Liner*	0.203	0.122
	E89 715M		0.584	0.051
	Crosstech	*Moisture Barrier*	0.381	0.166
	Chambray	*SMR Assembly*	0.229	0.102
	SMR		−	0.133
	Chambray		0.229	0.102
			2.032	**0.923**

E: Derivation of Uncertainty Expressions

The expressions used to calculate the uncertainties associated with the average temperature measurements, NTR parameters, and NTG parameters are derived as follows. The mean and standard deviation characterizing a set of measured quantities are first defined by the following expressions [22].

$$\bar{a} = \frac{1}{N} \sum_{j=1}^{N} a_j \qquad (E.1)$$

$$S_a = \sqrt{\frac{1}{(N-1)} \sum_{j=1}^{N} (a_j - \bar{a})^2} \qquad (E.2)$$

In these expressions, $\bar{a}$ and S_a respectively give the mean and standard deviation characterizing a set of quantities, a_j is the value of a particular quantity within the set, and N is the number of quantities within the set.

Considering a value of interest that is a function of some number of measurable quantities, such a value can be expressed as follows.

$$\varphi = f(a, b, \cdots) \qquad (E.3)$$

In this expression, φ gives the value of interest, a and b are measureable quantities with known uncertainties, and f is a function relating the value of interest to the measurable quantities. The standard deviation of the value of interest is then a function of the standard deviations of each measureable quantity and is given by the following expression [22].

$$S_\varphi = \sqrt{S_a^2 \left(\frac{\partial f(a,b)}{\partial a}\right)^2 + S_b^2 \left(\frac{\partial f(a,b)}{\partial b}\right)^2 + \cdots} \qquad (E.4)$$

In equation $(E.4)$, S_φ gives the standard deviation of the value of interest, S_a is the standard deviation of quantity a, and S_b is the standard deviation of quantity b. Utilizing equation $(E.1)$ as the function, f, within equation $(E.4)$ then allows the determination of the standard deviation of the mean for a set of measured quantities.

$$S_{\bar{a}} = \sqrt{\sum_{j=1}^{N}\left(S_a{}^2\left(\frac{\partial}{\partial a_j}\left(\frac{1}{N}\sum_{j=1}^{N}a_j\right)\right)^2\right)} \qquad (E.5)$$

$$S_{\bar{a}} = \sqrt{\frac{1}{N(N-1)}\sum_{j=1}^{N}(a_j - \bar{a})^2} \qquad (E.6)$$

Note that equation $(E.6)$ defines the uncertainty associated with a set of average temperature measurements where the arbitrary quantity, a, is replaced with a set of measured temperatures. The uncertainties associated with NTR and NTG parameters are similarly determined as follows. Note that the functions defining NTR and NTG parameters, as defined by equations (2.2) and (2.3), both take the same form. It is therefore worthwhile to derive a generalized uncertainty expression applicable to both NTR and NTG parameters and subsequently apply the specific measurements characteristic of each parameter to the resulting expression.

The expressions relating NTR and NTG parameters to measureable temperature quantities both take the following form.

$$\varphi = \frac{T_1 - T_2}{T_3 - T_4} \qquad (E.7)$$

In this expression, φ represents either the NTR or NTG parameter and T_1, T_2, T_3, and T_4 each represent the temperature measurements defining either parameter.

By utilizing equation $(E.7)$ as the function, f, within equation $(E.4)$, the generalized uncertainty expression for either parameter is derived as follows.

$$S_\varphi = \sqrt{S_{T_1}^2 \left(\frac{\partial \varphi}{\partial T_1}\right)^2 + S_{T_2}^2 \left(\frac{\partial \varphi}{\partial T_2}\right)^2 + S_{T_3}^2 \left(\frac{\partial \varphi}{\partial T_3}\right)^2 + S_{T_4}^2 \left(\frac{\partial \varphi}{\partial T_4}\right)^2} \qquad (E.8)$$

$$\left(\frac{\partial \varphi}{\partial T_1}\right)^2 = \left(\frac{T_3 - T_4}{(T_3 - T_4)^2}\right)^2 = \frac{1}{(T_3 - T_4)^2} \qquad (E.9)$$

$$\left(\frac{\partial \varphi}{\partial T_2}\right)^2 = \left(\frac{-(T_3 - T_4)}{(T_3 - T_4)^2}\right)^2 = \frac{1}{(T_3 - T_4)^2} \qquad (E.10)$$

$$\left(\frac{\partial \varphi}{\partial T_3}\right)^2 = \left(\frac{-(T_1 - T_2)}{(T_3 - T_4)^2}\right)^2 = \frac{(T_1 - T_2)^2}{(T_3 - T_4)^4} \qquad (E.11)$$

$$\left(\frac{\partial \varphi}{\partial T_4}\right)^2 = \left(\frac{T_1 - T_2}{(T_3 - T_4)^2}\right)^2 = \frac{(T_1 - T_2)^2}{(T_3 - T_4)^4} \qquad (E.12)$$

$$S_\varphi = \sqrt{\frac{S_{T_1}^2}{(T_3 - T_4)^2} + \frac{S_{T_2}^2}{(T_3 - T_4)^2} + S_{T_3}^2 \frac{(T_1 - T_2)^2}{(T_3 - T_4)^4} + S_{T_4}^2 \frac{(T_1 - T_2)^2}{(T_3 - T_4)^4}} \qquad (E.13)$$

Applying the specific temperature measurements characteristic of each parameter to equation $(E.13)$ then yields the following final uncertainty expressions.

$$S_{NTR_j^n}$$

$$= \sqrt{\frac{S_{T_j^n}^2}{(T_{os}^n - T_{os}^0)^2} + \frac{S_{T_j^0}^2}{(T_{os}^n - T_{os}^0)^2} + S_{T_{os}^n}^2 \frac{\left(T_j^n - T_j^0\right)^2}{(T_{os}^n - T_{os}^0)^4} + S_{T_{os}^0}^2 \frac{\left(T_j^n - T_j^0\right)^2}{(T_{os}^n - T_{os}^0)^4}} \qquad (E.14)$$

$$S_{NTG_j^n}$$

$$= \sqrt{\frac{S_{T_j^n}^2}{\left(T_{os}^n - T_{bp}^n\right)^2} + \frac{S_{T_{j-1}^n}^2}{\left(T_{os}^n - T_{bp}^n\right)^2} + S_{T_{os}^n}^2 \frac{\left(T_j^n - T_{j-1}^n\right)^2}{\left(T_{os}^n - T_{bp}^n\right)^4} + S_{T_{bp}^n}^2 \frac{\left(T_j^n - T_{j-1}^n\right)^2}{\left(T_{os}^n - T_{bp}^n\right)^4}} \qquad (E.15)$$
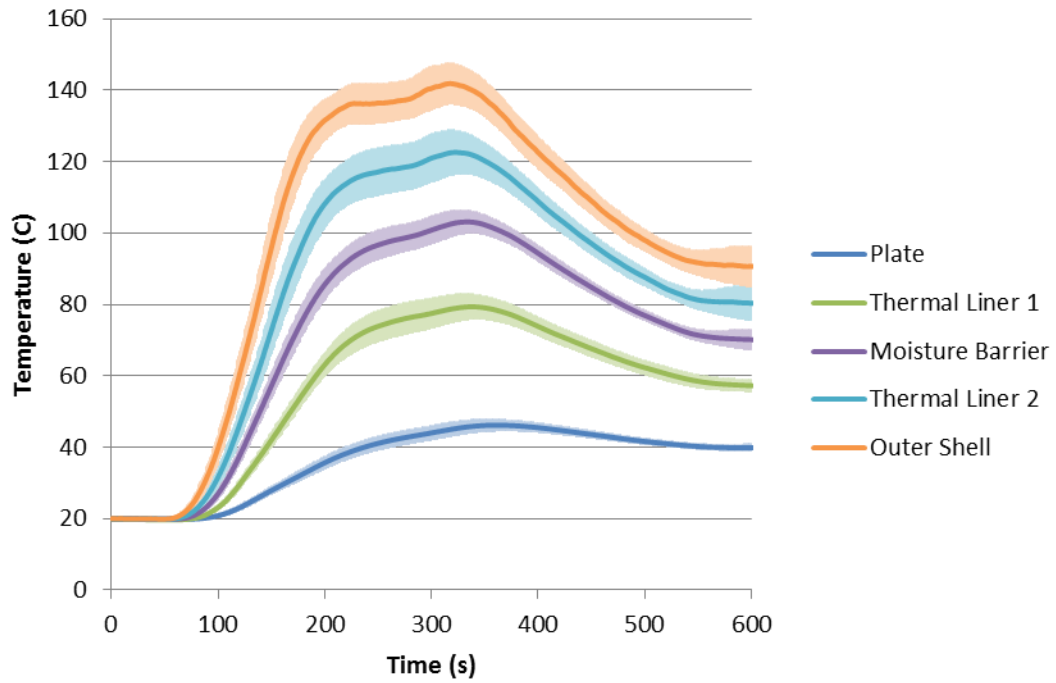
Figure F.1: Time evolution of individual layer temperatures for assembly *L-C*
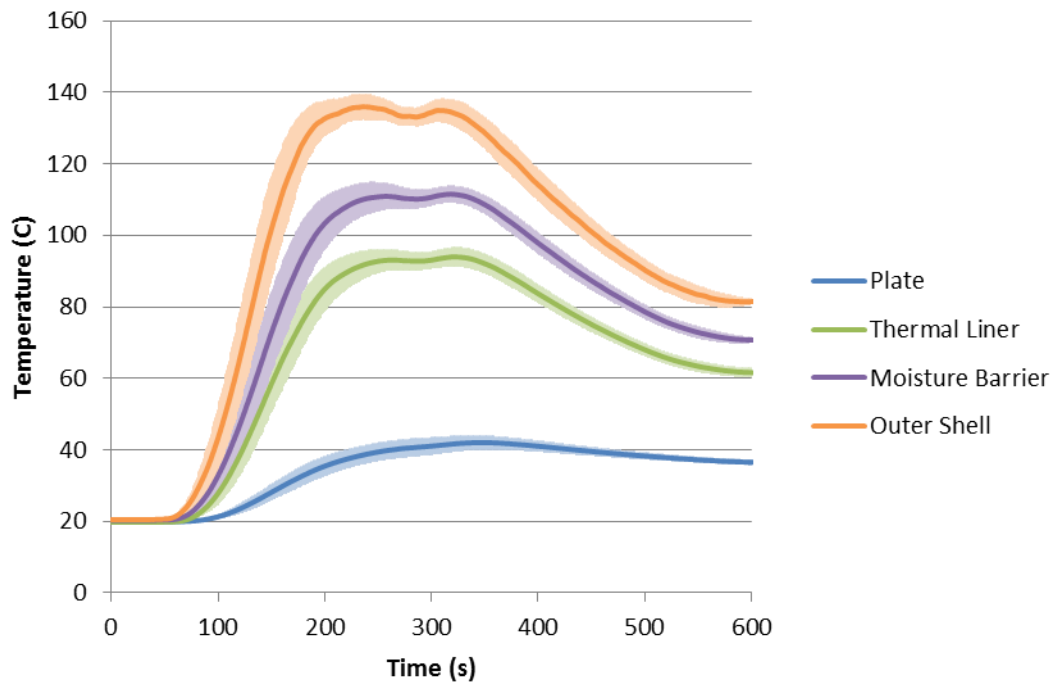
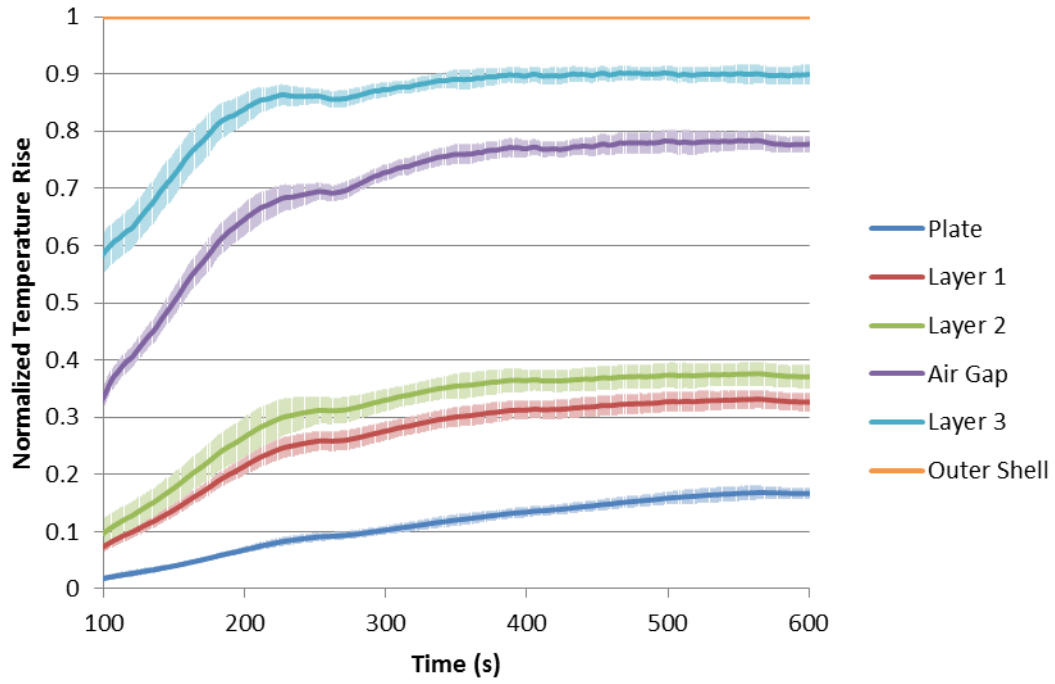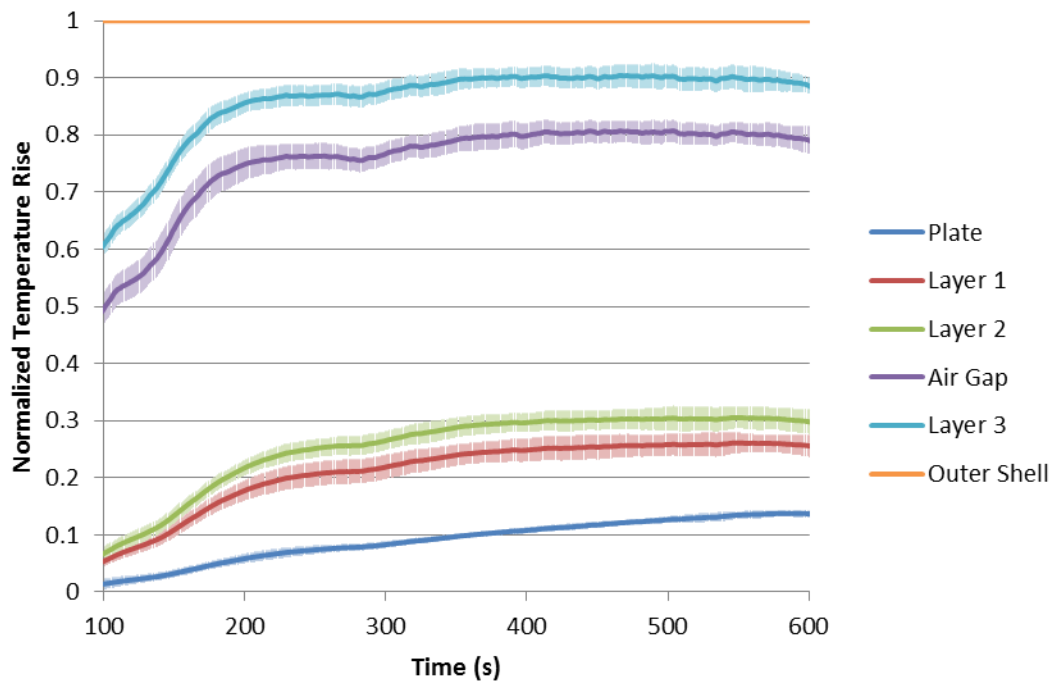**Figure F.2**: Time evolution of individual layer temperatures for assembly *L-K*
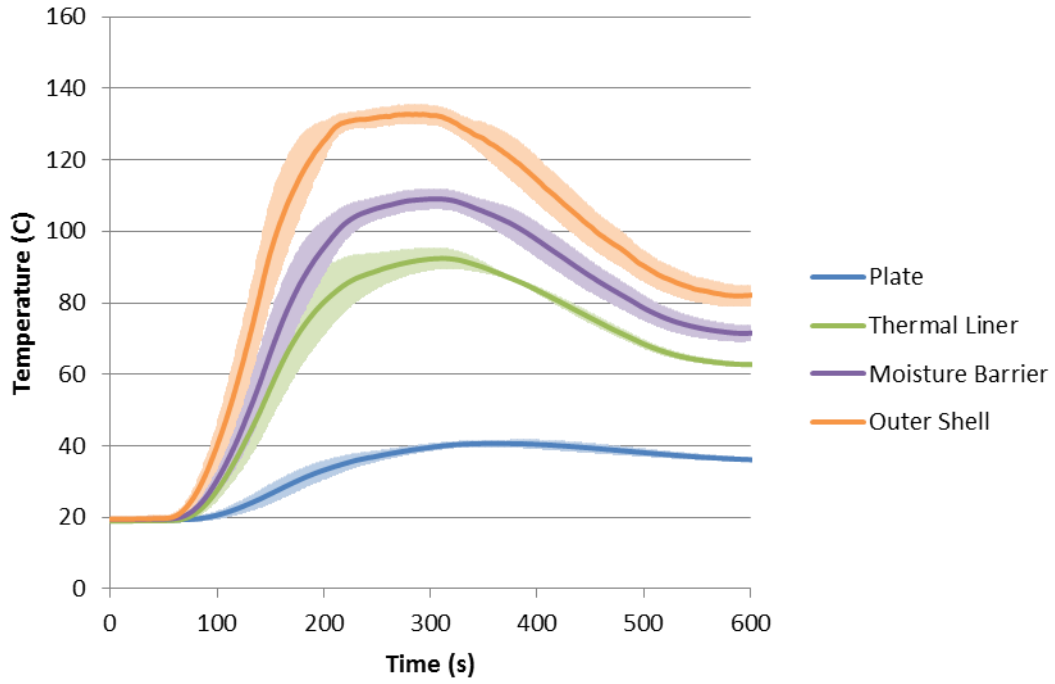
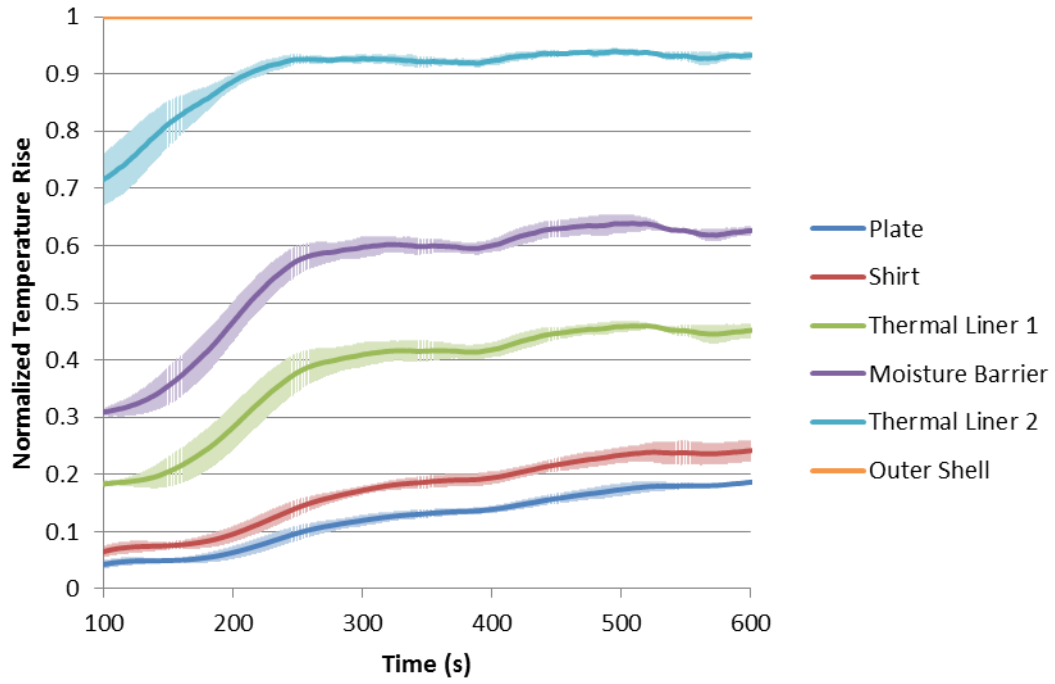**Figure F.3**: Time evolution of individual layer temperatures for assembly *L-S*
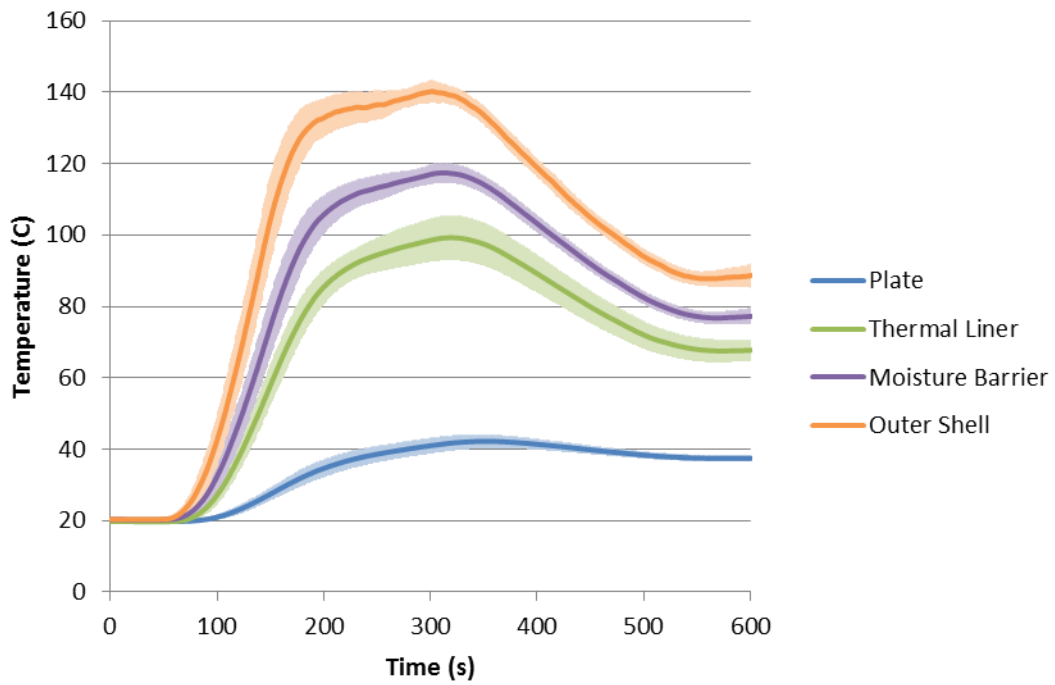
Figure F.4: Time evolution of individual layer temperatures for assembly *L-V*
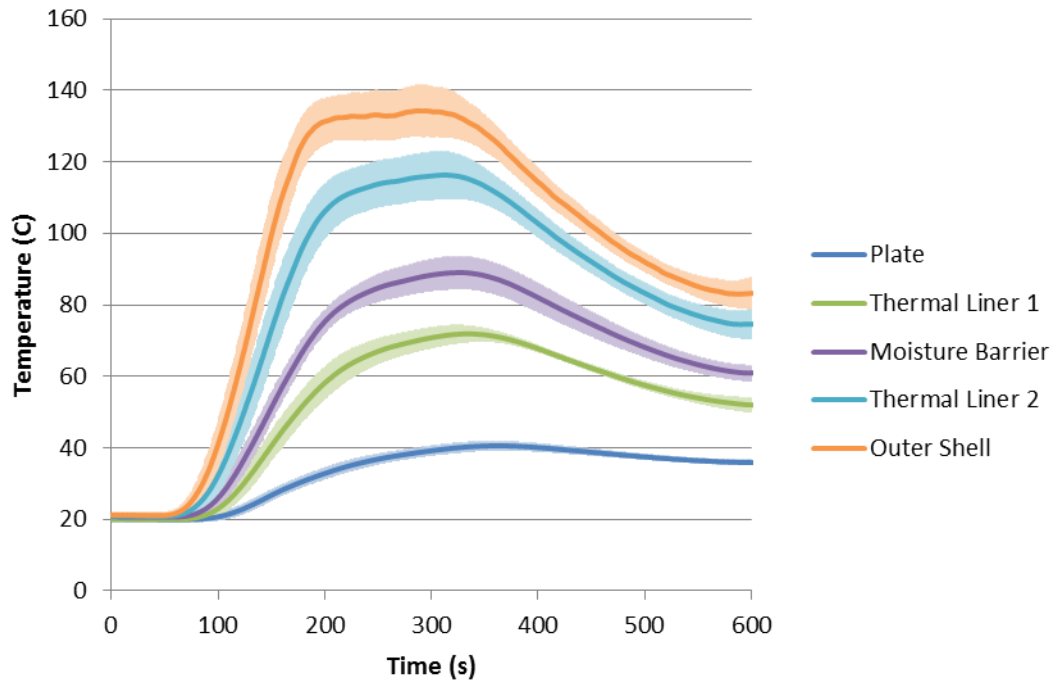
Figure F.5: Time evolution of individual layer temperatures for assembly *L-X*

Space Intentionally Left Blank
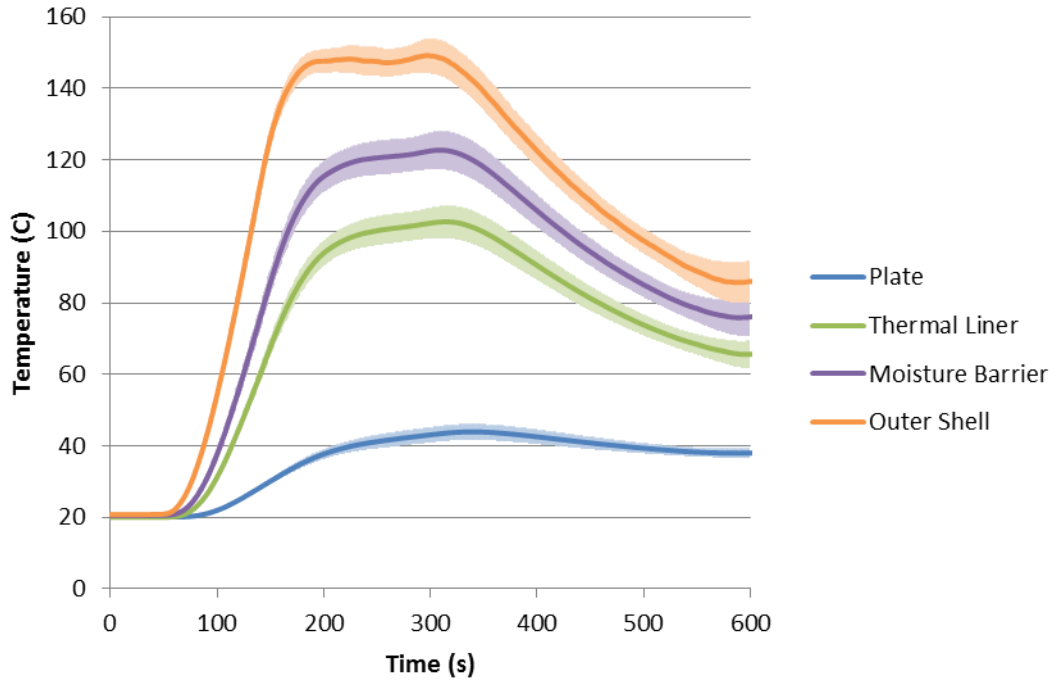
Figure F.6: Time evolution of individual layer temperatures for assembly *L-F*
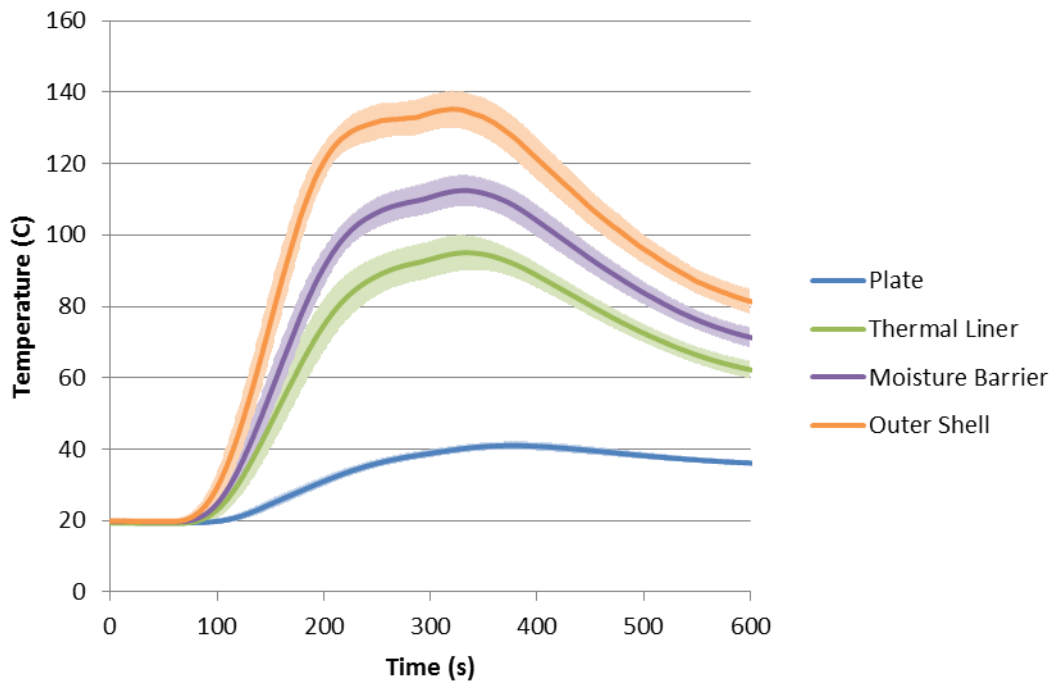
Figure F.7: Time evolution of individual layer temperatures for assembly *L-P*
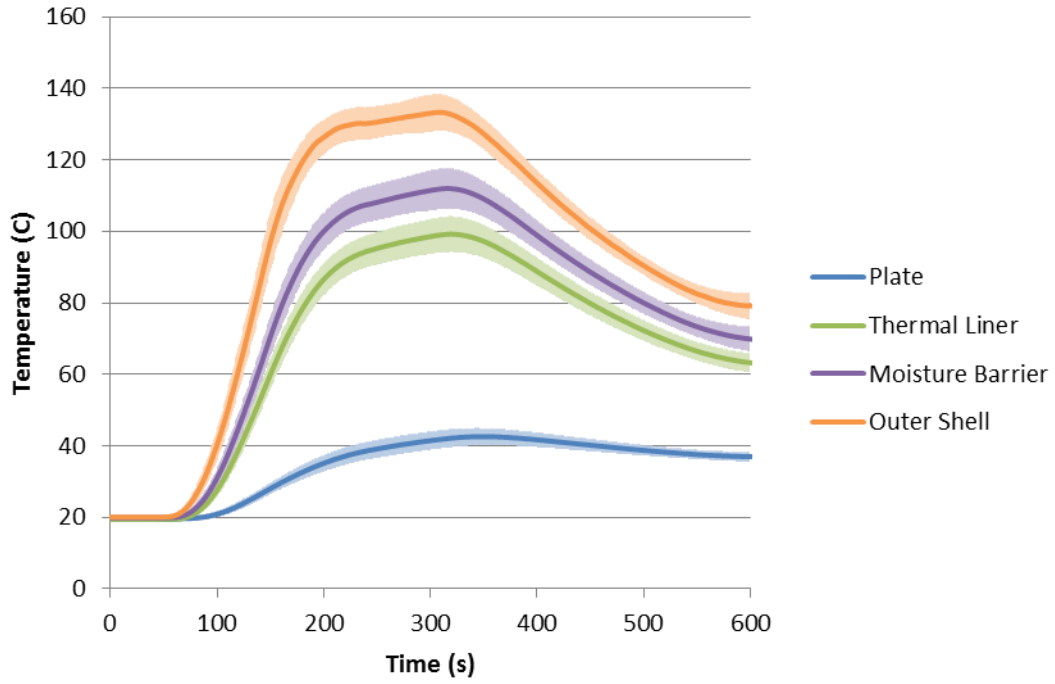
Figure F.8: Time evolution of individual layer temperatures for assembly *L-T*
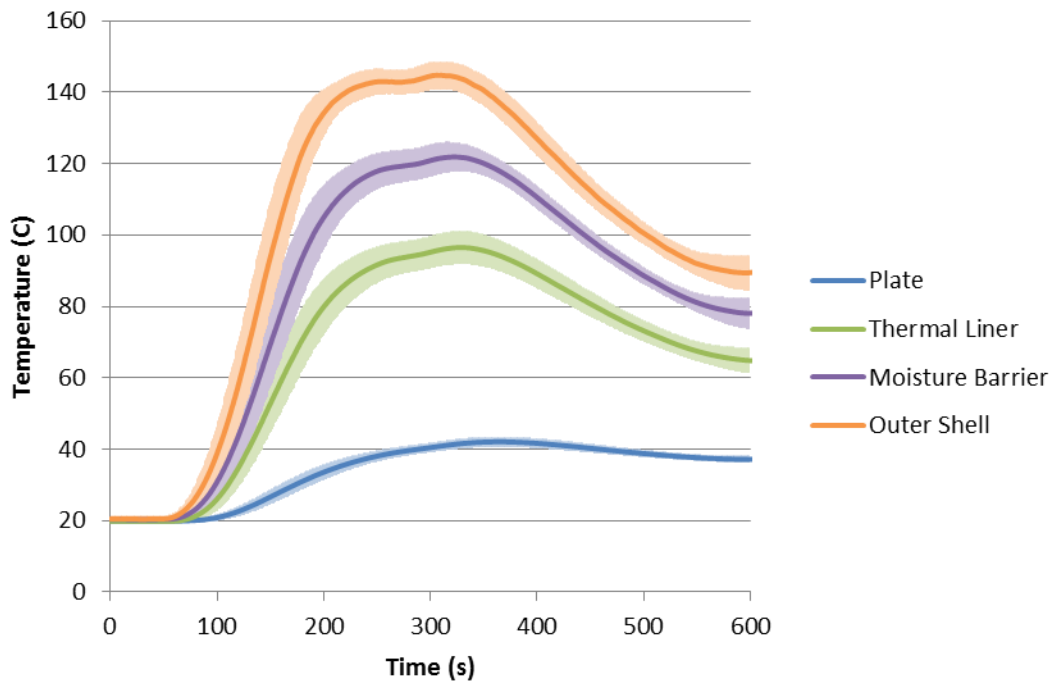
Figure F.9: Time evolution of individual layer temperatures for assembly *L-R*
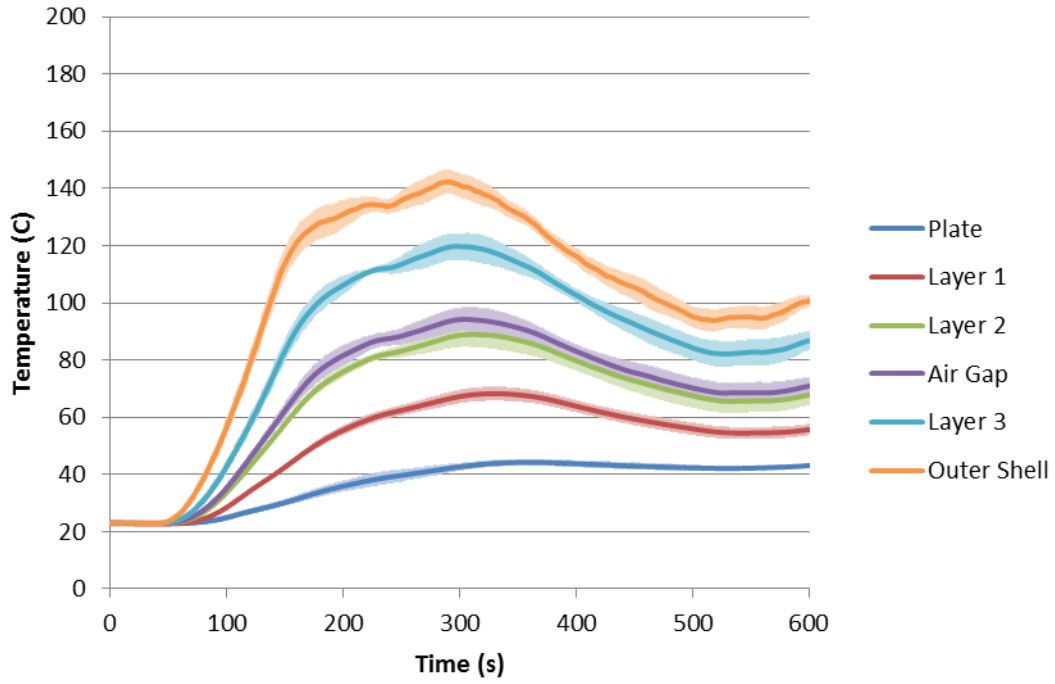
Figure F.10: Time evolution of individual layer temperatures for assembly *A*-0
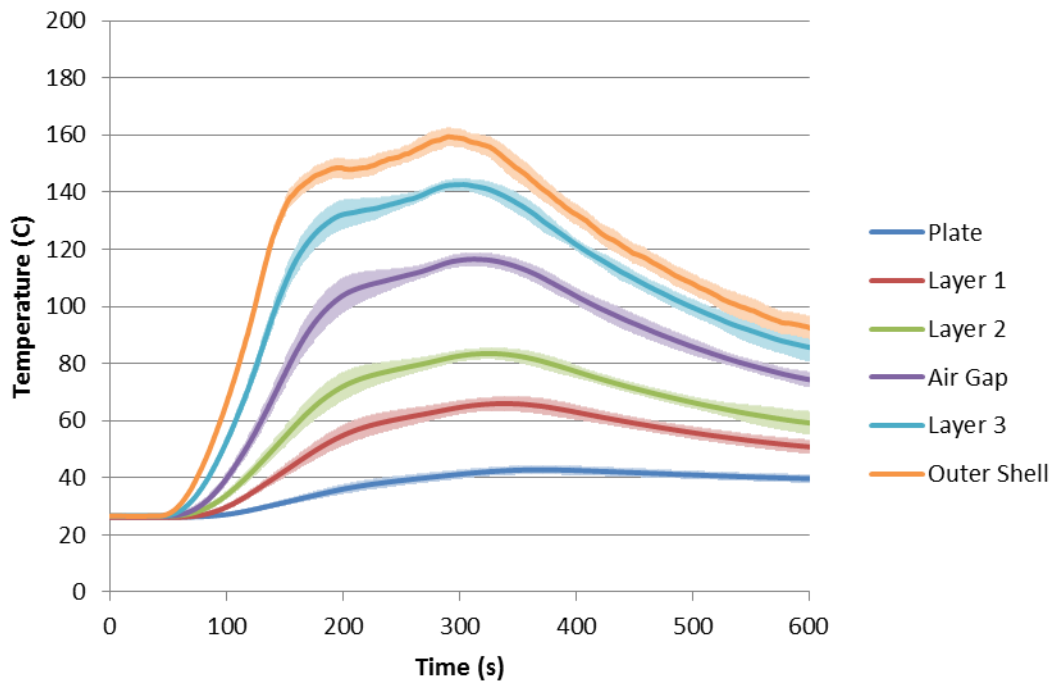
Figure F.11: Time evolution of individual layer temperatures for assembly *A*-1
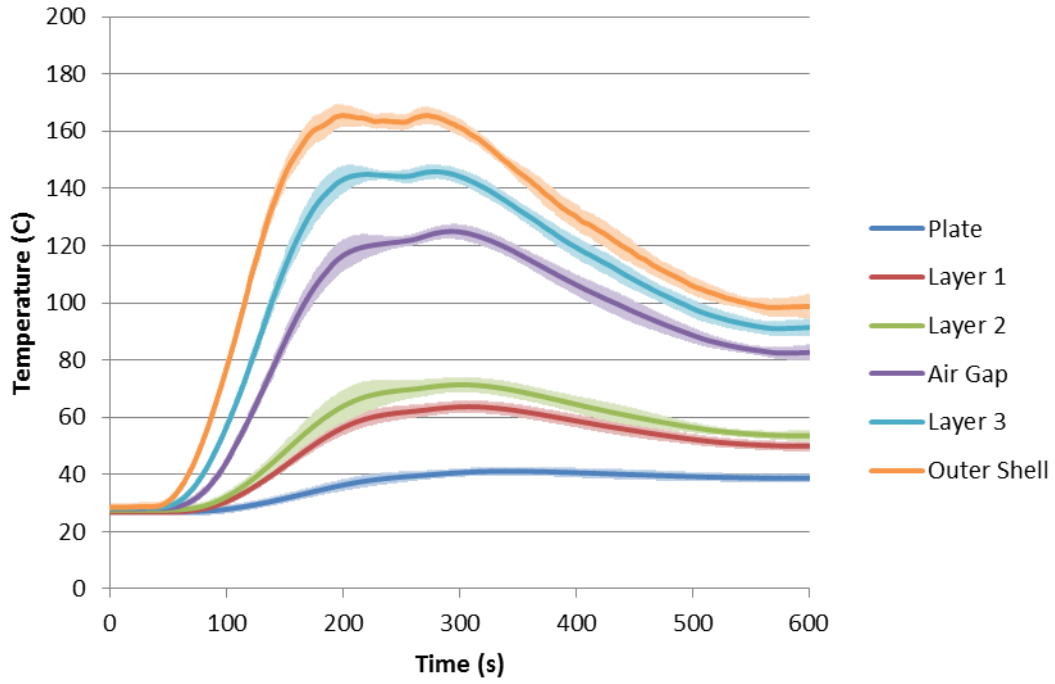
Figure F.12: Time evolution of individual layer temperatures for assembly *A*-2
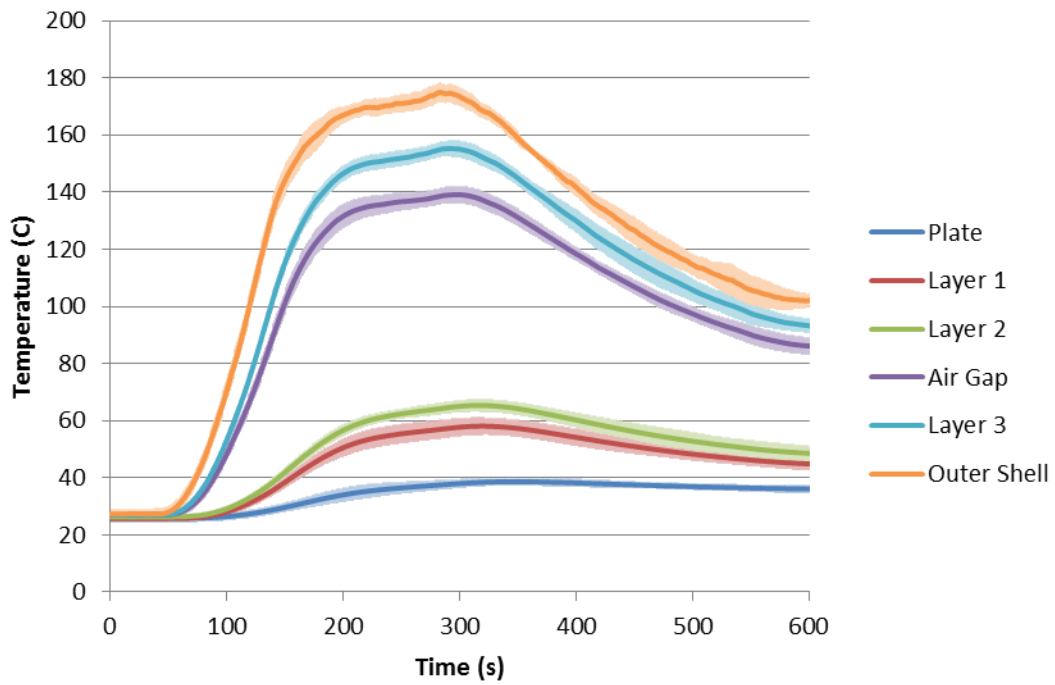
Figure F.13: Time evolution of individual layer temperatures for assembly *A*-4

146
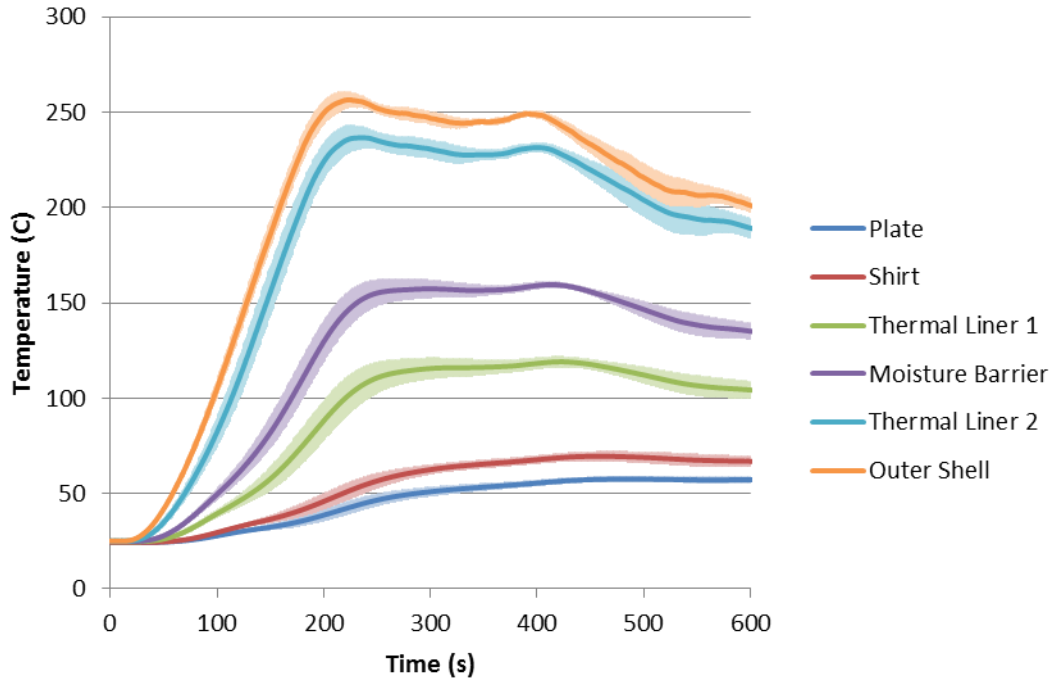
Figure F.14: Time evolution of individual layer temperatures for assembly M_s-D
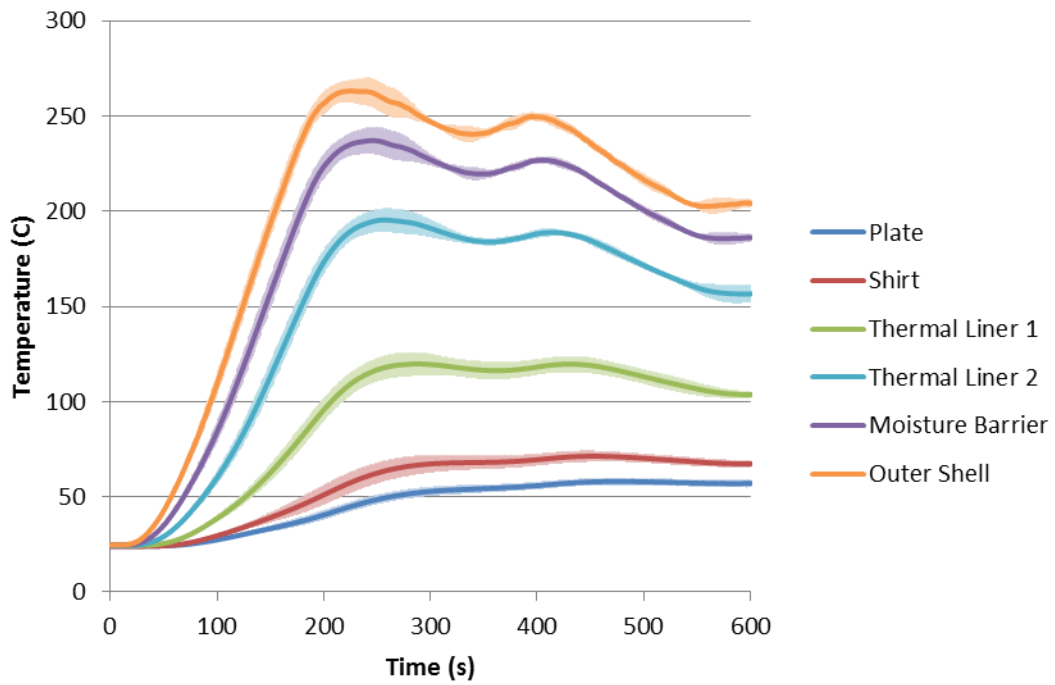
Figure F.15: Time evolution of individual layer temperatures for assembly M_t-D
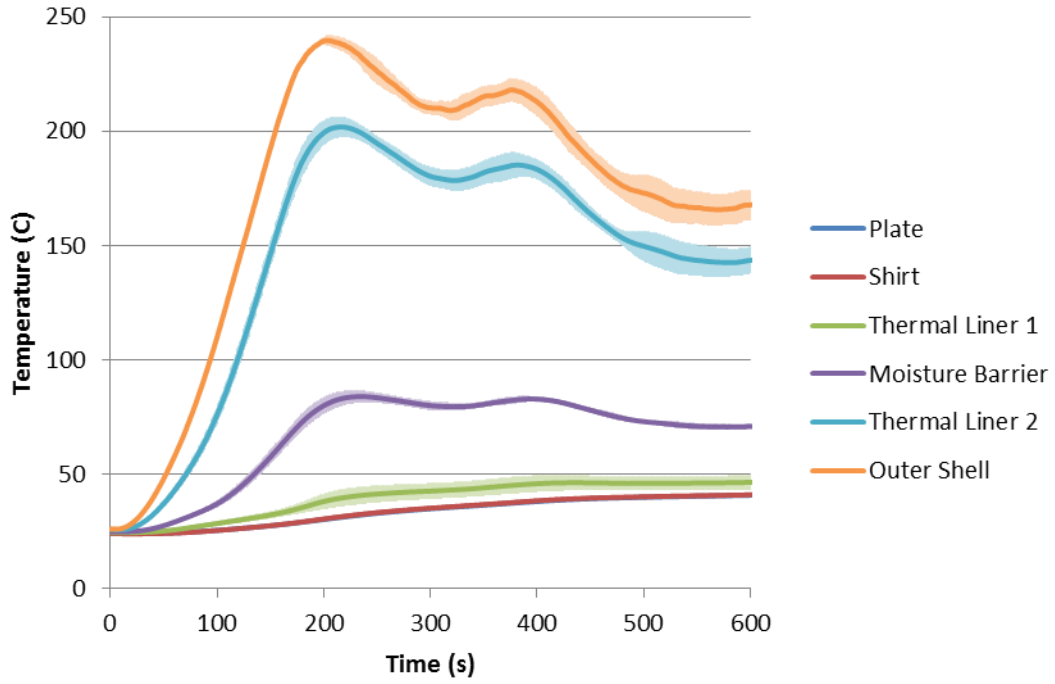
Figure F.16: Time evolution of individual layer temperatures for assembly M_s-W
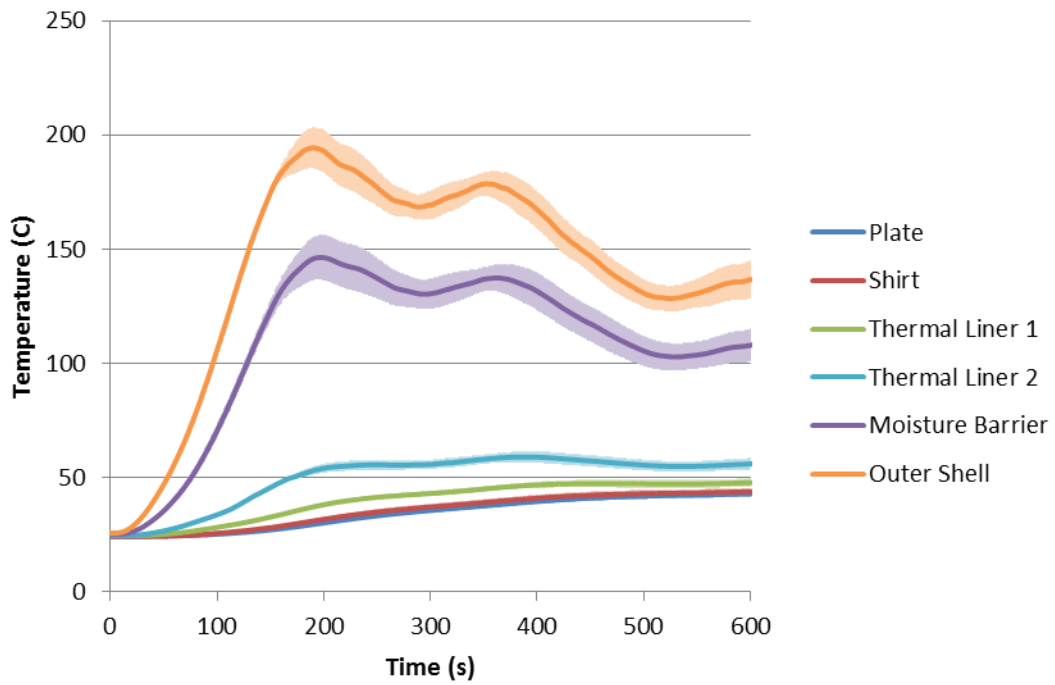
Figure F.17: Time evolution of individual layer temperatures for assembly M_t-W
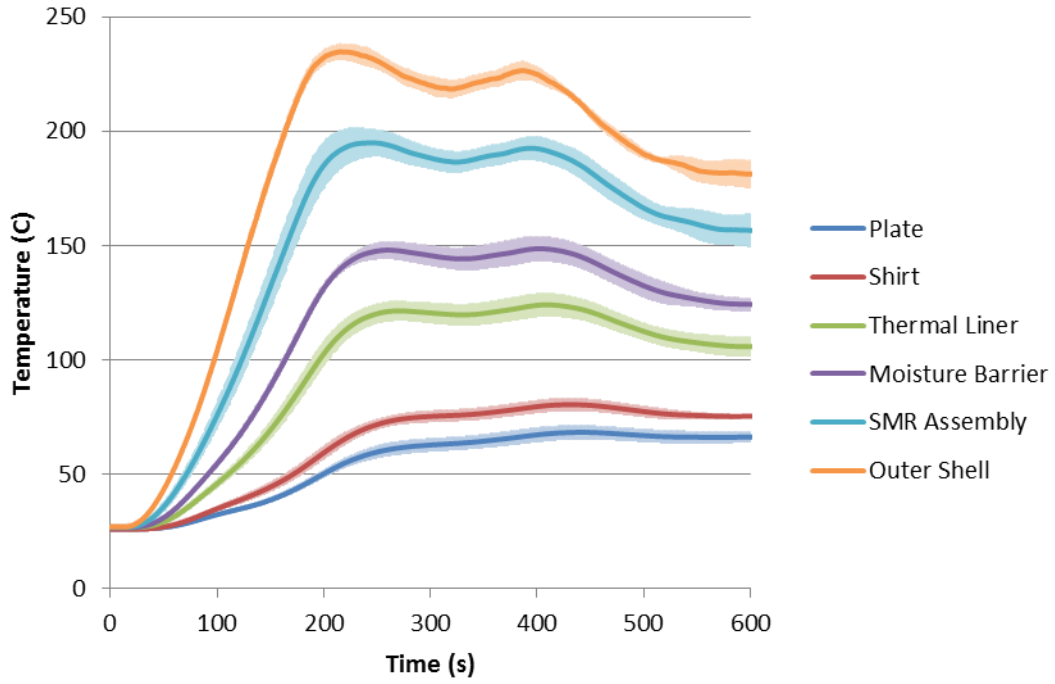
Figure F.18: Time evolution of individual layer temperatures for assembly E_o-$\emptyset$
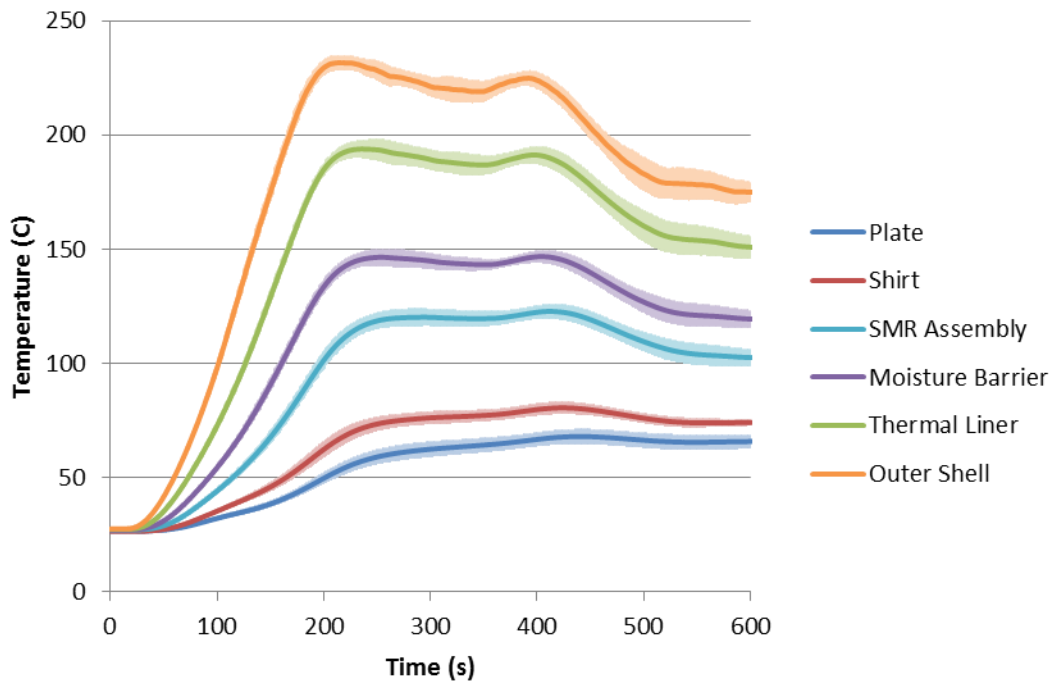
Figure F.19: Time evolution of individual layer temperatures for assembly E_i-$\emptyset$
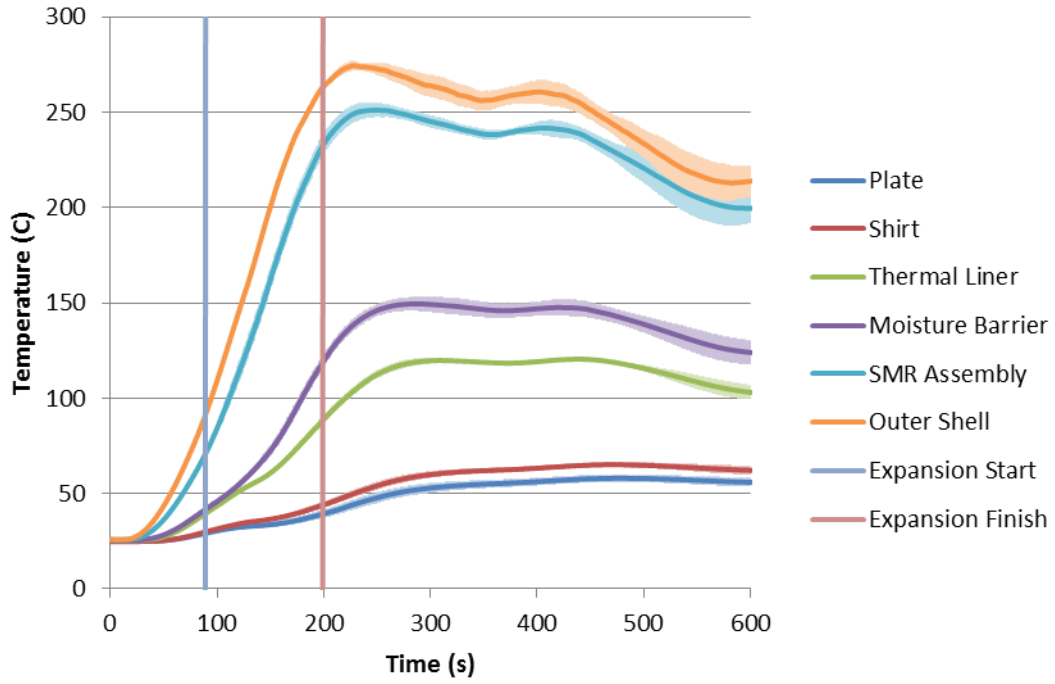
Figure F.20: Time evolution of individual layer temperatures for assembly E_o-50
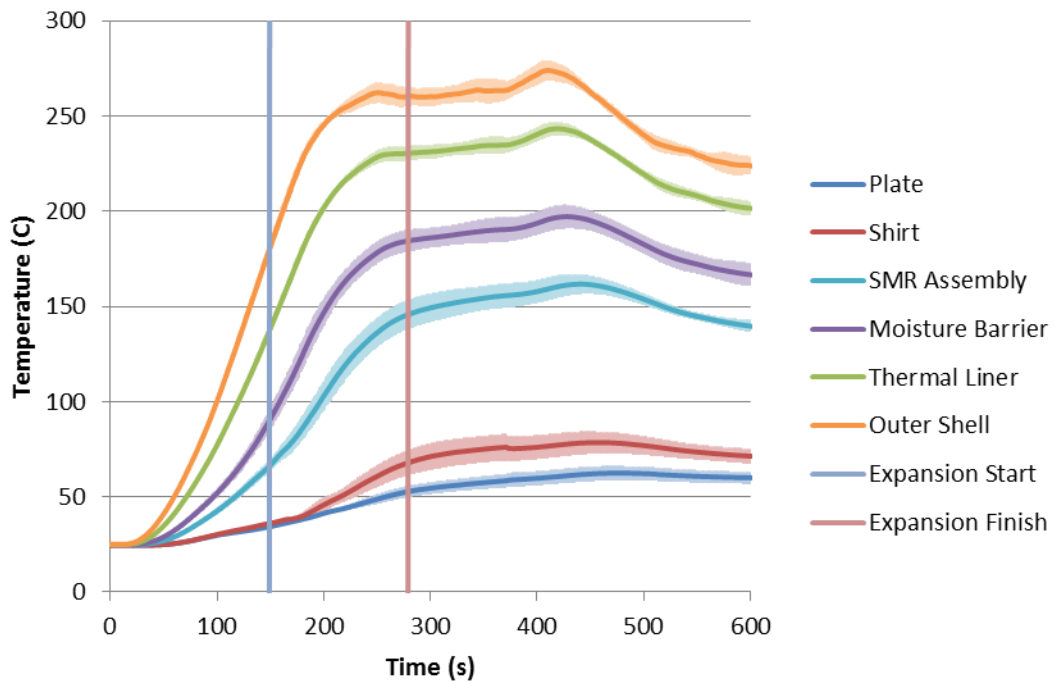
Figure F.21: Time evolution of individual layer temperatures for assembly E_i-50
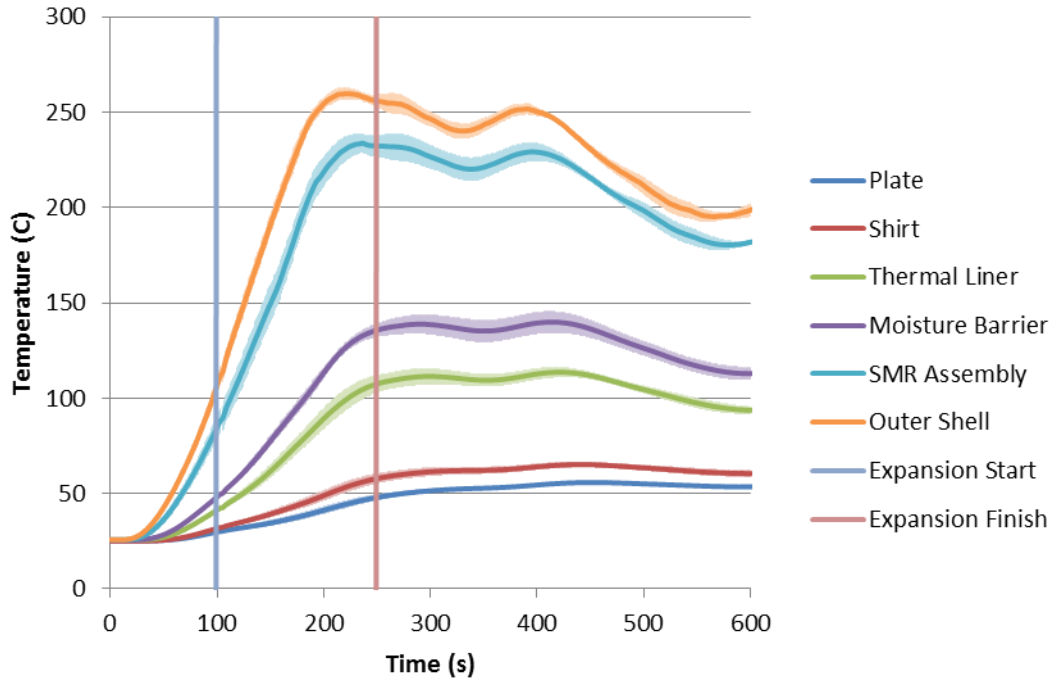
Figure F.22: Time evolution of individual layer temperatures for assembly E_o-90
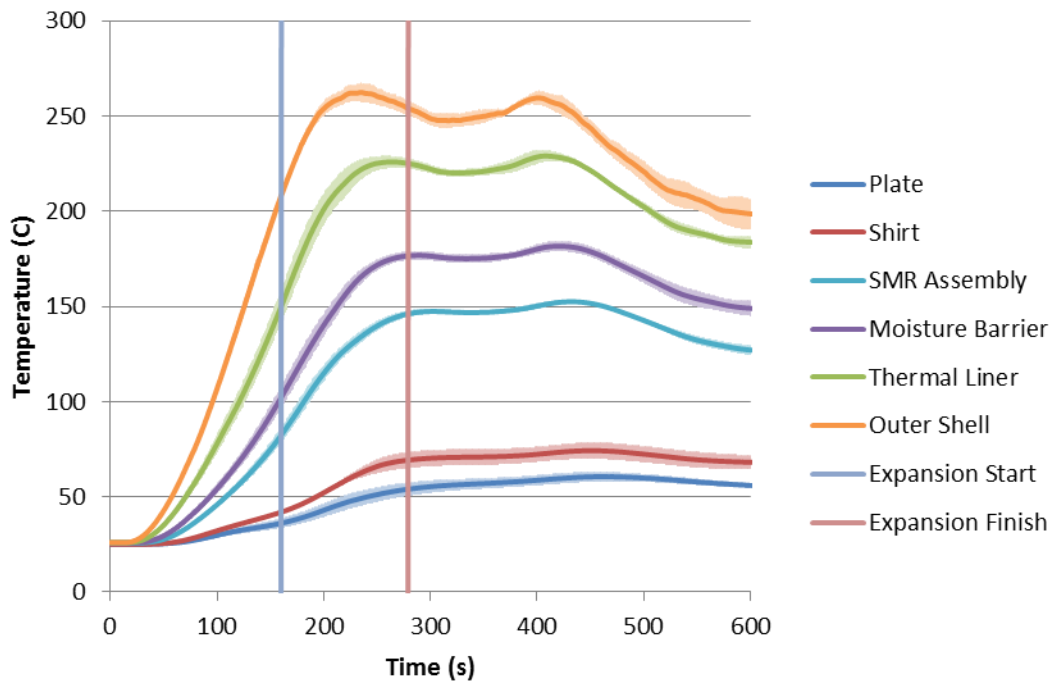
Figure F.23: Time evolution of individual layer temperatures for assembly E_i-90
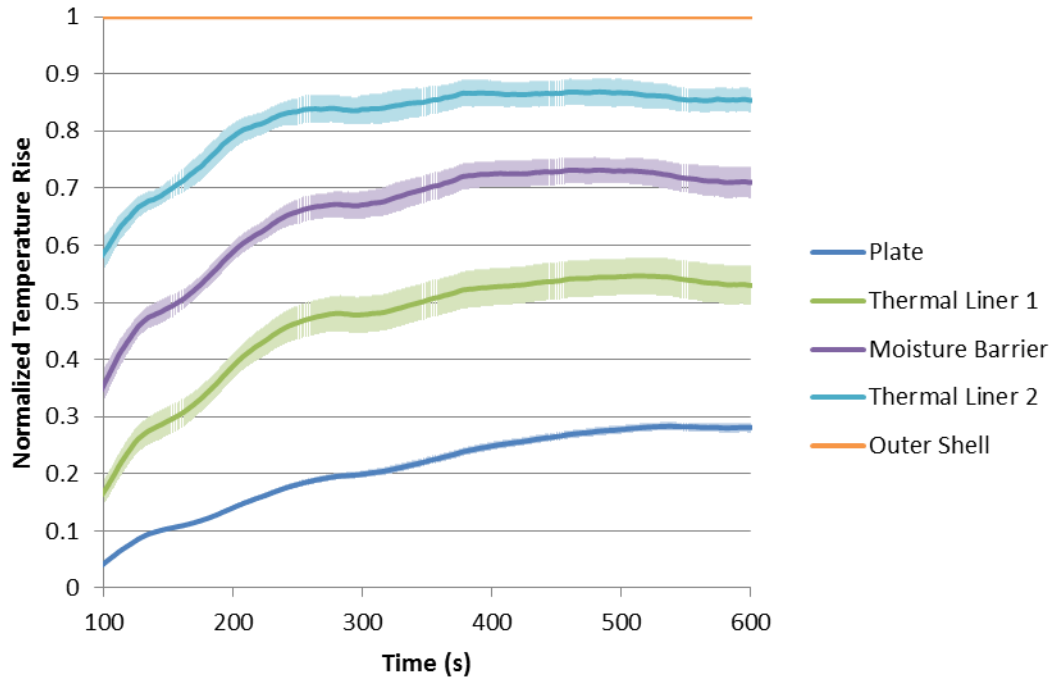
Figure G.1: Time evolution of individual layer *NTR* parameters for assembly *L-C*
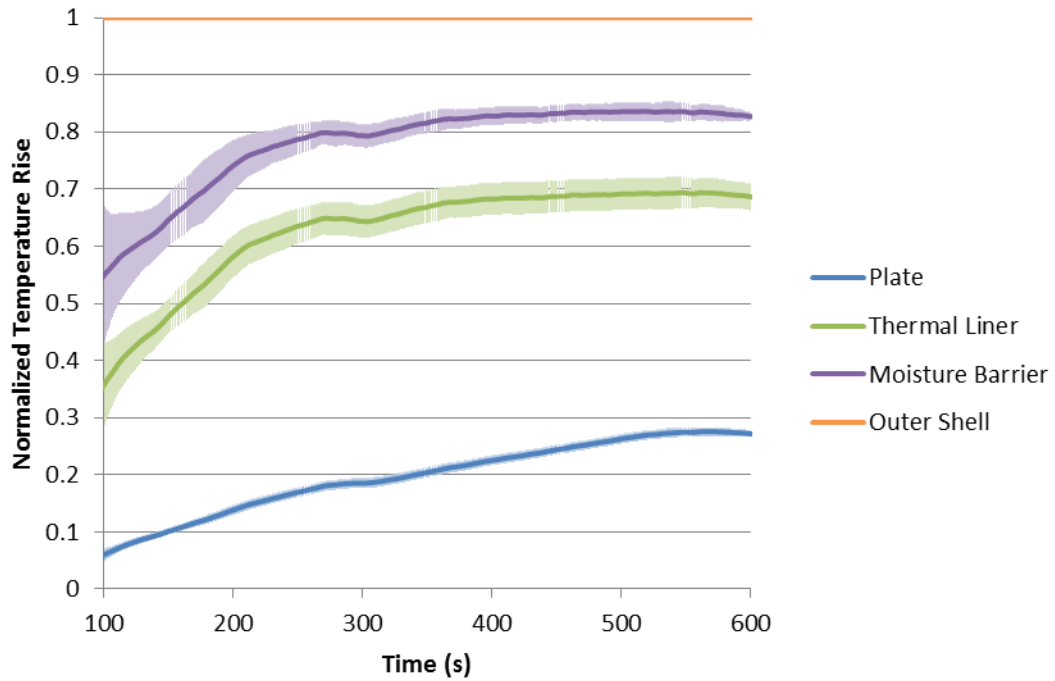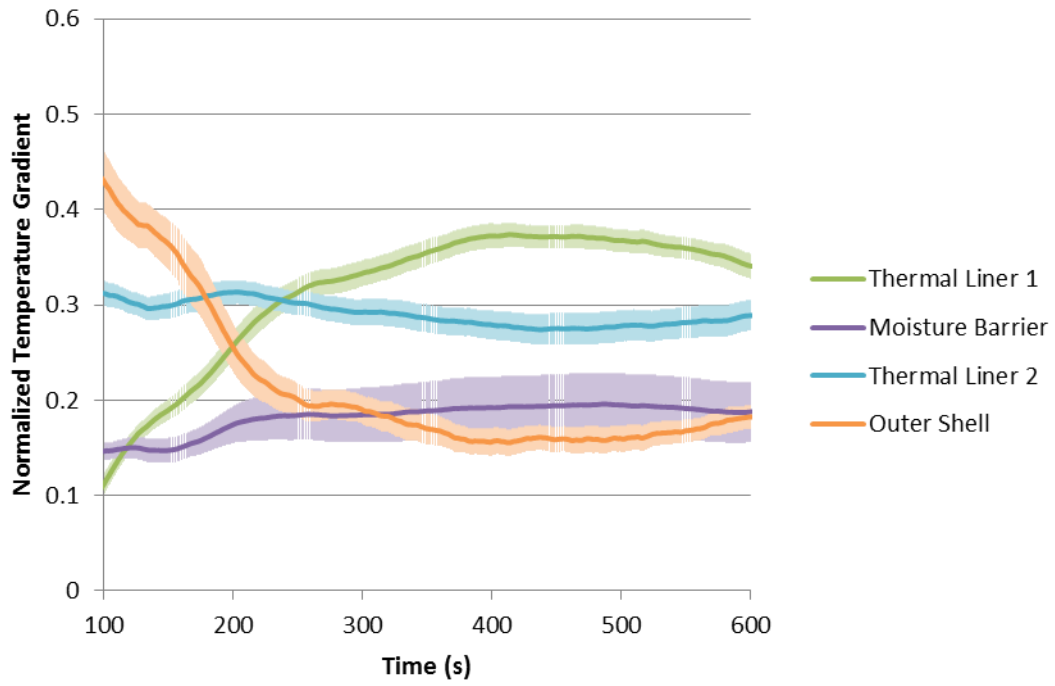

Figure G.2: Time evolution of individual layer *NTR* parameters for assembly *L-K*
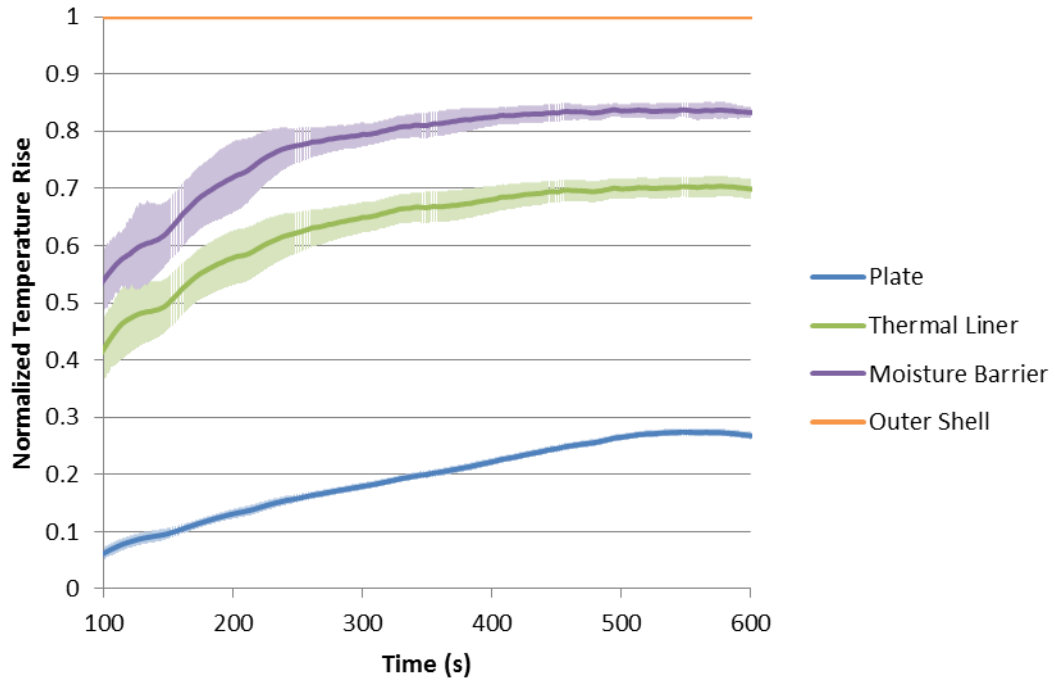
Figure G.3: Time evolution of individual layer *NTR* parameters for assembly *L-S*
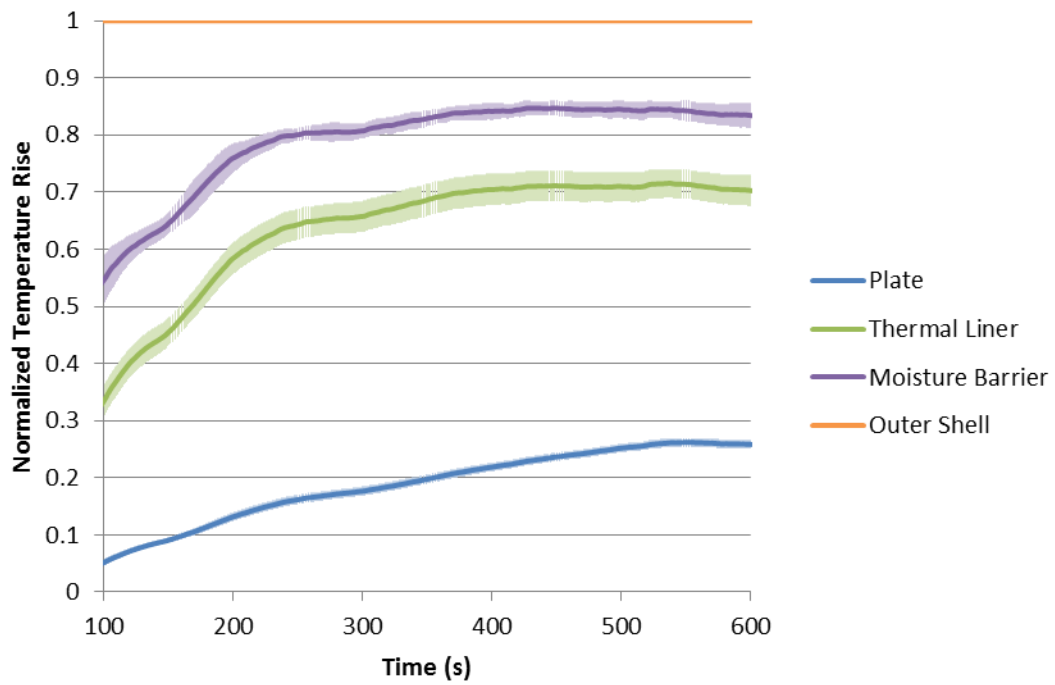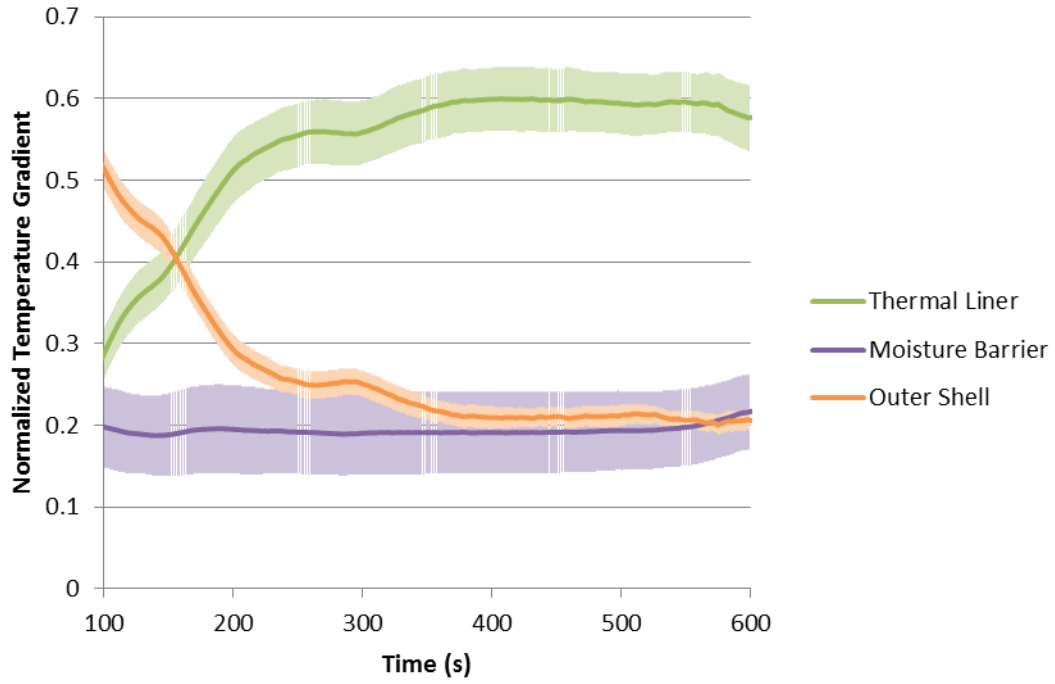

Figure G.4: Time evolution of individual layer *NTR* parameters for assembly *L-V*
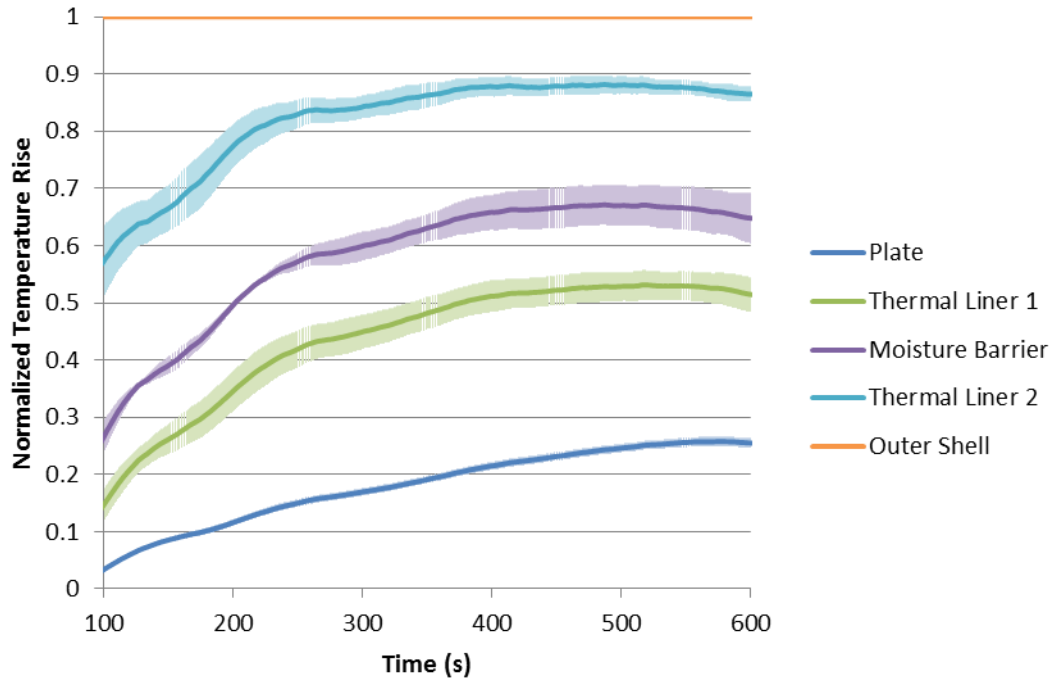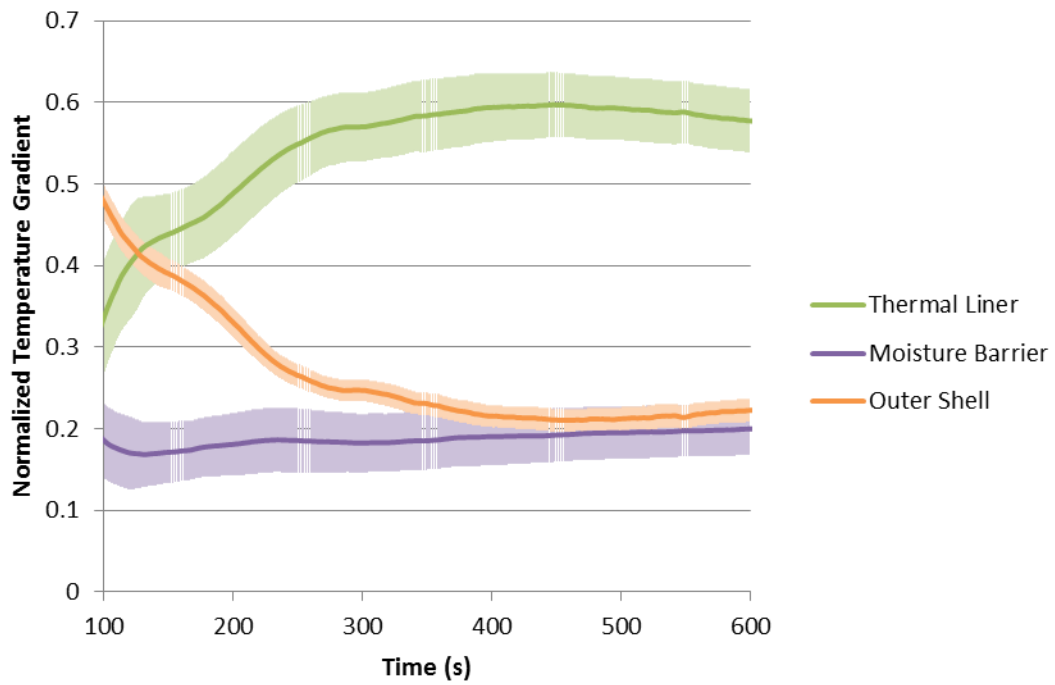
Figure G.5: Time evolution of individual layer *NTR* parameters for assembly *L-X*
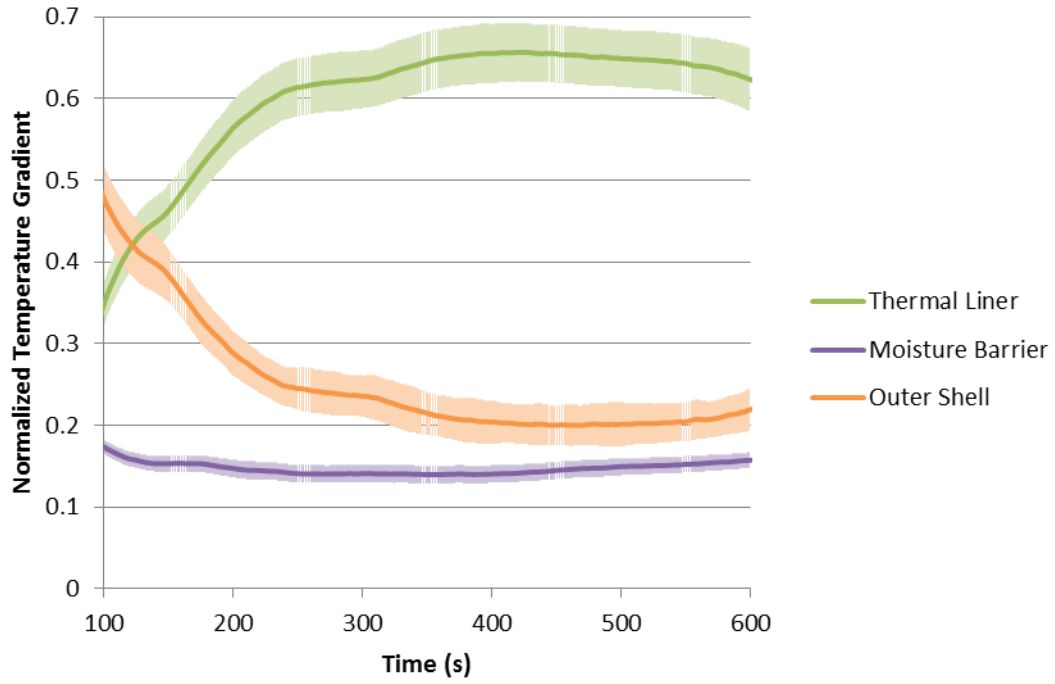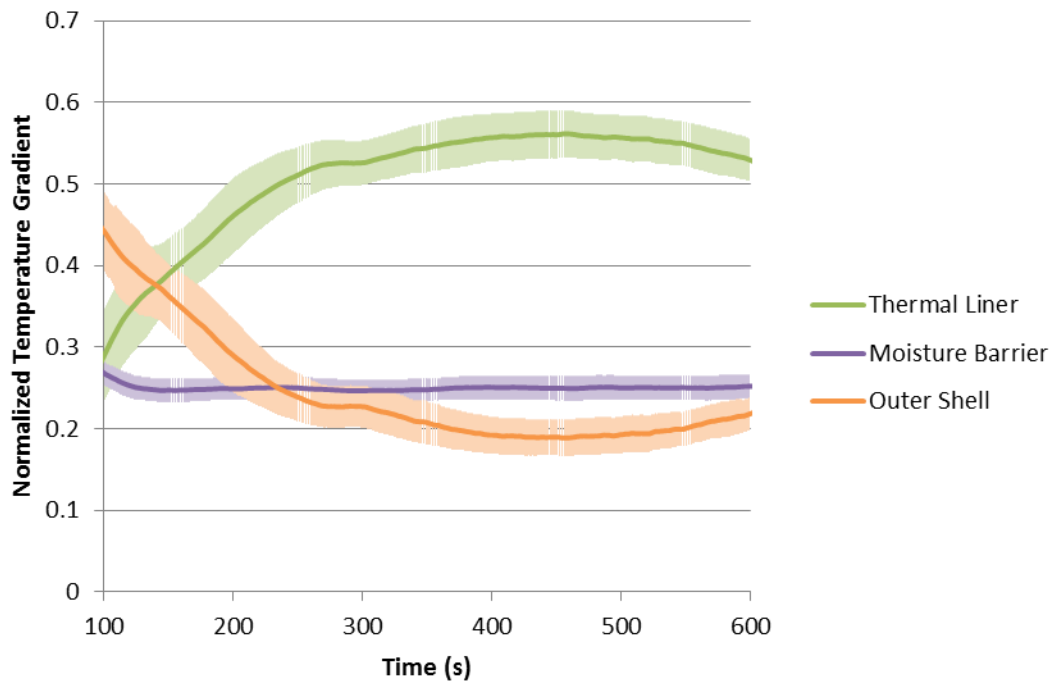
Space Intentionally Left Blank
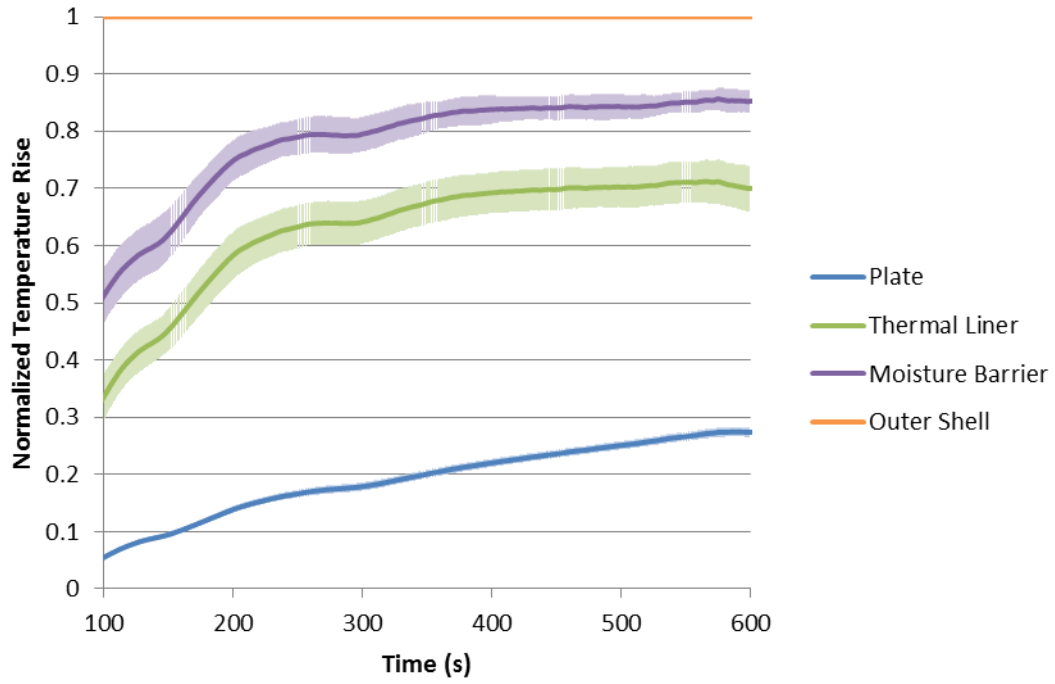
Figure G.6: Time evolution of individual layer *NTR* parameters for assembly *L-F*
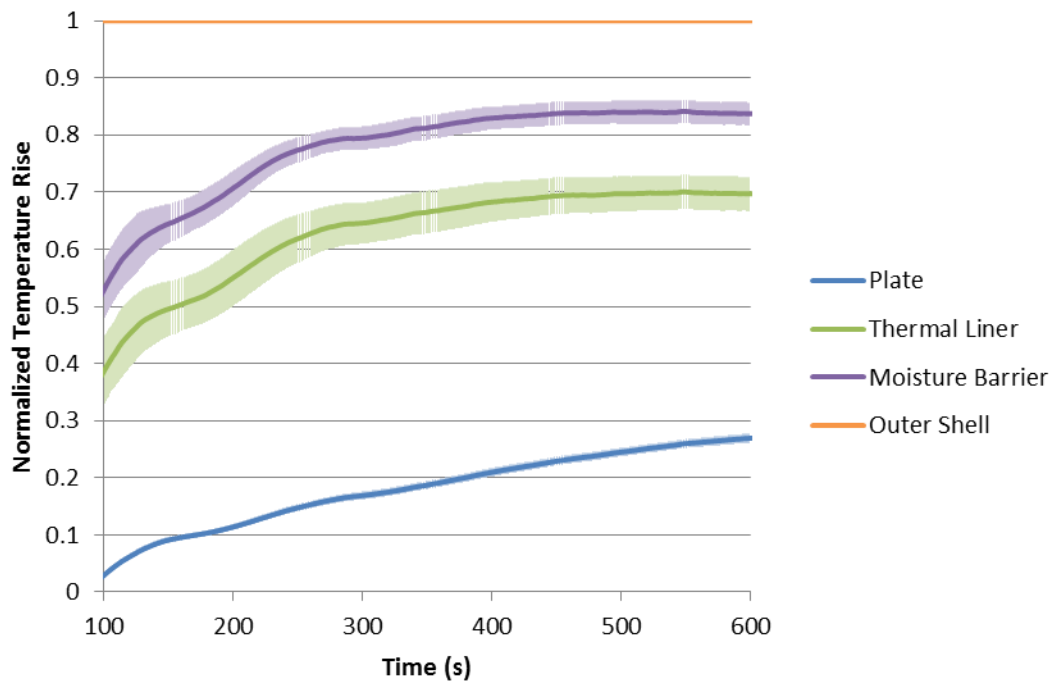
Figure G.7: Time evolution of individual layer *NTR* parameters for assembly *L-P*
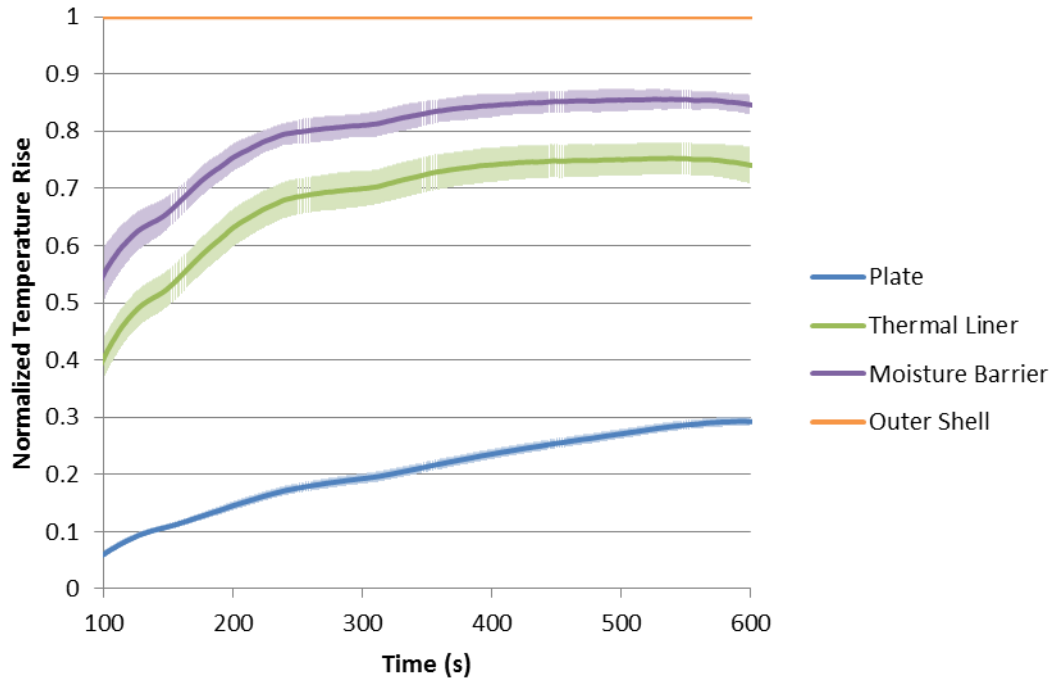
Figure G.8: Time evolution of individual layer *NTR* parameters for assembly *L-T*
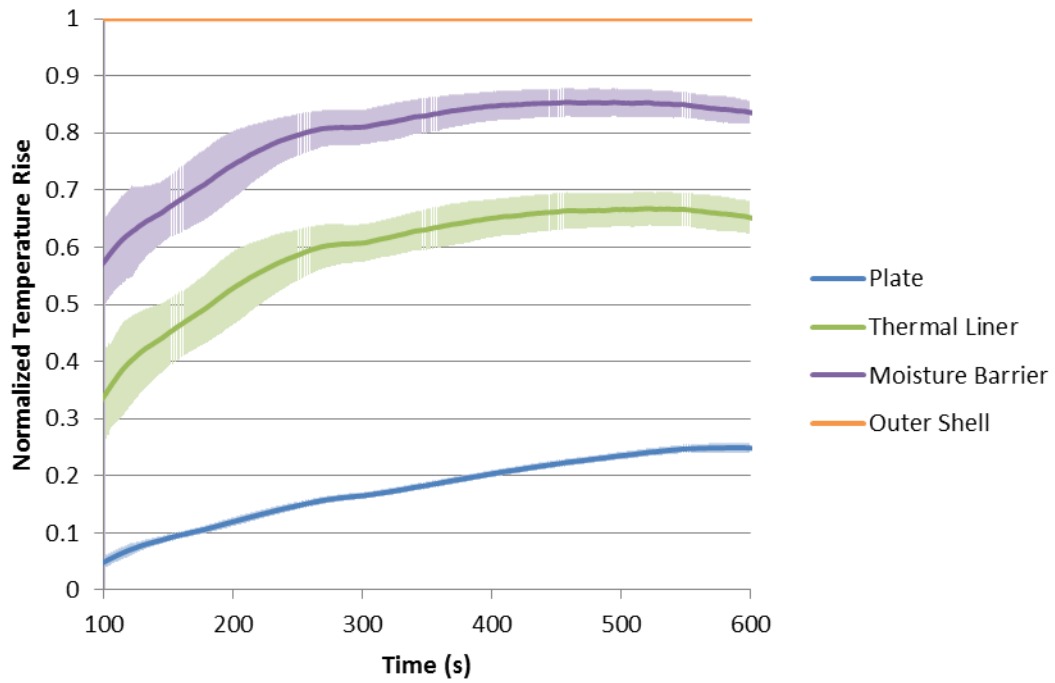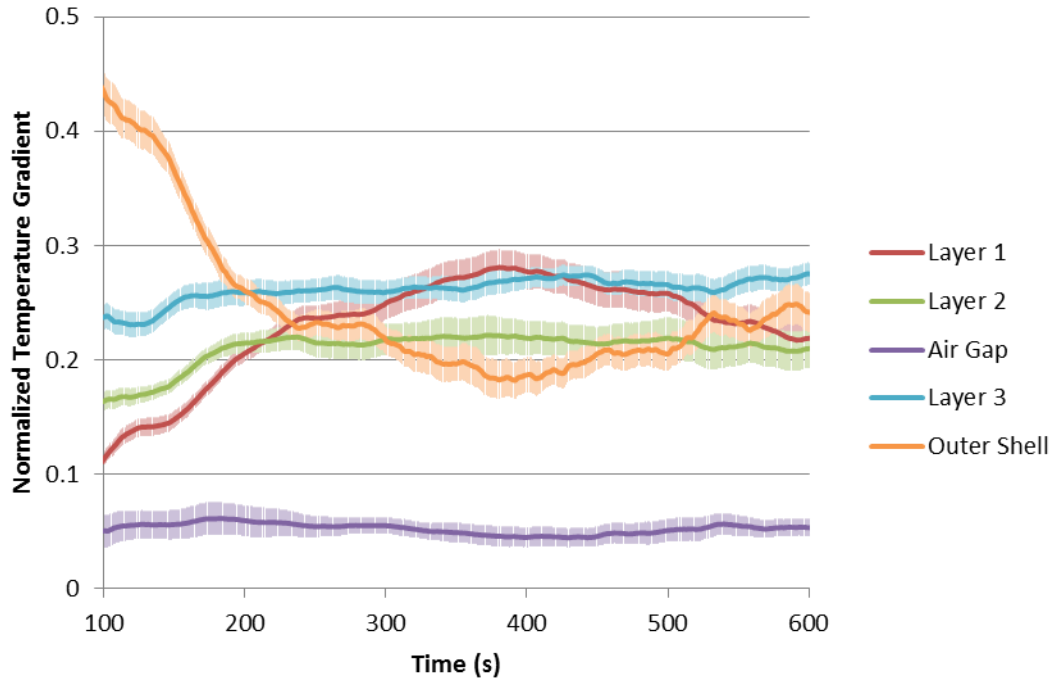

Figure G.9: Time evolution of individual layer *NTR* parameters for assembly *L-R*
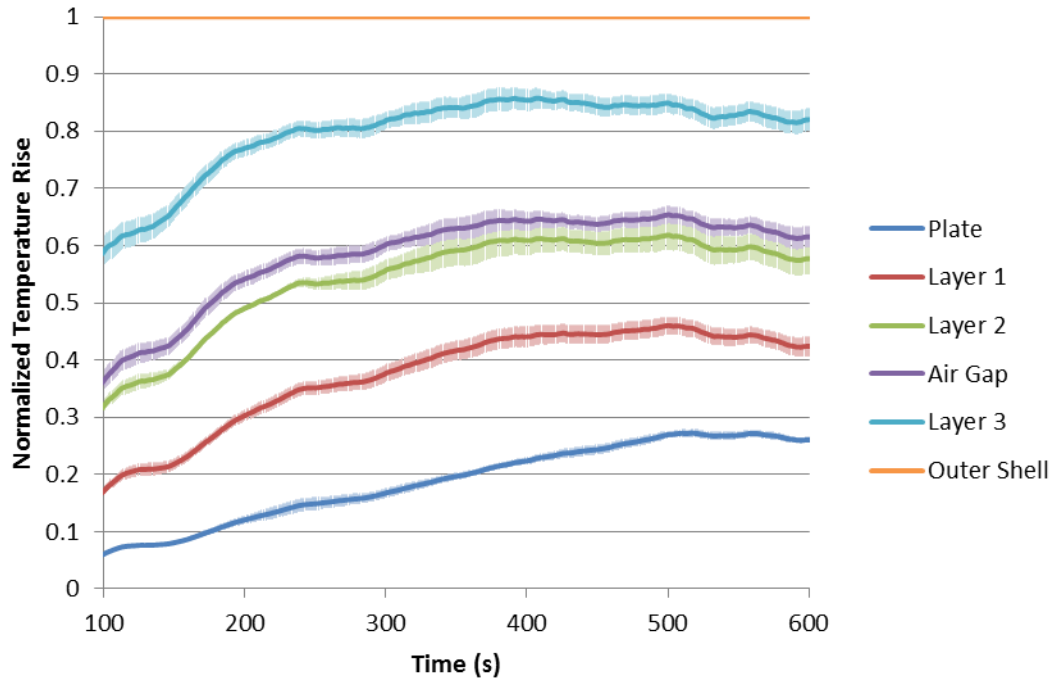
Figure G.10: Time evolution of individual layer *NTR* parameters for assembly *A*-0
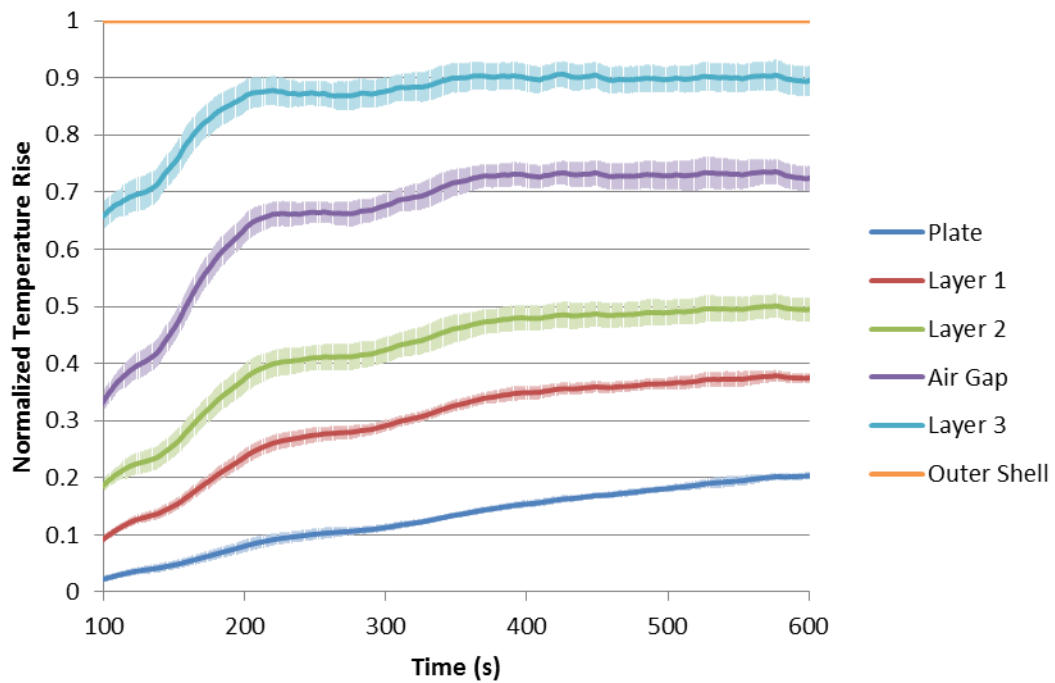
Figure G.11: Time evolution of individual layer *NTR* parameters for assembly *A*-1
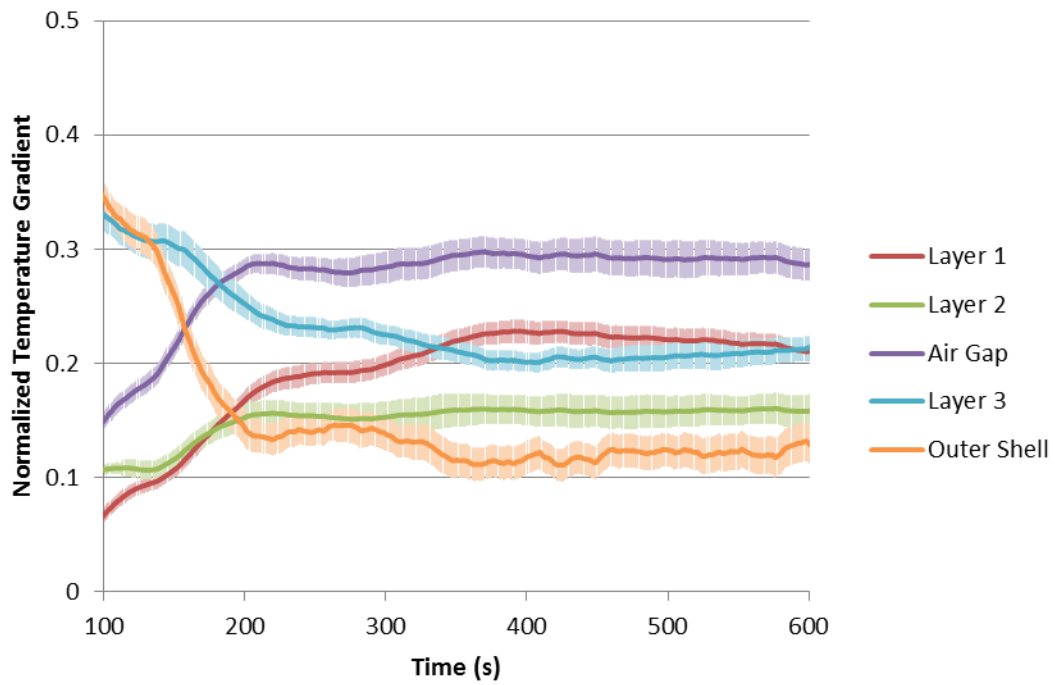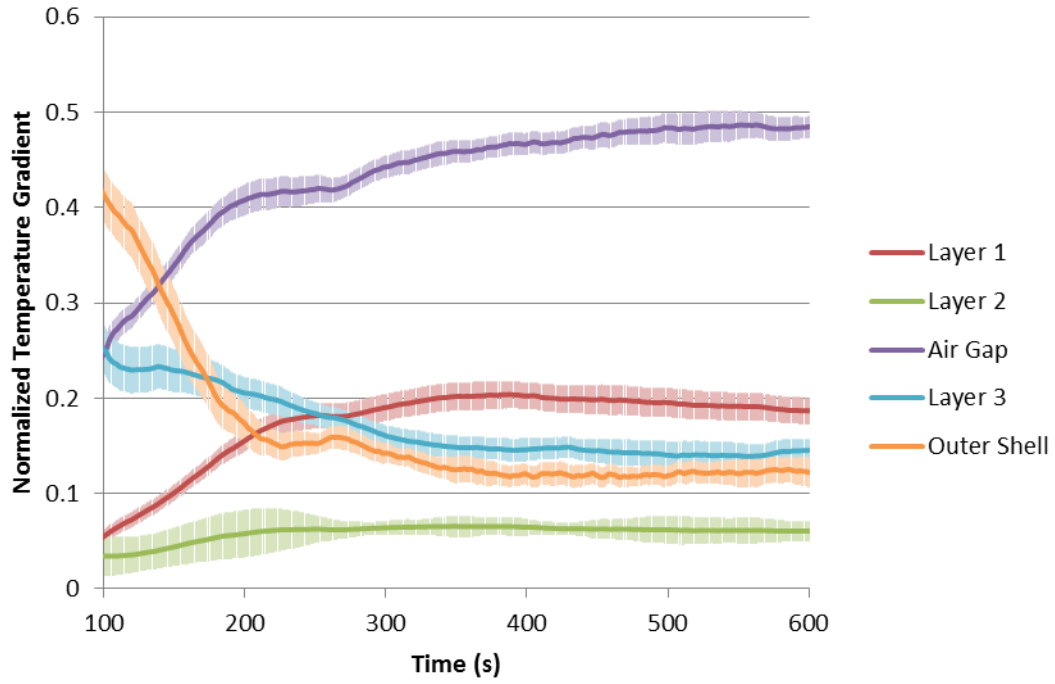
Figure G.12: Time evolution of individual layer *NTR* parameters for assembly *A*-2

Figure G.13: Time evolution of individual layer *NTR* parameters for assembly *A*-4

Figure G.14: Time evolution of individual layer NTR parameters for assembly M_s-D
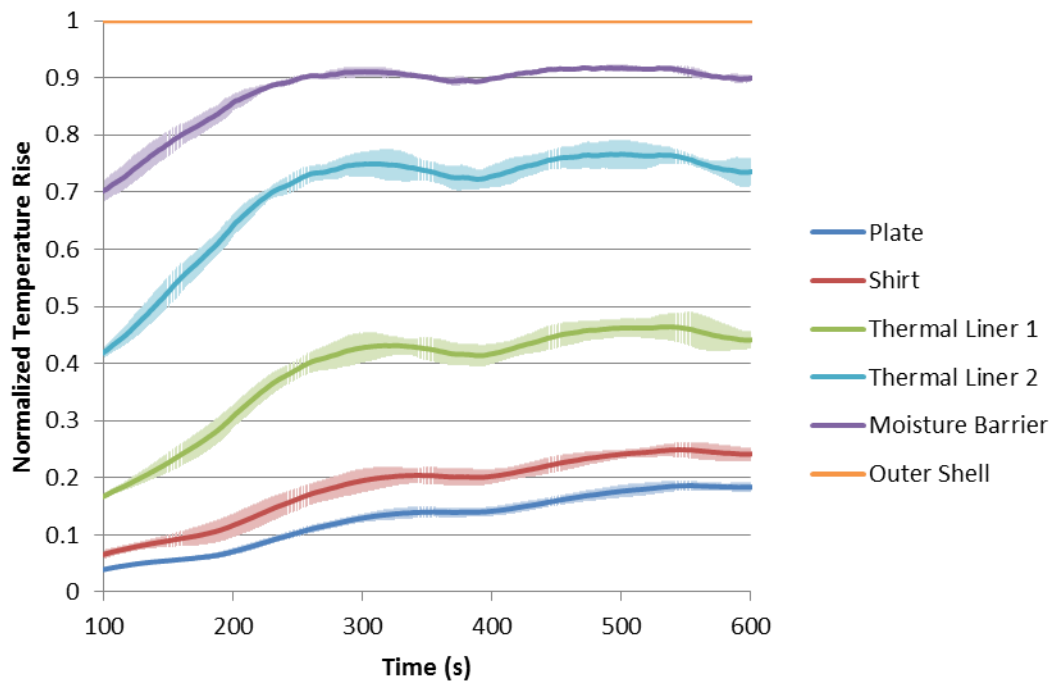
Figure G.15: Time evolution of individual layer NTR parameters for assembly M_t-D
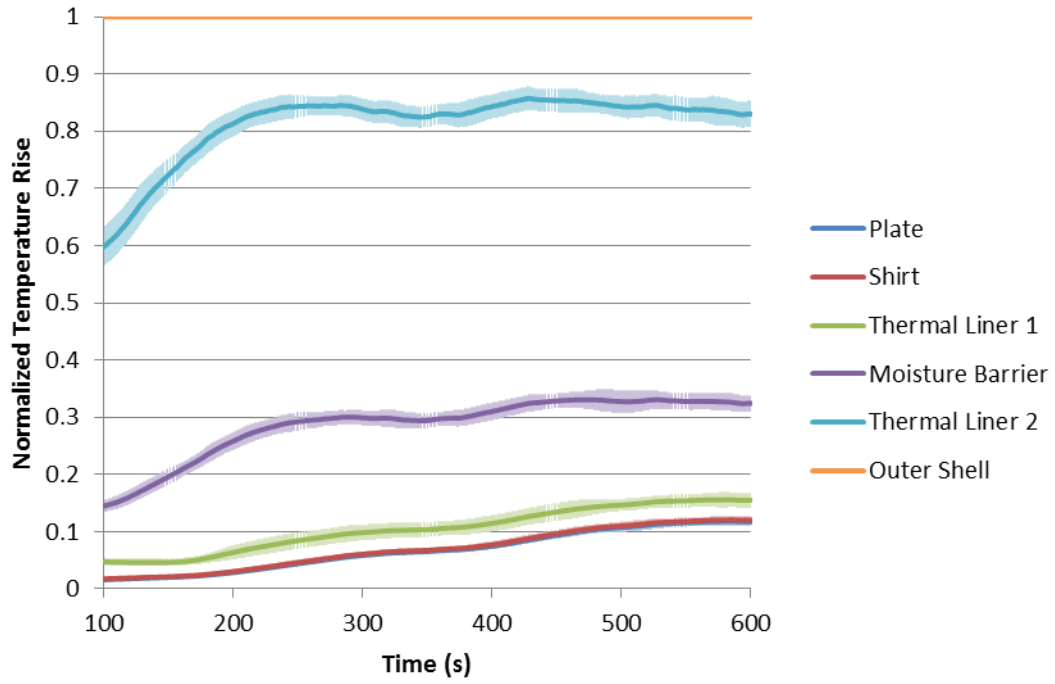
Figure G.16: Time evolution of individual layer NTR parameters for assembly M_s-W
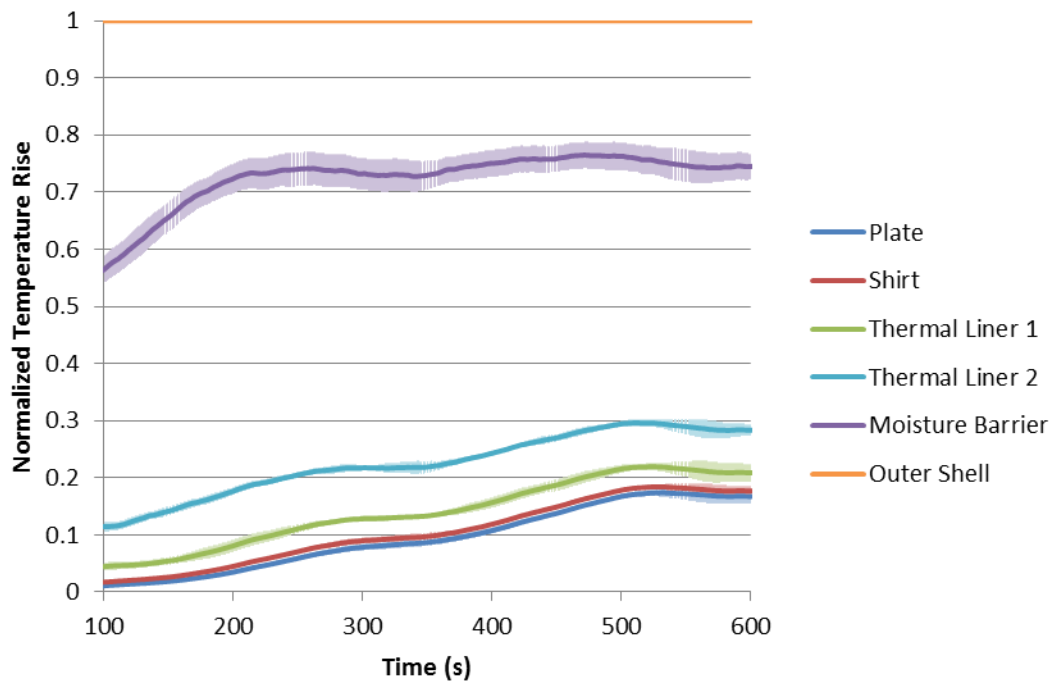
Figure G.17: Time evolution of individual layer NTR parameters for assembly M_t-W
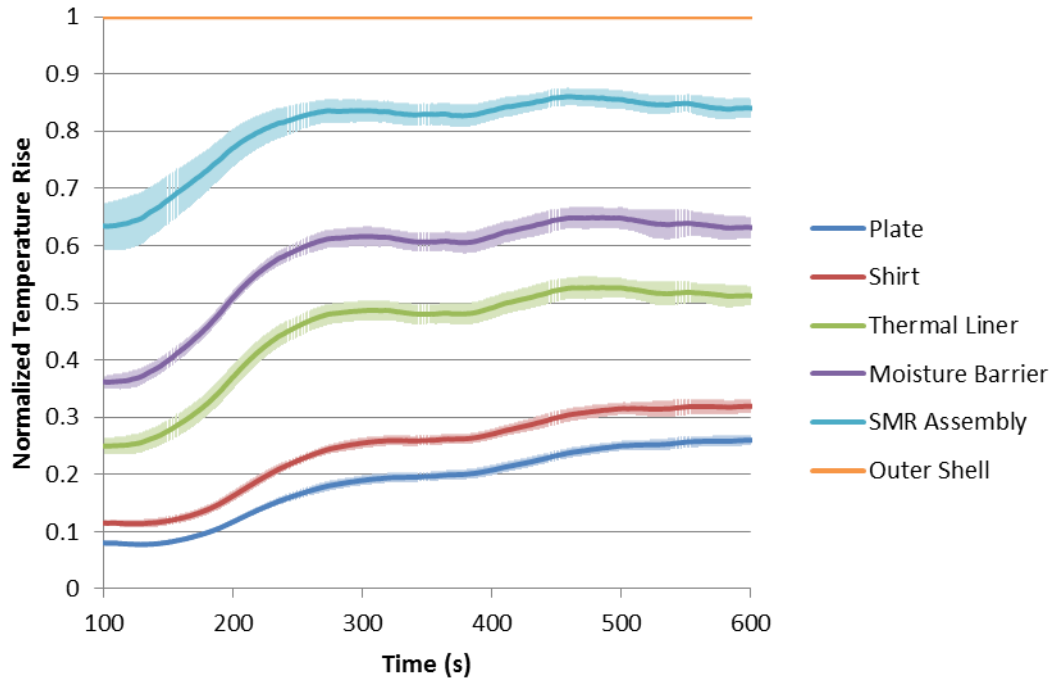
Figure G.18: Time evolution of individual layer NTR parameters for assembly E_o-$\emptyset$
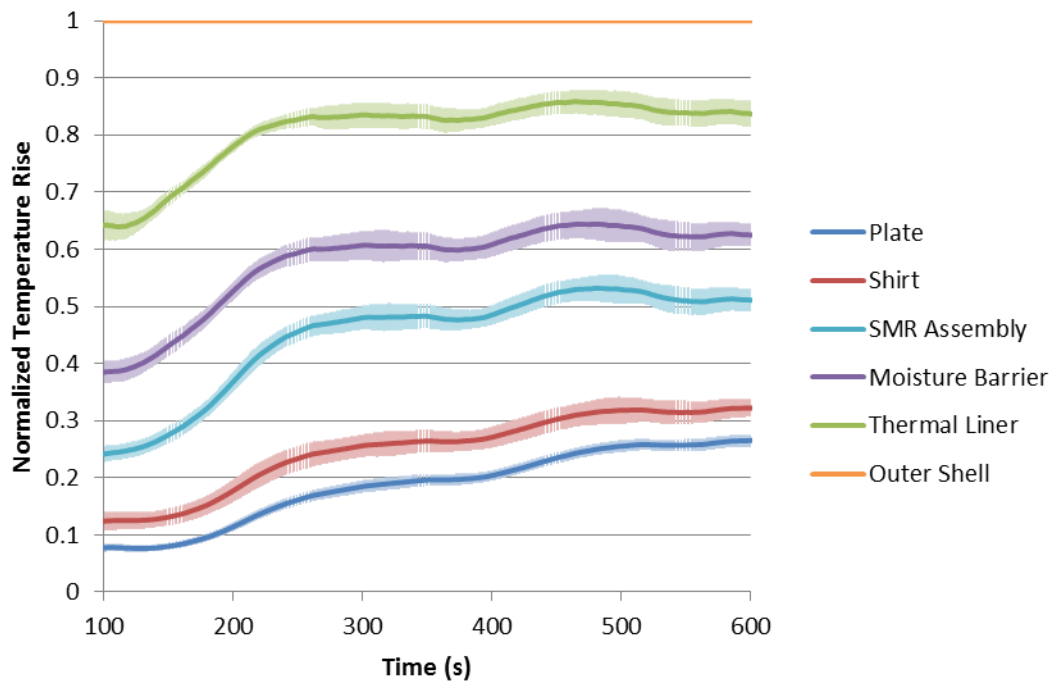
Figure G.19: Time evolution of individual layer NTR parameters for assembly E_i-$\emptyset$
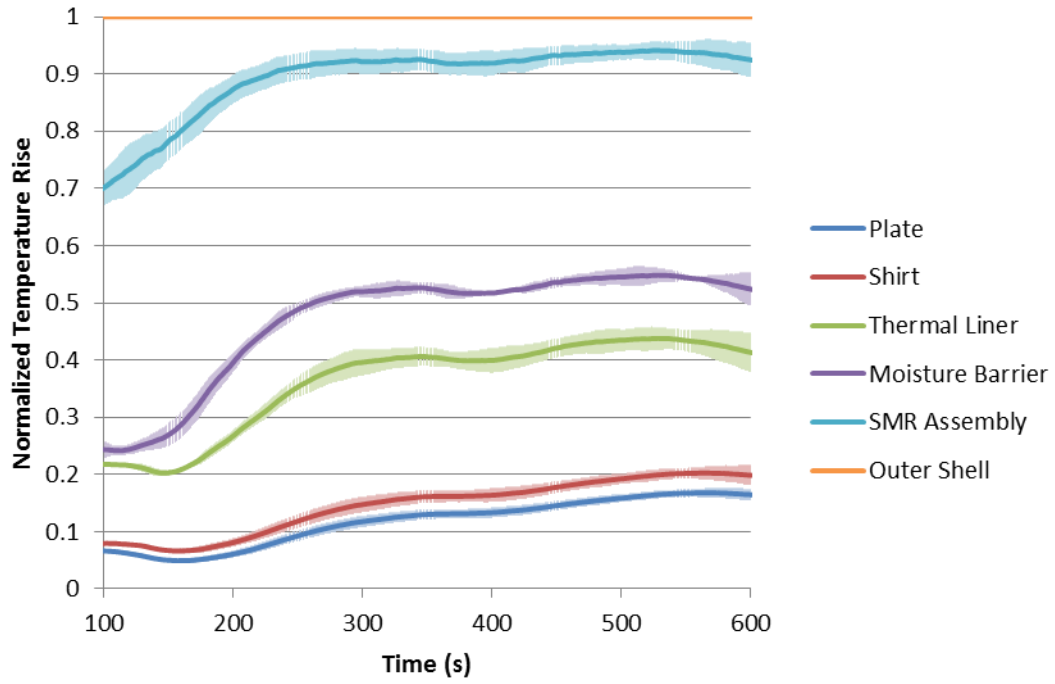
Figure G.20: Time evolution of individual layer NTR parameters for assembly E_o-50
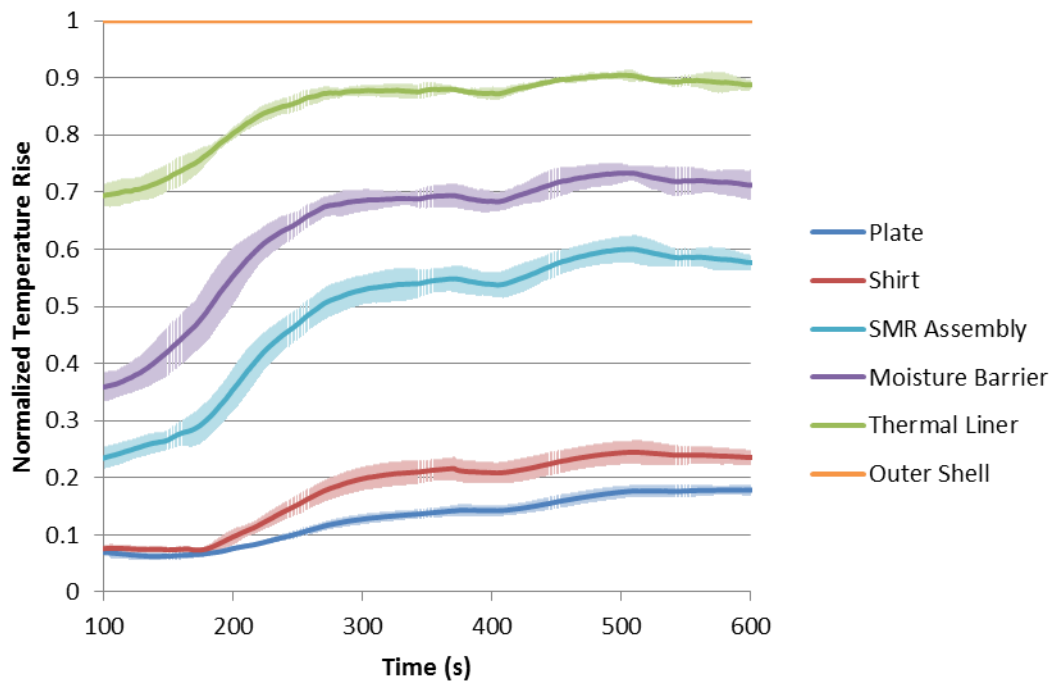
Figure G.21: Time evolution of individual layer NTR parameters for assembly E_i-50
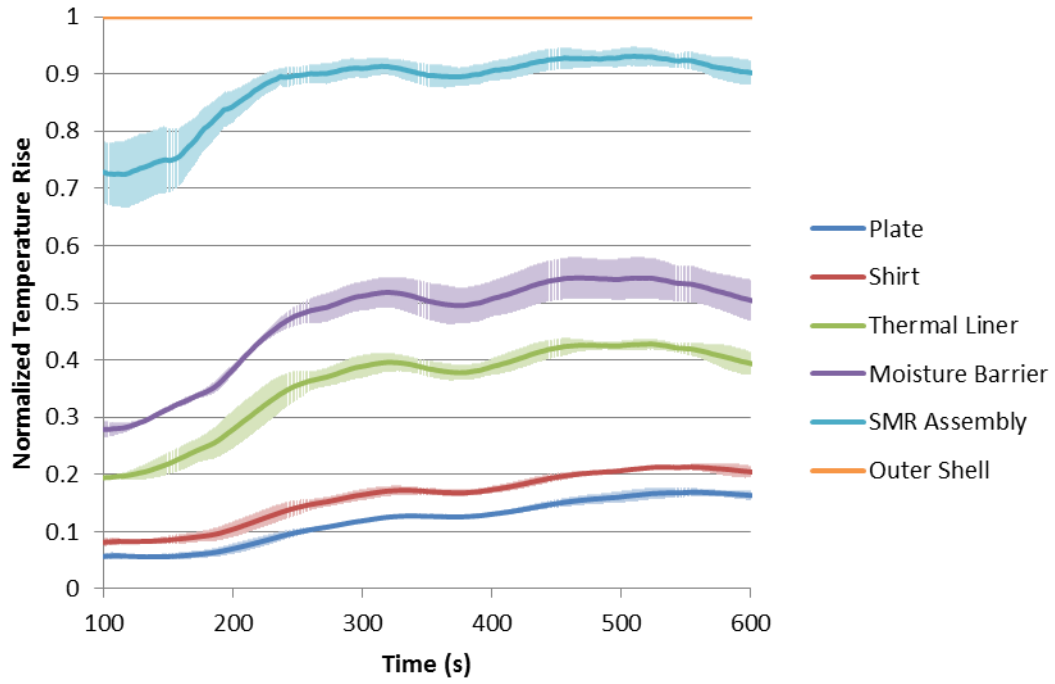
Figure G.22: Time evolution of individual layer *NTR* parameters for assembly E_o-90
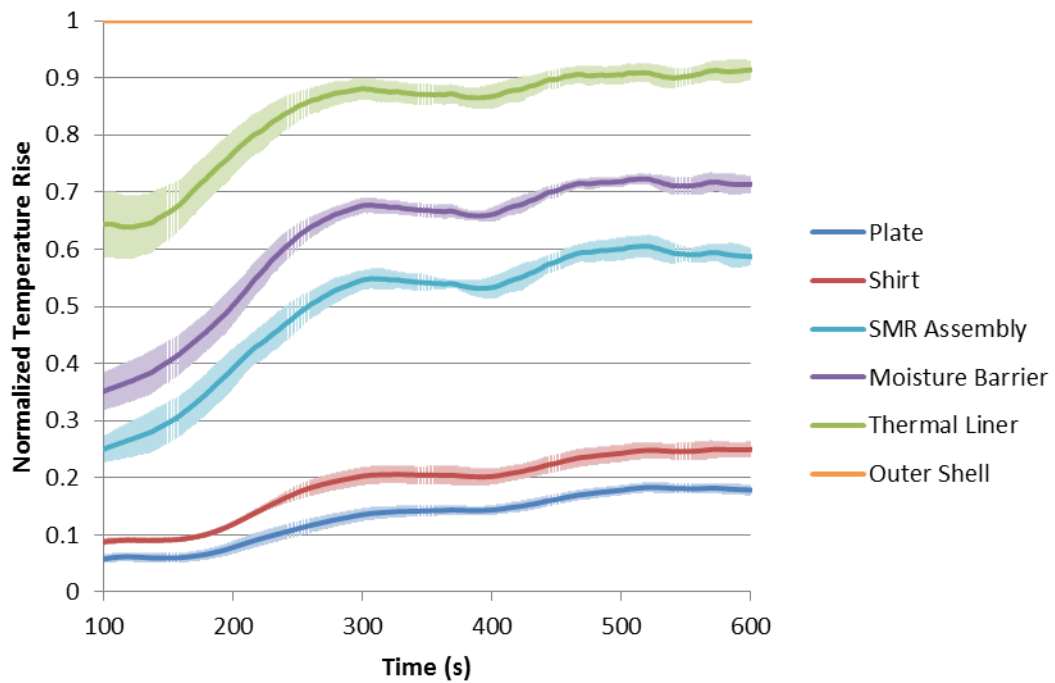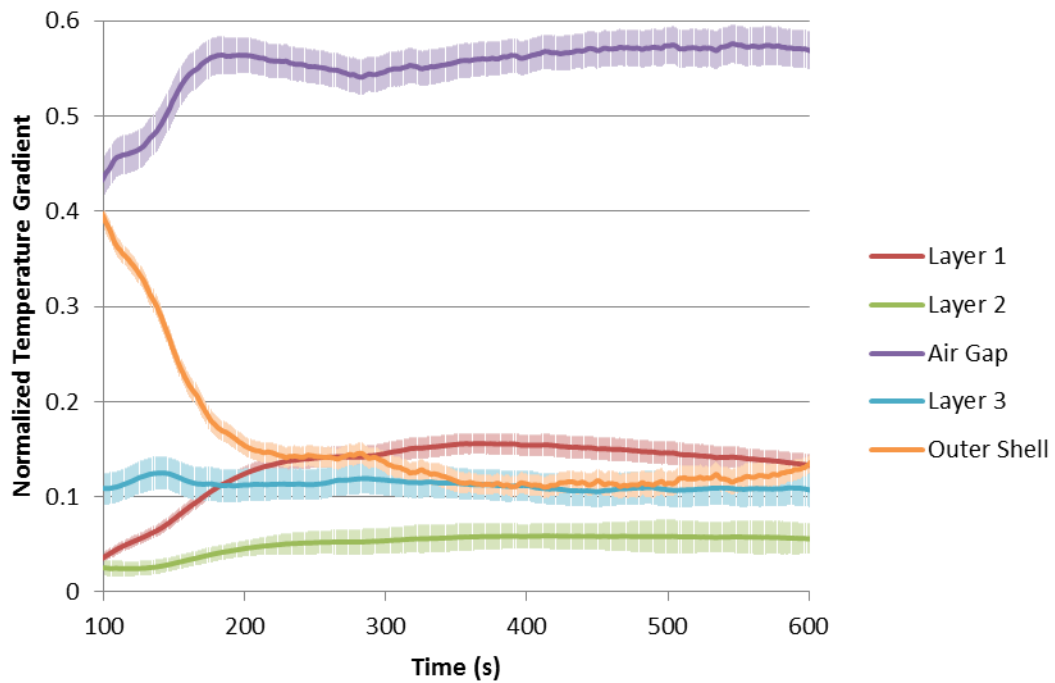

Figure G.23: Time evolution of individual layer *NTR* parameters for assembly E_i-90
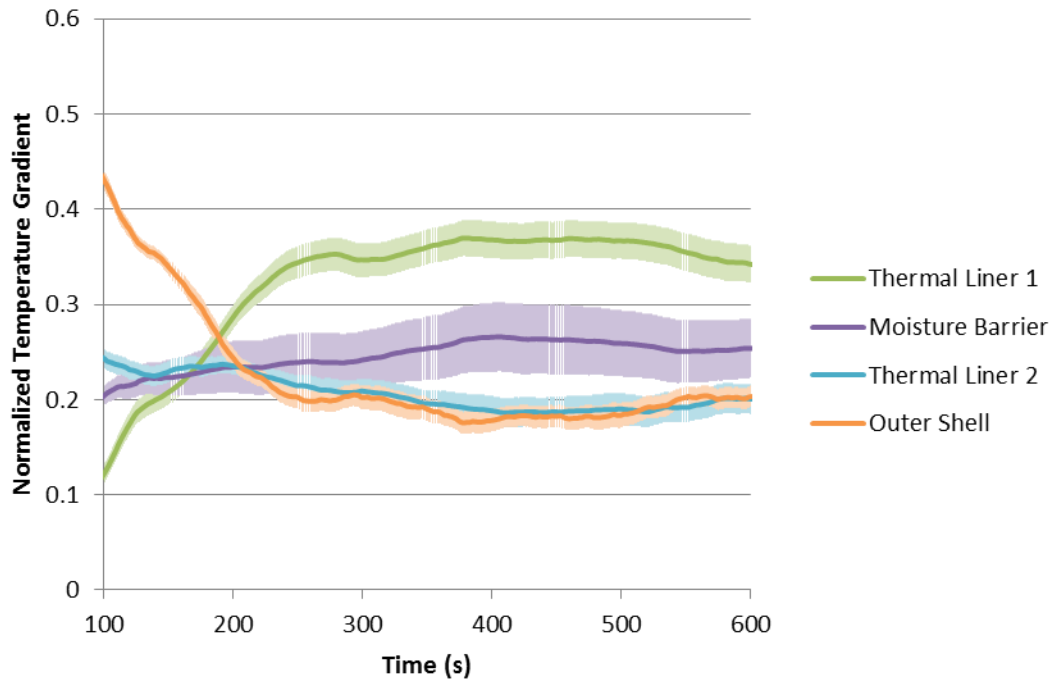
Figure H.1: Time evolution of individual layer *NTG* parameters for assembly *L-C*
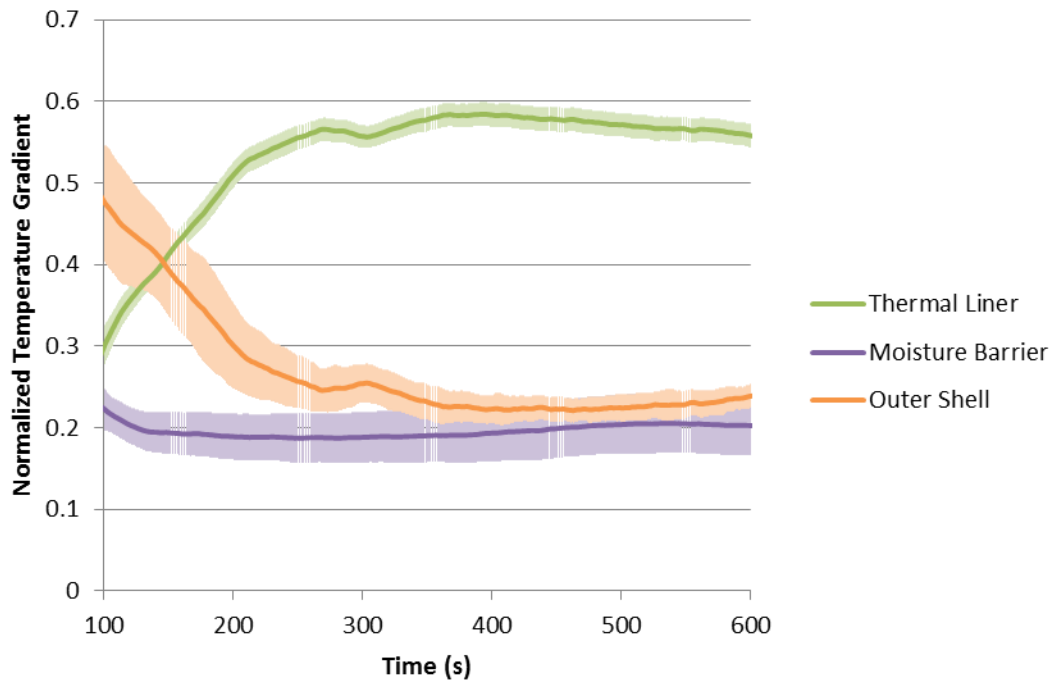
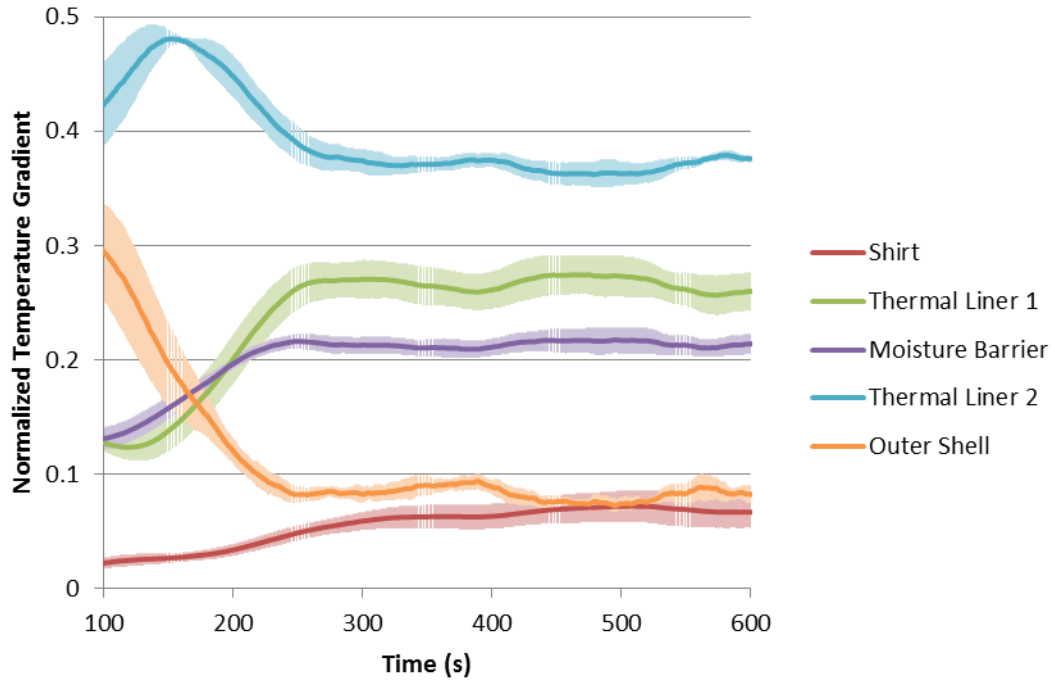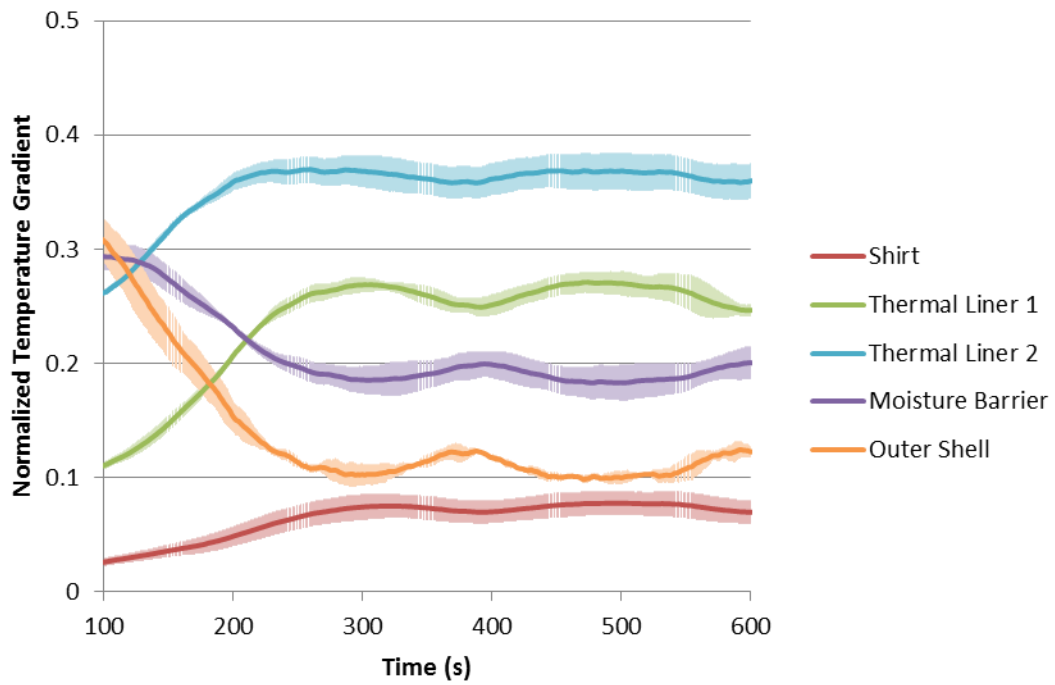**Figure H.2**: Time evolution of individual layer *NTG* parameters for assembly *L-K*
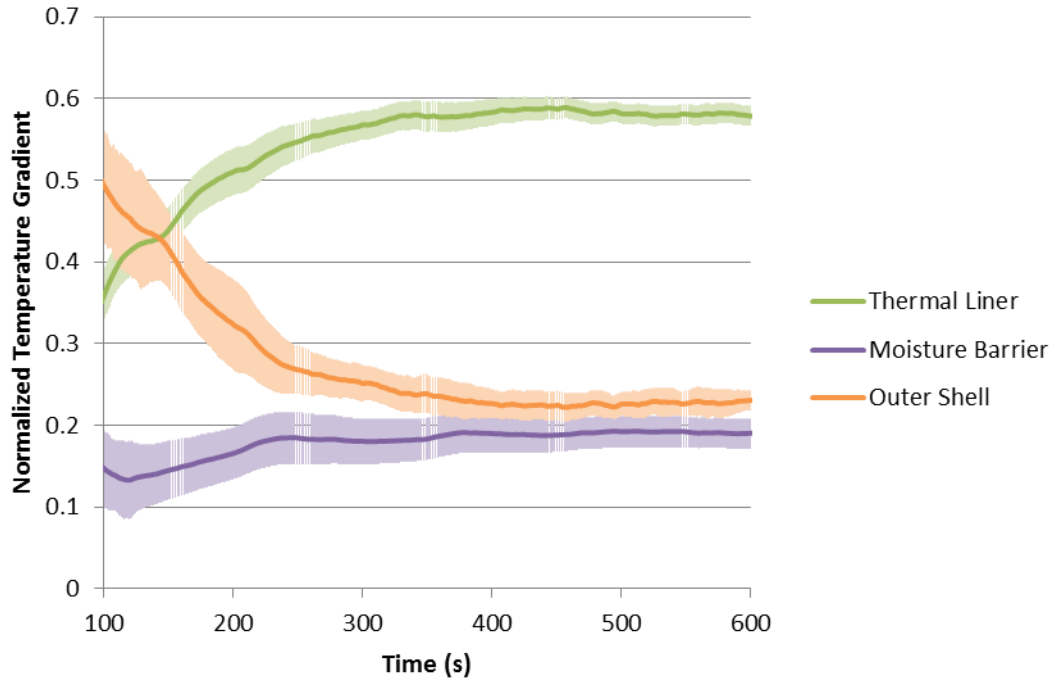
Figure H.3: Time evolution of individual layer NTG parameters for assembly L-S
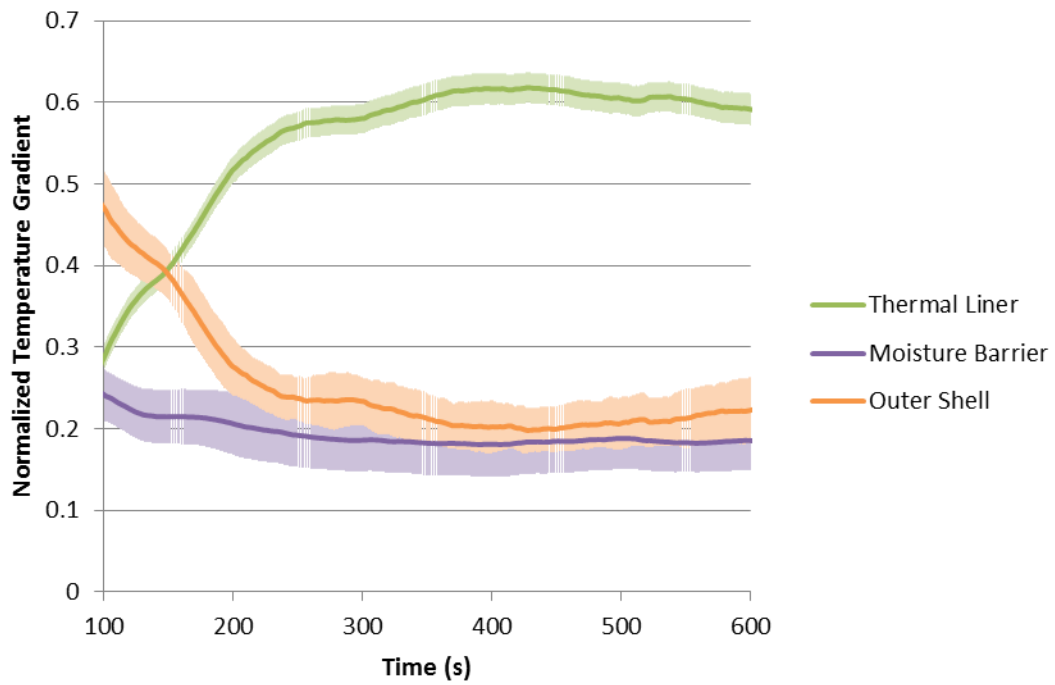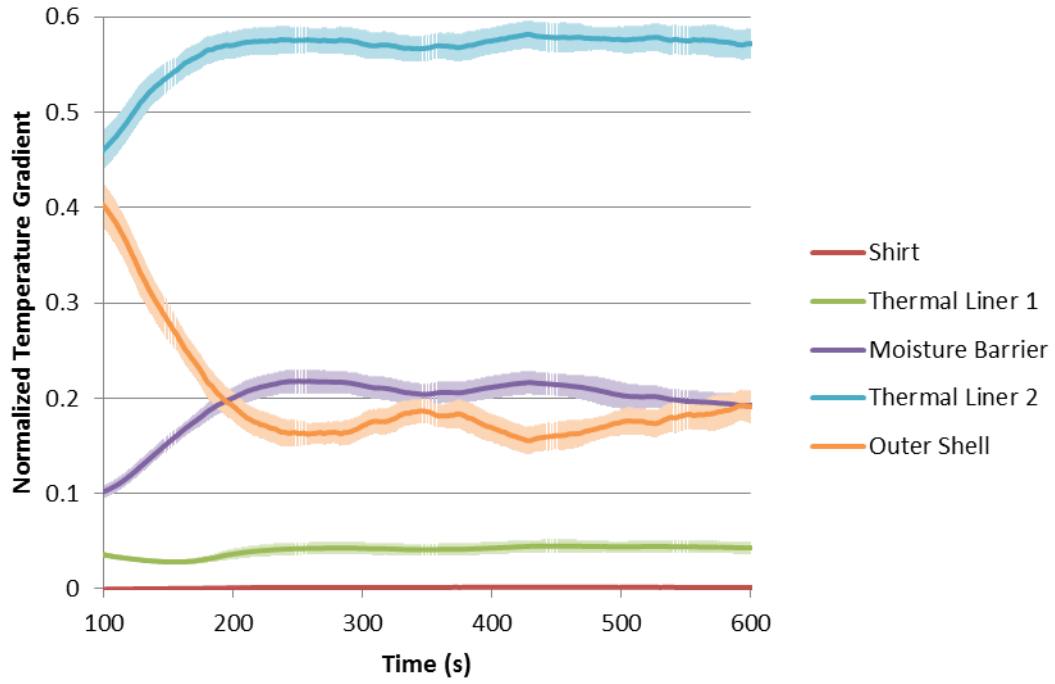

Figure H.4: Time evolution of individual layer NTG parameters for assembly L-V

Figure H.5: Time evolution of individual layer NTG parameters for assembly L-X
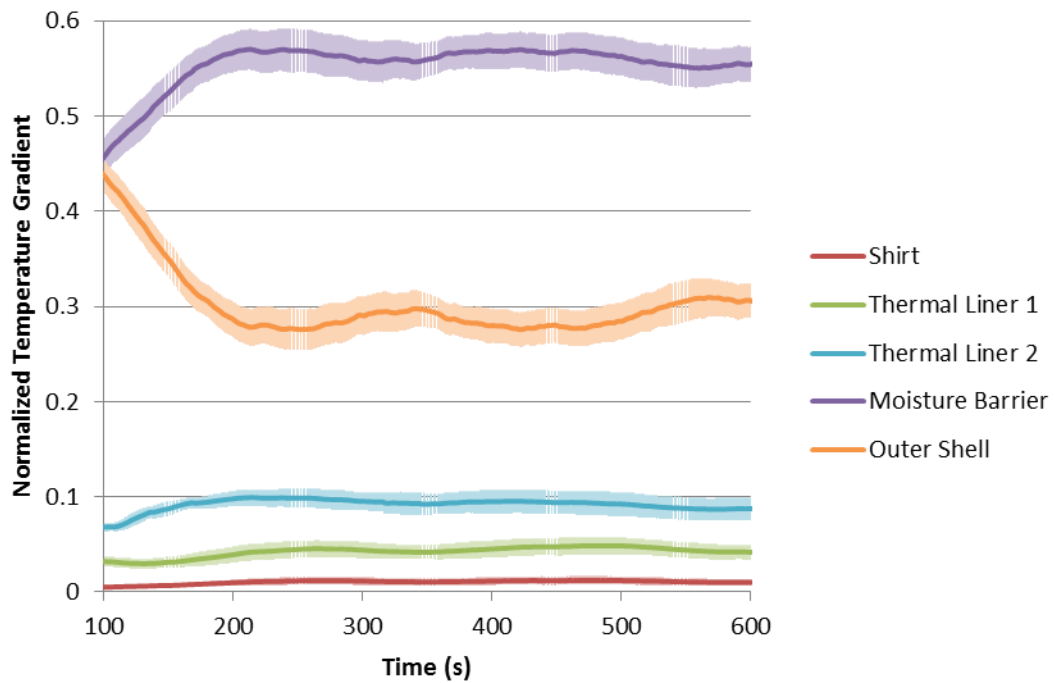
Space Intentionally Left Blank

Figure H.6: Time evolution of individual layer NTG parameters for assembly L-F

Figure H.7: Time evolution of individual layer NTG parameters for assembly L-P

Figure H.8: Time evolution of individual layer NTG parameters for assembly L-T

Figure H.9: Time evolution of individual layer NTG parameters for assembly L-R

Figure H.10: Time evolution of individual layer NTG parameters for assembly A-0

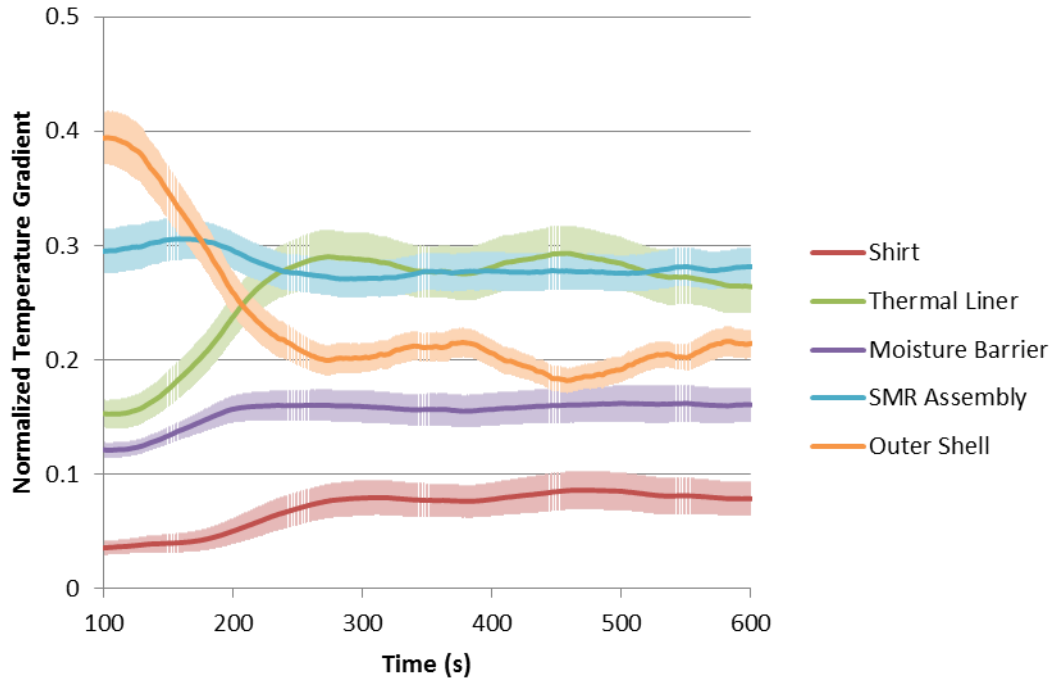**Figure H.11**: Time evolution of individual layer NTG parameters for assembly A-1

Figure H.12: Time evolution of individual layer NTG parameters for assembly A-2

Figure H.13: Time evolution of individual layer NTG parameters for assembly A-4

Figure H.14: Time evolution of individual layer NTG parameters for assembly M_s-D

Figure H.15: Time evolution of individual layer NTG parameters for assembly M_t-D
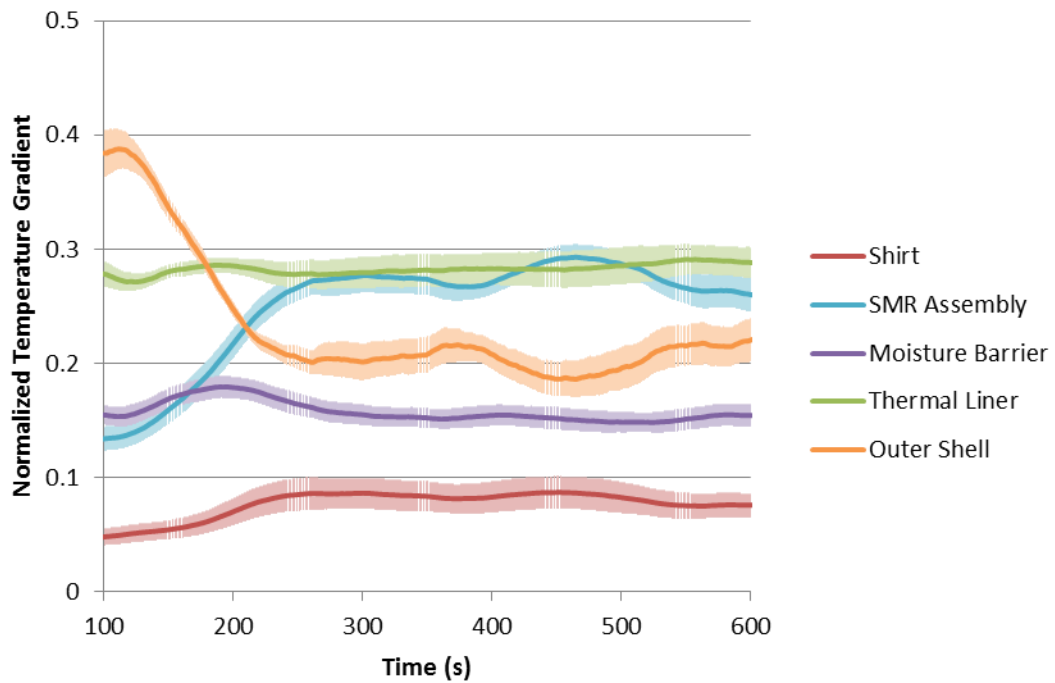
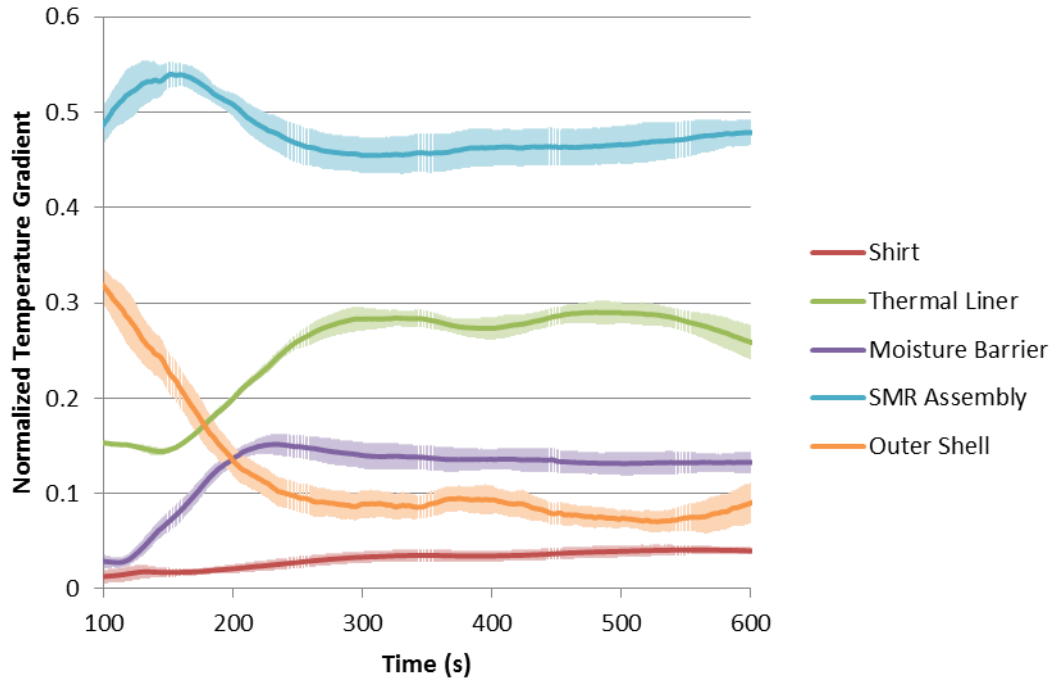**Figure H.16**: Time evolution of individual layer NTG parameters for assembly M_s-W

Figure H.17: Time evolution of individual layer NTG parameters for assembly M_t-W
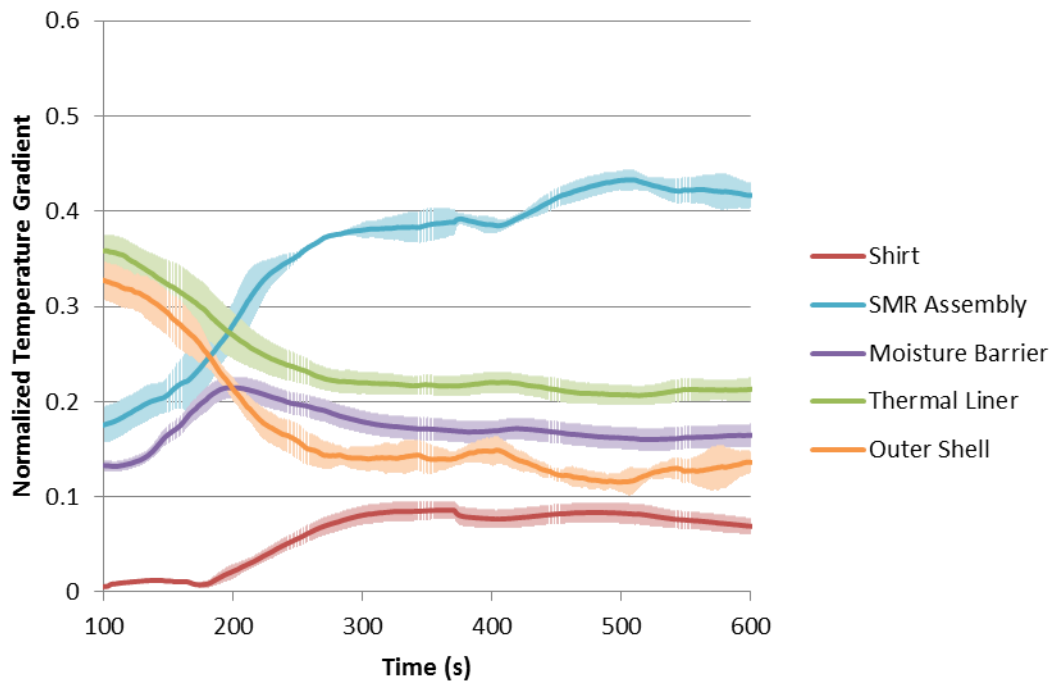
Figure H.18: Time evolution of individual layer NTG parameters for assembly $E_o\text{-}\emptyset$

Figure H.19: Time evolution of individual layer NTG parameters for assembly $E_i\text{-}\emptyset$
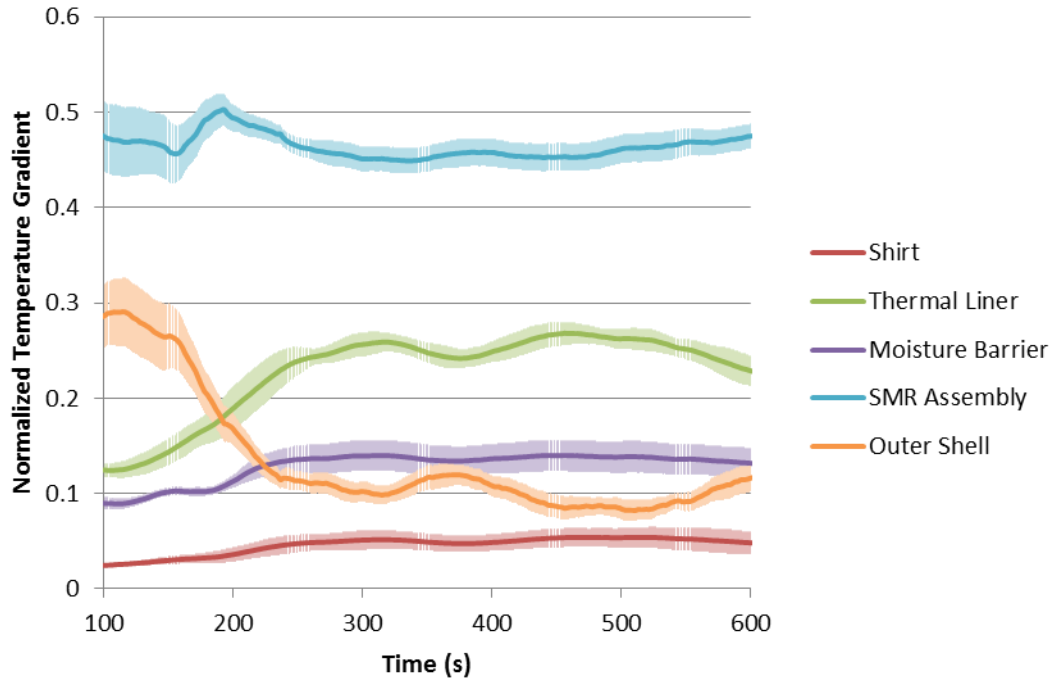
Figure H.20: Time evolution of individual layer NTG parameters for assembly E_o-50
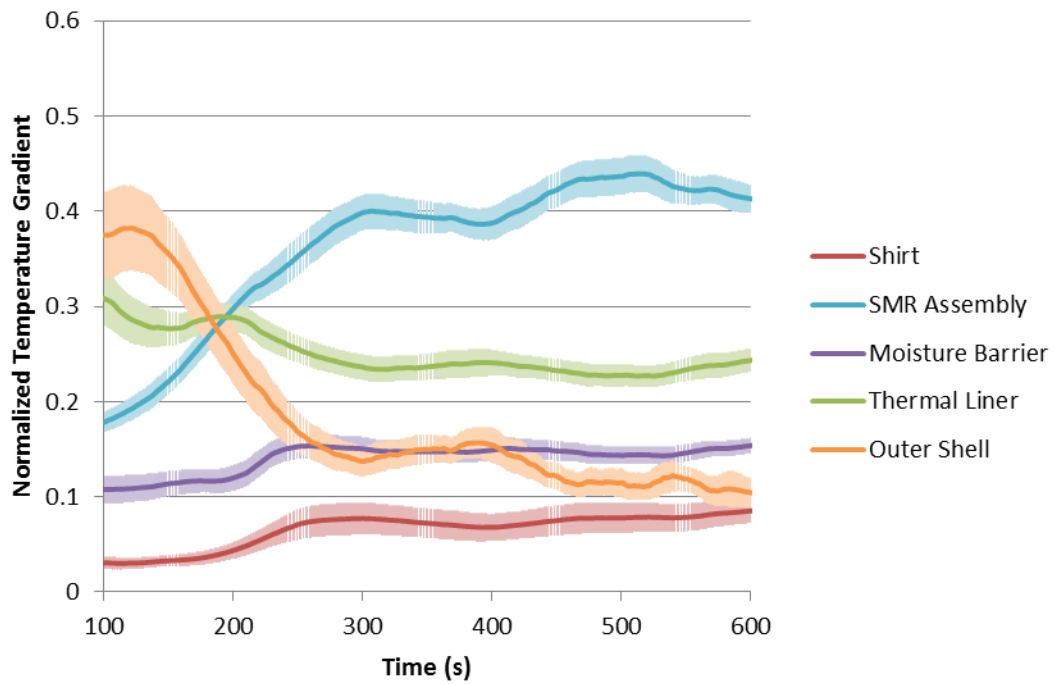

Figure H.21: Time evolution of individual layer NTG parameters for assembly E_i-50

Figure H.22: Time evolution of individual layer NTG parameters for assembly E_o-90

Figure H.23: Time evolution of individual layer NTG parameters for assembly E_i-90

References

[1]   Hasenmeier, Paul. "The History of Firefighter Personal Protective Equipment." *Fire Engineering* (2008): 1-4.

[2]   NFPA. *NFPA 1971: Standard on Protective Ensembles for Structural Fire Fighting and Proximity Fire Fighting, 2007 edition*. Quincy: National Fire Protection Association, 2006.

[3]   Lagoudas, Dimitris C. *Shape Memory Alloys: Modeling and Engineering Applications*. New York: Springer, 2008.

[4]   Brinson, L. C. "One-Dimensional Constitutive Behavior of Shape Memory Alloys." *Journal of Intelligent Material Systems and Structures* 4 (1993): 229-42.

[5]   Otsuka, K., and C. M. Wayman. *Shape Memory Materials*. Cambridge: Cambridge University Press, 1998.

[6]   Incropera, Frank, et al. *Fundamentals of Heat and Mass Transfer*. 6th ed. Hoboken: John Wiley & Sons, 2007.

[7]   Takahashi, Kaneko, et al. "Numerical Simulation of the Effective Thermal Conductivity of Wet Clothing Materials." *Heat Transfer – Japanese Research* 27.3 (1998): 243-54.

[8]   Dias, Tilak, and G. B. Delkumburewatte. "The Influence of Moisture Content on the Thermal Conductivity of a Knitted Structure." *Measurement Science and Technology* 18 (2007): 1304-14.

[9]   Chitrphiromsri, Patirop, and Andrey V. Kuznetsov. "Modeling Heat and Moisture Transport in Firefighter Protective Clothing during Flash Fire Exposure." *Heat Mass Transfer* 41 (2005): 206-15.

[10]   Chitrphiromsri, Patirop. "Modeling of Thermal Performance of Firefighter Protective Clothing during the Intense Heat Exposure." PhD thesis. North Carolina State University, 2004.

[11]   Pennes, H. H. "Analysis of Tissue and Arterial Blood Temperatures in Resting Human Forearm." *Journal of Applied Physiology* 1.2 (1948): 93-122.

[12]   Henriques, F. C., and A. R. Moritz. "Studies of Thermal Injury V: The Predictability and the Significance of Thermally Induced Rate Processes Leading to Irreversible Epidermal Injury." *Archives of Pathology* 43.5 (1947): 489-502.

[13]   Song, Guowen, et al. "Numerical Simulations of Heat and Moisture Transport in Thermal Protective Clothing Under Flash Fire Conditions." *International Journal of Occupational Safety and Ergonomics* 14.1 (2008): 89-106.

[14]   Torvi, David A., et al. "Influence of Air Gaps on Bench-Top Test Results of Flame Resistant Fabrics." *Journal of Fire Protection Engineering* 10 (1999): 1-12.

[15]   Torvi, David A. "Heat Transfer in Thin Fibrous Materials Under High Heat Flux Conditions." PhD thesis. University of Alberta, 1997.

[16]   Zhu, Fanglong, et al. "Study of Skin Model and Geometry Effects on Thermal Performance of Thermal Protective Fabrics." *Heat Mass Transfer* 45 (2008): 99-105.

[17]   Perry, Justin. "Thermal Degradation of Firefighter Turnout Gear due to the Effects of Moisture." MS thesis. University of Maryland, 2011.

[18]   Hendrickson, Bryant. "The Impact of a Variable Air Gap on the Thermal Performance of Firefighter Protective Clothing." MS thesis. University of Maryland, 2011.

[19]   Spangler, Kevin. "Energy Transport in Firefighter Protective Clothing." MS thesis. University of Maryland, 2008.

[20]   Schneider, Anna M. "Heat Transfer through Moist Fabrics." PhD thesis. University of New South Wales, 1987.

[21]   Yates, David. "Full-Scale Validation of a Numerical Heat Transfer Model for Thermally Responsive Firefighter Safety Gear." MS thesis. University of Maryland, 2012.

[22]   Devore, Jay. *Probability and Statistics for Engineering and the Sciences*. 8th ed. Boston: Cengage Learning, 2009

[23]   Ellis, Robert, and Denny Gulick. *Calculus*. 7th ed. Boston: Cengage Learning, 2011.

[24]   Carslaw, H. S., and J. C. Jaeger. *Conduction of Heat in Solids*. 2nd ed. Oxford: Oxford University Press, 1986.